Interplay between seismic and aseismic deformation on the Central Range fault during the 2013 Mw 6.3 Ruisui earthquake (Taiwan)

Hsiao-Fan Lin[1], Adriano Gualandi[2], Yu-Fang Hsu[1], Ya-Ju Hsu[1], Hsin-Hua Huang[3], Hsin-Ming Lee[3], and Alexandre Canitano[3]

[1]Institute of Earth Sciences, Academia Sinica
[2]Istituto Nazionale di Geofisica e Vulcanologia
[3]Academia Sinica

April 16, 2023

Abstract

The 2013 Ruisui earthquake represents the first unequivocal evidence of the activity of the Central Range fault in central Longitudinal Valley, Taiwan. Using a joint Bayesian finite-fault source inversion of Global Navigation Satellite System and strain time series, we infer that coseismic rupture occurred between 4 to 19 km depth with maximum slip of 0.5 m located near the hypocenter. We then apply a variational Bayesian Independent Component Analysis approach to displacement signals to infer a 3-month long afterslip located in the near-source region. This observation represents the first evidence of aseismic slip on the Central Range fault. Combining geodetic and seismological analysis with simulations based on rate-and-state friction mechanics, we analyze the interplay between seismic and aseismic deformation during the earthquake sequence. We observe that afterslip represents the dominant postseismic deformation mechanism, with $>95\%$ of the moment being released aseismically in the postseismic phase. Besides, afterslip likely represents the driving force controlling aftershock productivity and the spatiotemporal migration of seismicity. Finally, we infer the presence of a shallow velocity strengthening zone (0-4 km depth) associated with spatially heterogeneous slip during the postseismic phase with maximum slip of 0.15 m located above the zone of maximum coseismic deformation.

Interplay between seismic and aseismic deformation on the Central Range fault during the 2013 M_w 6.3 Ruisui earthquake (Taiwan)

Hsiao-Fan Lin[1], Adriano Gualandi[2], Yu-Fang Hsu[3], Ya-Ju Hsu[1], Hsin-Hua Huang[1], Hsin-Ming Lee[1] and Alexandre Canitano[1*]

Corresponding author: A. Canitano, Institute of Earth Sciences, Academia Sinica, Nankang, Taipei, Taiwan. (canitano@earth.sinica.edu.tw)

[1]Institute of Earth Sciences, Academia Sinica, Nankang, Taipei, Taiwan.

[2]Department of Earth Sciences, Bullard Laboratories, UK.

[3]Department of Earth Sciences, University of Southern California, Los Angeles, CA, USA.

Abstract.

The 2013 Ruisui earthquake represents the first unequivocal evidence of the activity of the Central Range fault in central Longitudinal Valley, Taiwan. Using a joint Bayesian finite-fault source inversion of Global Navigation Satellite System and strain time series, we infer that coseismic rupture occurred between 4 to 19 km depth with maximum slip of 0.5 m located near the hypocenter. We then apply a variational Bayesian Independent Component Analysis approach to displacement signals to infer a 3-month long afterslip located in the near-source region. This observation represents the first evidence of aseismic slip on the Central Range fault. Combining geodetic and seismological analysis with simulations based on rate-and-state friction mechanics, we analyze the interplay between seismic and aseismic deformation during the earthquake sequence. We observe that afterslip represents the dominant postseismic deformation mechanism, with $> 95\%$ of the moment being released aseismically in the postseismic phase. Besides, afterslip likely represents the driving force controlling aftershock productivity and the spatiotemporal migration of seismicity. Finally, we infer the presence of a shallow velocity strengthening zone ($\sim$ 0-4 km depth) associated with spatially heterogeneous slip during the postseismic phase with maximum slip of 0.15 m located above the zone of maximum coseismic deformation.

Plain Language Summary: Tectonic faults display a broad range of slip patterns, ranging from fast slip (earthquakes) to episodic or continuous aseismic slip. Aseismic transient slip events are now widely observed in active regions and play an important role in stress redistribution in the Earth's crust. The Central Range fault is the second most active fault in the Longitudinal Valley, in eastern Taiwan. During the past 15 years, the fault hosted large to destructive earthquakes, but little is known about the presence and the role of aseismic events on the fault deformation. The 2013 Ruisui earthquake reveals for the first time the presence of transient slip regions on the Central Range fault, capable of sustaining aseismic deformation over months. Besides, slow stress relaxation on the fault plane may have also influenced the behavior of seismicity following the mainshock. Monitoring and characterizing the sources of aseismic slip is fundamental to identify areas with high seismic hazard on the fault and to gain more knowledge about the interactions between seismic and aseismic processes.

1. Introduction

The Longitudinal Valley (LV), in eastern Taiwan, represents the collision boundary between the Philippine Sea plate (PSP) and the Eurasian plate (EP) [*Barrier and Angelier*, 1986], and accounts for about a third of plate convergence [*Yu and Kuo*, 2001]. The Central Range fault (CRF) is dipping westward underneath the western flank of the LV [*Biq*, 1965], and contributes to the rapid uplift (3-10 mm.yr^{-1}) of the Central Range (CR) [*Shyu et al.*, 2006] (Figure 1(a)). The CRF and the Longitudinal Valley fault (LVF), which bounds the eastern flank of the LV, represent the major active structures in eastern Taiwan. However, the role of the CRF in the regional geodynamics and even its existence have long been debated because of the absence of unambiguous geomorphic expression of the fault and its lack of recent seismic activity [*Shyu et al.*, 2006]. In the past 15 years, a succession of moderate to large ruptures (moment magnitude $M_w \geq 5.9$) has led to the activation of the CRF almost along its entire length [*Lee et al.*, 2023]. The M_w 6.1 Taitung earthquake that occurred in 2006 in southern LV represents the first large event ever recorded on the CRF [*Mozziconacci et al.*, 2013]. In May 2014, a M_w 5.9 earthquake ruptured the fault section located north of the Ruisui earthquake [*Wen*, 2018]. Then, the northernmost section of the fault ruptured during the 2019 M_w 6.1 [*Lee et al.*, 2020] and the 2021 M_w 6.2 [*Hwang et al.*, 2022] earthquake sequences. Recently, in September 2022, a M_w 6.6 earthquake struck the southern section of the CRF at the depth of 9 km, and was followed about 16 hours later by an M_w 7.1 event (8 km depth) [*Yagi et al.*, 2023]. The sequence shows a complex rupture pattern that possibly reflects the spatially heterogeneous stress and structure properties of the CRF [*Yagi et al.*, 2023]. Finally, the 18 September 2022 Chengkung earthquake also represents the largest event striking the island since the 1999 devastating Chi-Chi earthquake [*Rousset et al.*, 2012], and thus reveals that the CRF can also generate destructive earthquakes.

The 31 October 2013 Ruisui earthquake, which ruptured a shallow to intermediate section (4 to 20 km depth) of the CRF [*Lee et al.*, 2014], represents the first unequivocal evidence of the fault activity in central LV [*Chuang et al.*, 2014]. Based on dense seismological and geodetic (Global Navigation Satellite System (GNSS), strainmeters) networks, previous studies have inferred a complex rupture pattern distributed over a $\sim$ 30 km $\times$ 25 km fault plane [*Lee et al.*, 2014; *Canitano et al.*, 2017], striking 201°-209° NE, dipping 44°-59° westward with a dominant left-lateral thrust-faulting mechanism (47°-57°) [*Chuang et al.*, 2014; *Canitano et al.*, 2015; *Lin et al.*, 2019]. In this study, we invert GNSS and strain time series to infer a static finite-fault coseismic model of the earthquake. We also present the first evidence of postseismic deformation on the CRF. Indeed, a frictional afterslip is detected by near-source GNSS stations ($\leq$ 25 km from the epicenter) during about 3 months following the mainshock. We characterize the velocity strengthening region of the CRF and its implication during the Ruisui mainshock by combining geodetic and seismological analysis with numerical simulations based on rate-and-state friction mechanics [*Marone et al.*, 1991; *Dieterich*, 1994].

2. Instrumentation and data processing

2.1. Aftershock catalog

We apply the time and spatial double-link cluster-analysis approach [*Wu and Chiao*, 2006] to analyze the aftershock sequence during the first 3 months following the mainshock. We apply the method to the Central Weather Bureau (CWB) catalog after 3-D double-difference relocation [*Wu et al.*, 2008; *Huang et al.*, 2014]. The approach identifies aftershocks via a space-time distance linking and we select 3 days and 5 km as optimal parameters, as widely utilized in Taiwan region [*Hsu et al.*, 2021; *Huang and Wang*, 2022]. We then estimate the completeness magnitude M_c of the aftershock sequence using a magnitude correction factor of 0.1, which corresponds to the size of the event magnitude binning [*Schorlemmer et al.*, 2005]. Using the maximum curvature approach in *ZMAP* software [*Wiemer*, 2001], we infer $M_c = 1.6 \pm 0.1$, and we retain aftershocks with local magnitude $M_L \geq M_c$ (423 events) (Figure 1(b)). We estimate a and b parameters in the Gutenberg-Richter law [*Gutenberg and Richter*, 1944] using a maximum-likelihood approach ($a = 3.671$, $b = 0.653 \pm 0.032$) (Figure 2(a)). b-value is consistent with estimates inferred for thrust-faulting events ($b \sim 0.7$) [*Schorlemmer et al.*, 2005] and with values observed in the Ruisui region ($b \sim$ 0.7-0.8) [*Wu et al.*, 2018]. Finally, the evolution of aftershock activity is explained by the Omori-Utsu law [*Utsu et al.*, 1995] with parameters: $p = 0.99$, $k = 56.2$, and $c = 0.041$ day (Figure 2(b)). p-value estimate represents a typical value for aftershock decay rate (median value of 1.1) [*Utsu et al.*, 1995].

2.2. GNSS data

We process displacement time series for 82 GNSS stations in eastern Taiwan with the *GAMIT10.42/GLOBK5.16* software packages [*Herring et al.*, 2010]. We estimate daily solutions through double-differenced carrier phase measurements. We also utilize additional stations (362 from Taiwan, 8 from Ryukyu and 17 International GNSS Service sites in the Asia-Pacific region) to assess a more accurate pattern of regional deformation for Taiwan. Finally, we process *GAMIT* output with *GLOBK* to estimate daily positions in

ITRF2008 reference frame [*Altamini et al.*, 2012]. Then, we use a Principal component analysis (PCA) [*Dong et al.*, 2006; *Gualandi et al.*, 2014] to estimate horizontal and vertical coseismic offsets related to the Ruisui earthquake. We apply the PCA to 40 GNSS stations over a 2-month period (30 days prior and following the earthquake) (Figure S1 in the Supplementary Information) and permanent coseismic displacements are obtained by fitting the first principal component to a Heaviside function H (Figure 3(a) and Table S1).

To isolate postseismic deformation from signals of both non-tectonic (e.g., hydrological loading cycles [*Hsu et al.*, 2020]) and tectonic origin [*Gualandi et al.*, 2017], we process the displacement time series recorded by 28 near-source stations over a 1.5-year time period (from January 2013 to May 2014). First, we model displacement time series x with a trajectory equation described as follows:

$$x(t) = q + mt + \sum_{i=1}^{n_{eq}} H\left(t - t_{eq}^{(i)}\right) A_{eq}^{(i)} + \sum_{j=1}^{n_{off}} H\left(t - t_{off}^{(j)}\right) A_{off}^{(j)}$$
$$+ A_{yr}\sin\left(2\pi t + \phi_{yr}\right) + A_{hfyr}\sin\left(4\pi t + \phi_{hfyr}\right) + \sum_{i=1}^{n_{eq}} H\left(t - t_{eq}^{(i)}\right) A_{post}^{(i)} \times \left(1 - e^{-\frac{t - t_{eq}^{(i)}}{\tau_{post}^{(i)}}}\right) \tag{1}$$

where q is a constant, m is the secular velocity, t is time, $A_{eq}^{(i)}$ is the coseismic step starting at time $t_{eq}^{(i)}$, n_{eq} is the number of detected earthquakes, $A_{off}^{(j)}$ is instrumental offset at time $t_{off}^{(j)}$, n_{off} is the number of detected offsets, A_{yr} and A_{hfyr} are the amplitudes of the annual and semi-annual seasonal motions with phase shifts ϕ_{yr} and ϕ_{hfyr} respectively, $A_{post}^{(i)}$ is the maximum amplitude of the postseismic displacement with relaxation time $\tau_{post}^{(i)}$. Second, a linear trend and both instrumental and tectonic offsets are removed from position time series (first line in Equation (1)) and we keep all other signals (second line). Finally, we input the corrected time series into a variational Bayesian Independent Component Analysis (vbICA) algorithm [*Choudrey and Roberts*, 2003] adapted to study complex geodetic signals [*Gualandi et al.*, 2016].

The ICA method is an unsupervised learning technique commonly used to resolve blind source separation problems [*Gualandi et al.*, 2016], which allows us to model signals for which the actual temporal functional form is unknown [*Serpelloni et al.*, 2018]. Here we use the vbICA, which assumes that observations are generated by a linear mixture of a limited number of statistically independent sources, because it offers more flexibility in characterizing and extracting sources with multimodal probability density functions, as commonly observed in geophysical time series. We set the number of independent components (IC) using an Automatic Relevance Determination method (nIC = 5) [*Gualandi et al.*, 2016]. The postseismic displacement signal is mapped in the first independent component IC1 and represents the prominent signal in GNSS data for the selected epoch (Figure S2). We infer 11 stations with resolvable postseismic relaxation (cumulative horizontal displacements ≥ 3 mm) (Figure S3), mainly located in the earthquake near-source region (≤ 25 km from epicenter).

2.3. Strainmeter data

We estimate dilatation (ϵ_v) coseismic offsets for the 9 *Sacks-Evertson* borehole dilatometers [*Sacks et al.*, 1971] operating during the earthquake. We calibrate the dilatometers through waveform correlation between observed and synthetic tides following *Canitano et al.* [2018a]. We correct the 100-Hz sampling data for solid and ocean tidal strain, air pressure-induced strain and borehole relaxation [*Hsu et al.*, 2015; *Canitano et al.*, 2021] and estimate coseismic strain offsets following *Lin et al.* [2022]. Coseismic static contraction of -900 nϵ to -360 nϵ, well above the measurement noise of $\sim$ 1 nϵ, is recorded by near-field dilatometers (15-20 km SE of the rupture) (Figure 4). Far-field stations (40-60 km away from the rupture) show moderate to little expansion (about 15 nϵ to 35 nϵ), while no coseismic steps are recorded by DONB and FBRB stations.

3. Finite-fault coseismic model

We follow a two-step approach to estimate a finite-fault coseismic slip model. In a first step, we estimate a preliminary model inverting geodetic data for a uniform slip distribution on a single patch. In a second step, we refine the fault discretization. Both solutions are obtained by the joint inversion of horizontal and vertical coseismic displacements for 40 GNSS stations and dilatation for 9 strainmeters. We utilize the *Geodetic Bayesian Inversion Software* (*GBIS*, MATLAB-based software) [*Bagnardi and Hooper*, 2018], which performs a rapid and robust characterization of source fault parameters and associated uncertainties for multiple geodetic datasets using a Bayesian approach and assuming elastic homogeneous half-space Green's function for a rectangular source [*Okada*, 1992]. We assume a rigidity of 30 GPa, as commonly used to model the Earth crust in the region [*Canitano et al.*, 2015]. We modified the *GBIS* algorithm to integrate the calculation of internal deformations together with surface displacements [*Okada*, 1992].

To determine the preliminary source model, we invert for source dimensions and location (length, width, midpoint of the fault upper edge (X, Y, and depth)) and source parameters (strike, dip, uniform slip in the strike and in the dip direction) without imposing constraints onto fault strike (0°-360° clockwise from north), dip (0° to 90° from horizontal) angles and geologic slip direction to explore all possible fault kinematics and orientations. We searched for a fault plane within 15 km from the epicenter with a depth of the midpoint upper edge varying from 0 to 20 km and uniform slip ranging from -1.5 m to 2.0 m (10^6 iterations). We define the weighted misfit between the GNSS observations and the modeled coseismic displacements as follows:

$$misfit_G = \sqrt{\frac{r^T W r}{Tr(W)/3}} \tag{2}$$

where r is the vector of residual displacements between GNSS observations and models, W is the weight matrix, and $Tr(.)$ the matrix trace. The dilatation misfit is estimated as follows (all observations have identical weight):

$$misfit_\epsilon = \sqrt{\frac{\sum_{i=1}^{n}(\epsilon_v^{obs(i)} - \epsilon_v^{mod(i)})^2}{n}} \tag{3}$$

where $\epsilon_v^{obs(i)}$ and $\epsilon_v^{mod(i)}$ are the observed and modeled dilatation for the i^{th} strainmeter, respectively and n is the number of stations ($n = 9$). The source model reveals that surface displacements and dilatation are well explained ($misfit_G = 5$ mm and $misfit_\epsilon = 14$ nϵ) by a left-lateral thrust-fault (rake = 45°-47°) striking 203° and dipping 48° westward (Table S2). This source modeling agrees well with previous models [*Canitano et al.*, 2015; *Lin et al.*, 2019], and is consistent with a rupture on the CRF.

Then, we aim to obtain a more realistic rupture model by discretizing the extended previous fault plane (36 km × 30 km) into 270 subfaults (2 km × 2 km) and solve for slip on each patch. We fix strike and dip angles to values inferred from the uniform-slip model but we allow a variable rake on each subfault to account for the complex rupture pattern [*Lee et al.*, 2014; *Canitano et al.*, 2017]. To avoid unrealistic slip values because of the small amount of constraints west of the fault plane, we apply a zero slip boundary constraint B (unapplied to the plane top edge). A weighted least squares inversion with constraints on smoothness and boundary is performed by minimizing the cost function $\phi(s)$:

$$\phi(s) = \|\Sigma_d^{-1/2}\,(d - Gs)\,\|^2 + \beta\|Ls\|^2 + \alpha\|Bs\|^2 \qquad (4)$$

where Σ_d is the error covariance matrix, d is GNSS and strain observation matrix, G is the Green's function, s is the slip vector on each subfault and L is the 9-point stencil finite difference Laplacian. β and α are the weighting factors for smoothing and boundary constraints, respectively. We estimate the optimal smoothing factor ($\beta = 152$) by minimizing the leave-one-out cross-validation mean squared error [*Matthews and Segall*, 1993] (Figure S4).

Our preferred model ($misfit_G = 4$ mm and $misfit_\epsilon = 16$ nϵ) (Figure 3(b)) shows that the rupture occurs on a fault plane with dimensions of approximately 26 km $\times$ 22 km located between 3 and 19 km depth (Figure 5). The main asperity is concentrated in a region with dimensions of $\sim$ 16 km $\times$ 10 km located between 6 and 16 km depth, with a peak slip of about 0.5 m located near the hypocenter. The asperity exhibits a dominant left-lateral thrust-faulting mechanism and aftershocks fall both within and at the edge of coseismic slip distribution. The total seismic moment of the rupture is 3.12×10^{18} N.m, corresponding to $M_w = 6.3$, in agreement with other studies [*Chuang et al.*, 2014; *Canitano* *et al.*, 2015]. We estimate the earthquake stress drop $\Delta\tau$ assuming a rectangular rupture [*Kanamori and Anderson*, 1975] and found a value (2 MPa), about twice lower than what obtained with seismological data (3.9 MPa) [*Lee et al.*, 2014] under the assumption of circular fault rupture [*Eshelby*, 1957].

4. Forward model of stress-driven afterslip

Several mechanisms are commonly involved in postseismic transient deformation. Viscoelastic lower crust or upper mantle relaxation can follow moderate-magnitude events ($M_w \sim$ 6-6.5) [*Mandler et al.*, 2021] and is characterized by large-scale and long-lasting deformation (months to years) [*Tang et al.*, 2019]. Here, postseismic relaxation is of short-duration ($\sim$ 3 months) and is mainly recorded by near-source GNSS stations. Poroelastic rebound is generated by changes in pore pressure in the near-source region due to a dislocation [*Peltzer et al.*, 1996]. We calculate the poroelastic deformation following *Li et al.* [2021] protocol for an undrained Poisson's ratio of 0.3. Predicted surface displacements ($\leq$ 1 mm) are one order of magnitude smaller than near-field transient deformation, therefore poroelastic rebound shows no appreciable contribution to postseismic deformation. We thus consider frictional afterslip as the main contributor to the postseismic deformation of the Ruisui earthquake. Typically, afterslip takes place on fault portions surrounding the coseismic rupture. These regions exhibit velocity strengthening behavior and can resist the rupture propagation [*Marone et al.*, 1991]. Afterslip usually represents the predominant deformation mechanism in the postseismic phase during weeks to months after the mainshock [e.g., *Hu et al.*, 2016].

Here, because of the small amount of stations detecting postseismic slip (11 stations) (Figure 1(a)), we are not able to resolve afterslip distribution using the discretized fault plane. Therefore, we perform a forward modeling of stress-driven afterslip to approximate the equivalent effects on the horizontal surface displacements generated by the time dependent slip response v of a fault governed by nonlinear rate strengthening friction parameters [*Dieterich*, 1994] using *Relax* software [*Barbot and Fialko*, 2010a, b], in which afterslip is driven by coseismic shear stress change:

$$v = 2v_0 \exp \frac{-\mu_0}{(a-b)} \sinh \frac{\tau}{(a-b)\sigma} \tag{5}$$

where v_0 represents the reference long-term slip velocity, μ_0 is the static reference friction at depth, a and b are frictional parameters, and τ and σ denote the shear and normal stress changes on the fault, respectively (assumed constant in time). We use the finite-fault coseismic model (26 km $\times$ 22 km) as the stress-driven source and explore parameters v_0, $(a-b)\sigma$, and the dimensions and location of afterslip regions. Given the size of the mainshock and the limited extension of the postseismic deformation, we are seeking for afterslip located in the vicinity of the coseismic slip region. We thus limit our search to the 36 km $\times$ 30 km plane considered for finite-fault modeling (Figure 1(b)). Note that forward modeling simulates relaxation taking place outside of the coseismic source area, which does not preclude the possibility that afterslip and coseismic slip did overlap. We explore two rupture scenarios: afterslip occurs only on the CRF (strike = 203°, dip = 48°, rake = 47°) (Figure S5(a)), and afterslip occurs on the CRF and on the shallow, creeping section of the LVF [*Thomas et al.*, 2014] (about 0-4 km depth) beneath which the CRF may be buried [*Shyu et al.*, 2006]. We model the shallow LVF section with a 5 km-wide receiver striking 20°NE with variable length and location and with a dip of 60° [*Thomas et al.*, 2014] and a rake at the surface of 60° [*Peyret et al.*, 2011] (Figure S5(b)).

In the case of the CRF, we analyze several receiver configurations to seek the simplest model explaining near-source horizontal displacements (Figure S6). Observations are well explained by postseismic relaxation surrounding the coseismic slip region. In particular, we find that shallow relaxation is required to explain observations recorded in the eastern rupture region (e.g., FENP, FONB, HRGN) and NS displacements for near-source stations DNFU and DSIN (Figures 6 and S7). Lateral relaxation on the southwestern fault plane region allows to predict horizontal displacements recorded by KNKO and NHSI stations. Frictional parameters show $v_0 = 5$ mm.yr^{-1}, agreeing with the long-term slip rate of the CRF [*Shyu et al.*, 2020] and $(a-b)\sigma = 3$ MPa, which is about the earthquake stress drop, and is also consistent with estimates for afterslip on continental faults (typically ~ 1 MPa) [*Perfettini and Avouac*, 2004]. This simple, forward relaxation model also explains the absence of detection for remote stations (e.g., YUL1, NPRS, ZCRS or SHUL) but tends to overestimate displacements for stations located south of the rupture (JSUI and CMRS) and to underestimate EW displacements for stations located right above the hypocenter (GUFU and DSIN) (Figure 7). Finally, adding the shallow section of the LVF as a passive fault in the forward modeling does not improve displacement modeling (Figure S8), suggesting that the fault did not appreciably contribute to postseismic stress relaxation.

5. Aftershock activity possibly mediated by frictional afterslip

To explore a possible connection between aftershock activity and afterslip, we first compare the cumulative seismicity with the afterslip temporal function mapped in IC1 component (Figure 8(a)). We observe a good correlation between the signals, which suggests that afterslip may represent the driving force behind aftershock productivity during the Ruisui sequence [*Perfettini and Avouac*, 2004; *Hsu et al.*, 2006; *Gualandi et al.*, 2020]. Besides, seismicity rate and postseismic relaxation decays are well explained by the Omori-Utsu law with p-value $= 1$ (Figure 2(b)). This particular case also reflects a temporal seismicity decay compatible with resisting stress on the fault plane increasing as the logarithm of the sliding velocity, as typically observed during afterslip [*Dieterich*, 1994; *Perfettini et al.*, 2018].

To further investigate how seismic and aseismic transient slip interact during the postseismic period, we analyze the spatiotemporal evolution of aftershocks. In particular, we seek a possible expansion of the aftershock region reflecting aftershock migration driven by afterslip [*Frank et al.*, 2017; *Perfettini et al.*, 2018]. For a rate strengthening rheology, the aftershock region expansion with time $\Delta R_a(t)$, since the onset time t_i of the first aftershock, is expressed as [*Perfettini et al.*, 2018]:

$$\Delta R_a(t) = \zeta(a-b)\sigma\frac{c}{\Delta\tau}\log\left(\frac{t}{t_i}\right) \tag{6}$$

where ζ is a constant and c represents the source radius assuming a circular crack model following *Eshelby* [1957]:

$$c = \left(\frac{7}{16}\frac{M_0}{\Delta\tau}\right)^{1/3} \tag{7}$$

We model the aftershock zone expansion using parameters related to our coseismic model ($c = 8.80$ km, $\Delta\tau = 2$ MPa) and we also test *Lee et al.* [2014] model ($c = 7.05$ km, $\Delta\tau = 3.9$ MPa). We assume $M_0 = 3.12\times10^{18}$ N.m, $(a-b)\sigma = 3$ MPa, $\zeta = 1$ [*Frank et al.*, 2017] and $t_i = 194$ s.

We observe that apparent propagation velocity shows substantial differences for these coseismic models using $(a-b)\sigma$ constrained from rate-and-state simulations (Figure 8(b), purple and blue curves). Aftershock propagation velocity is well reproduced using *Lee et al.* [2014] coseismic parameters while our model tends to overestimate migration speed by a factor of about 3. However, since *Lee et al.* [2014] coseismic model shows greater resolution and related static stress drop was estimated under the assumption of circular fault rupture [*Eshelby*, 1957], we may expect a good estimate of aftershock spatiotemporal evolution. Conversely, our model is probably too complex to assume circular rupture (Figure 5), so that stress drop is estimated based on a rectangular rupture [*Kanamori and Anderson*, 1975]. We can note that $(a-b)\sigma$ parameter also strongly impacts migration pattern. For instance, a value of $(a-b)\sigma = 1$ MPa (which also yields a reasonable fit to postseismic signals) would allow to predict well expansion velocity using our coseismic model (Figure 8(b), green curve). Overall, the absence of resolution for characterizing afterslip that possibly occurs in the coseismic slip region (where most of aftershocks are located) limits our ability to investigate further the impact of afterslip on seismicity during the postseismic phase of the Ruisui earthquake.

6. Discussion

We analyze GNSS, strain, and seismological time series to investiage the spatiotemporal evolution of crustal deformation related to the 2013 Ruisui earthquake. We observe that the fault plane geometry and location inferred from the joint geodetic inversion agree well with previous models [e.g., *Chuang et al.*, 2014; *Lin et al.*, 2019]. Our finite-fault model shows that the rupture is distributed on a 26 km $\times$ 22 km fault plane located at a depth of about 3 to 19 km. The absence of surface ruptures directly above the mainshock was also reported previously [*Lee et al.*, 2014; *Chuang et al.*, 2014]. The dimension and location of the main asperity are consistent with *Lee et al.* [2014] model, but the coseismic slip is underestimated by approximately 30%. *Lee et al.* [2014] have also inferred a second, shallow asperity (with average slip of 0.3-0.4 m) in the SW section of the fault plane associated with a left-lateral slip component. Our model possibly shows shallow slip ($\sim$ 3 to 9 km depth) (Figure 5) in the SW termination of the rupture associated with a dominant left-lateral slip component and which concentrates a small cluster of aftershocks, albeit with limited resolution. Finally, we observe that near-source deformation (recorded by HGSB, SSNB, CHMB, and ZANB), previously used to infer the mainshock source parameters [*Canitano et al.*, 2015], is well explained ($misfit_{\epsilon} = 1.0$ nϵ) (Figure 4). Since joint geodetic inversion is dominated by GNSS and strain observations recorded in the near-source region, far-field deformation (e. g., SJNB and TRKB) is likely underestimated by our model.

While the existence of aseismic transient slip regions on the CRF was previously suggested based on geodetic [*Canitano et al.*, 2019] and seismological (seismic swarms, repeating earthquakes) [*Chen et al.*, 2020; *Peng et al.*, 2021] observations, the Ruisui earthquake reveals unambiguously the presence of velocity strengthening regions capable of sustaining transient deformation over months. Using frictional rate-and-state parameters from our optimal relaxation model, we simulate the spatial evolution of postseismic slip on the CRF plane as a function of time (Figure 9). We observe that during the early postseismic phase (first 2 weeks to 1 month), afterslip spreads around the coseismic slip region with relatively limited slip (< 0.1 m). Then, postseismic slip increases in the shallow fault section, reaching a maximum cumulative slip of approximately 0.15 m about 3 months following the mainshock. The velocity strengthening region extends toward the surface and mainly covers the fault region located right above the main asperity (Figure 5). We estimate the total moment released by the 3-month afterslip considering the slip associated with the $0.5° \times 0.5°$ cells distributed on the plane inferred from GNSS forward modeling (30 km $\times$ 30 km) (Figure 7). We infer a moment of about 6.73×10^{17} N.m ($M_w \sim 5.8$), that represents about 20% of the cumulative seismic moment. Typically, ratio estimates for thrust-faulting earthquakes with $M_w \sim 6$ to 6.5 range from about 10% to 30% [*Hawthorne et al.*, 2016]. However, since aftershocks appear to be primarily driven by afterslip, the fraction of postseismic slip that possibly occurs within the coseismic area remains unknown. Finally, the cumulative seismic moment released by aftershocks (423 events with $M_L \geq 1.6$) is $M_0 \sim 2.56\times10^{16}$ N.m ($M_w = 4.9$) which represents less than 4% of the minimum cumulative moment released by afterslip. Consequently, aseismic slip represents the dominant mechanism of postseismic deformation, a commonly observed pattern in active regions [e.g., *Gualandi et al.*, 2020].

The presence of the shallow afterslip-prone region, possibly highly fractured [*Lee et al.*, 2014], has contributed to relieve stress aseismically in the postseismic phase, but may have also arrested the rupture propagation, acting as a barrier that impeded locally seismic slip to reach the surface [*Rolandone et al.*, 2018]. Rupture propagation toward the surface arrested by shallow fault creep was observed during the 2003 Chengkung earthquake [*Hsu et al.*, 2009; *Thomas et al.*, 2014] or during the 2020 Elazig (Turkey) event [*Cakir et al.*, 2023], for instance. Indeed, a field survey conducted shortly after the Ruisui earthquake reported the absence of surface fractures in the region located right above the main coseismic zone while fractures were found further south, near the southwestern rupture termination [*Lee et al.*, 2014], suggesting that coseismic slip has possibly penetrated the surface. Seismic rupture propagation may have been impacted by the spatially heterogeneous properties of the velocity strengthening area that shows the largest postseismic slip level right above the main coseismic zone and a smaller amount above the SW rupture section (Figure 9). Seismic rupture can partially or completely penetrate a region of transient deformation provided effective stress difference between coseismic and aseismic regions is large enough to facilitate it [*Lin et al.*, 2020]. The presence of this shallow transient zone may also be compatible with the very low level of historical seismicity on the shallow section of the CRF in the Ruisui region (Figure 7(b)). Overall, further investigations are needed to constrain the rheological properties of the CRF and to understand the mechanisms that contribute to relieving the strain accumulated in the crust.

7. Conclusions

The 2013 Ruisui earthquake represents the first unequivocal evidence of the activity of the CRF in central LV. In this study, combining geodetic and seismological observations with numerical simulations based on rate and state-dependent friction, we present the first evidence of postseismic transient deformation on the CRF. We observe that afterslip represents the dominant mechanism during the postseismic period, releasing $> 95\%$ of the moment through aseismic slip on the CRF. Further, we demonstrate that afterslip also likely acts as the driving force controlling aftershock productivity and the spatiotemporal migration of seismicity during the first 3 months following the mainshock. Such a mechanism was previously observed on the LVF [*Canitano et al.*, 2018b] and we present the first evidence that the CRF can also experience complex interactions between aseismic and seismic slip in the postseismic phase. Finally, since the 2022 Chihshang earthquake revealed that the CRF can generate major earthquakes ($M_w > 7$) but also that both the CRF and LVF southern fault segments might be connected and might ruptured together during a seismic event [*Lee et al.*, 2023], enhancing detection and characterization of aseismic fault slip in the LV will be fundamental to reducing earthquake hazards in Taiwan in the future.

Acknowledgments

The authors thank the Carnegie Institution of Washington for helping with the strainmeter project. We are grateful to IES staff for helping with GNSS data. We thank Marco Bagnardi for valuable comments concerning GBIS software.

Data Availability Statement

All GNSS, strainmeter, and aftershock catalog data and slip inversion codes used in this study are available at https://doi.org/10.5281/zenodo.7803958 [*Lin*, 2023]. The open-source Geodetic Bayesian Inversion Software (GBIS) is available from *Bagnardi and Hooper* [2018] at https://comet.nerc.ac.uk/gbis/. The Relax v1.0.7 software is available via https://geodynamics.org. Some figures are plotted with the Generic Mapping Tools [*Wessel and Smith*, 1998].

References

Altamini, Z., L. Métivier and X. Collilieux (2012), ITRF2008 plate motion model, *J. Geophys. Res.*, *117*, doi:10.1029/2011JB008930.

Bagnardi, M. and A. Hooper (2018), Inversion of surface deformation data for rapid estimates of source parameters and uncertainties: A Bayesian approach, *Geochem. Geophys. Geosystems*, *19*, 2194–2211.

Barbot, S. and Y. Fialko (2010a), Fourier-domain Green's function for an elastic semi-infinite solid under gravity, with applications to earthquake and volcano deformation, *Geophys. J. Int.*, *182*(2), 568–582.

Barbot, S. and Y. Fialko (2010b), A unified continuum representation of postseismic relaxation mechanisms: Semi-analytic models of afterslip, poroelastic rebound and viscoelastic flow, *Geophys. J. Int.*, *182*(3), 1124–1140.

Barrier, E. and J. Angelier (1986), Active collision in eastern Taiwan: the Coastal Range, *Tectonophysics*, *125*, 39–72.

Biq, C. (1965), The East Taiwan Rift, *Pet. Geol. Taiwan*, *4*, 93–106.

Cakir, Z., U. Dogan, A. M. Akoglu, S. Ergintav, S. Ozarpaci, A. Ozdemir, T. Nazadkhalil, N. Cakir, C. Zabci, M. H. Erkoc, M. Basmenji, M. Kokum and R. Bilham, Arrest of the M_w 6.8 January 24, 2020 Elazig (Turkey) earthquake by shallow fault creep, *Earth Planet. Sci. Lett.*, *608*, doi:10.1016/j.epsl.2023.118085.

Canitano, A., Y. J. Hsu, H. M. Lee, A. T. Linde and S. Sacks (2015), Near-field strain observations of the October 2013 Ruisui, Taiwan, earthquake: source parameters and limits of very-short term strain detection, *Earth Planets Space*, *67*, 125, doi:10.1186/s40623-015-0284-1.

Canitano, A., Y. J. Hsu, H. M. Lee, A. T. Linde and S. Sacks (2017), A first modeling of dynamic and static crustal strain field from near-field dilatation measurements: example of the 2013 M_w 6.2 Ruisui earthquake, Taiwan, *J. Geodesy*, *91*(1), 1–8.

Canitano, A., Y. J. Hsu, H. M. Lee, A. T Linde and S. Sacks (2018a), Calibration for the shear strain of 3-component borehole strainmeters in eastern Taiwan through Earth and ocean tidal waveform modeling, *J. Geodesy*, *92*(3), 223–240.

Canitano, A., M. Godano, Y. J. Hsu, H. M. Lee, A. T. Linde and S. Sacks (2018b), Seismicity controlled by a frictional afterslip during a small magnitude seismic sequence ($M_L < 5$) on the Chihshang Fault, Taiwan, *J. Geophys. Res. Solid Earth*, *123*(2), 2003–2018, doi:10.1002/2017JB015128.

Canitano, A., H. Gonzalez-Huizar, Y. J. Hsu, H. M. Lee, A. T. Linde and S. Sacks (2019), Testing the influence of static and dynamic stress perturbations on the occurrence of a shallow, slow slip event in eastern Taiwan, *J. Geophys. Res. Solid Earth*, *124*(3), 3073–3087, doi:10.1029/2018JB016742.

Canitano, A., M. Godano and M. Y. Thomas (2021), Inherited state of stress as a key factor controlling slip and slip mode: inference from the study of a slow slip event in the Longitudinal Valley, Taiwan, *Geophys. Res. Lett.*, *48*, doi:10.1029/2020GL090278.

Chen, Y., K. H. Chen, J. C. Hu and J. C. Lee (2020), Probing the variation in aseismic slip behavior around an active suture zone: observations of repeating earthquakes in Eastern Taiwan, *J. Geophys. Res. Solid Earth*, *125*(5), doi:10.1029/2019JB018561.

Choudrey, R. A. and S. J. Roberts (2003), Variational mixture of Bayesian independent component analyzers, *Neural Comput.*, *15*(1), 213–252.

Chuang, R. Y., K. M. Johnson, Y. T. Kuo, Y. M. Wu, C. H. Chang and L. C. Kuo (2014), Active back thrust in the eastern Taiwan suture revealed by the 2013 Rueisuei earthquake: evidence for a doubly vergent orogenic wedge ?, *Geophys. Res. Lett.*, *41*, 3464–3470.

Dieterich, J. (1994), A constitutive law for rate of earthquake production and its application to earthquake clustering, *J. Geophys. Res.*, *99*(B2), 2601–2618.

Dong, D., P. Fang, Y. Bock, F. Webb, L. Prawirodirdjo, S. Kedar and P. Jamason (2006), Spatiotemporal filtering using principal component analysis and Karhunen-Loeve expansion approaches for regional GPS network analysis, *J. Geophys. Res.*, *111*, B03405, doi:10.1029/2005JB003806.

Eshelby, J. D. (1957), The determination of the elastic field of an ellipsoid inclusion and related problems, *Proc. R. Soc. London A*, *241*, 376–396.

Frank, W. B., P. Poli and H. Perfettini (2017), Mapping the rheology of the Central Chile subduction zone with aftershocks, *Geophys. Res. Lett.*, *44*, 5374–5382.

Gualandi, A., E. Serpelloni and M. E. Belardinelli (2014), Space-time evolution of crustal deformation related to the M_w 6.3, 2009 L'Aquila earthquake (central Italy) from principal component analysis inversion of GPS position time-series, *Geophys. J. Int.*, *197*, 174–191.

Gualandi, A., E. Serpelloni and M. E. Belardinelli (2016), Blind source separation problem in GPS time series, *J. Geodesy*, *90*, 323–341.

Gualandi, A., C. Nichele, E. Serpelloni, L. Chiaraluce, D. Latorre, M. E. Belardinelli and J. P. Avouac (2017), Aseismic deformation associated with an earthquake swarm in the northern Apennines (Italy), *Geophys. Res. Lett.*, *42*, doi:10.1002/2017GL073687.

Gualandi, A., Z. Liu and C. Rollins (2020), Post-large earthquake seismic activities mediated by aseismic deformation processes, *Earth Planet. Sci. Lett.*, *530*, doi: 10.1016/j.epsl.2019.115870.

Gutenberg, R. and C. F. Richter (1944), Frequency of earthquakes in California, *Bull. Seismol. Soc. Am.*, *34*, 185–188.

Hawthorne, J. C., M. Simons and J.-P. Ampuero (2016), Estimates of aseismic slip associated with small earthquakes near San Juan Bautista, CA, *J. Geophys. Res. Solid Earth*, *121*, 8254–8275.

Herring, T., W. King and S. M. McCluskey (2010), Introduction to GAMIT/GLOBK release 10.4., *Mass. Inst. of Technol., Cambridge.*

Hsu, Y. J., M. Simons, J. P. Avouac, J. Galetzka, K. Sieh, M. Chlieh, D. Natawidjaja, L. Prawirodirdjo and Y. Bock (2006), Frictional afterslip following the 2005 Nias-Simeulue earthquake, Sumatra, *Science*, *312*, 1921–1926.

Hsu, Y. J., S. B. Yu and H. Y. Chen (2009), Coseismic and postseismic deformation associated with the 2003 Chengkung, Taiwan, earthquake, *Geophys. J. Int.*, *176*, 420–430.

Hsu, Y. J., Y. S. Chang, C. C. Liu, H. M. Lee, A. T. Linde, S. Sacks, G. Kitagawa and Y. G. Chen (2015), Revisiting borehole strain, typhoons, and slow earthquakes using quantitative estimates of precipitation-induced strain changes, *J. Geophys. Res. Solid Earth*, *120*(6), 4556–4571.

Hsu, Y. J., Y. Fu, R. Bürgmann, S. Y. Hsu, C. C. Lin, C. H. Tang and Y. M. Wu (2020), Assessing seasonal and interannual water storage variations in Taiwan using geodetic and hydrological data, *Earth Planet. Sci. Lett.*, *550*, doi:10.1016/j.epsl.2020.116532.

Hsu, Y. J., H. Kao, R. Bürgmann, Y. T. Lee, H. H. Huang, H. F. Hsu, Y. M. Wu and J. Zhuang (2021), Synchronized and asynchronous modulation of seismicity by hydrological loading: A case study in Taiwan, *Sci. Adv.*, *7:eabf7282*.

Hu, Y., R. Bürgmann, N. Uchida, P. Banerjee and J. T. Freymueller (2016), Stress-driven relaxation of heterogeneous upper mantle and time-dependent afterslip following the 2011 Tohoku earthquake, *J. Geophys. Res. Solid Earth*, *121*, 385–411.

Huang, H. H., Y. M. Wu, X. Song, C. H. Chang, S. J. Lee, T. M. Chang and H. H. Hsieh (2014), Joint V_p and V_s tomography of Taiwan: implications for subduction-collision orogeny, *Earth Planet. Sci. Lett.*, *392*, 177–191.

Huang, H H. and Y. Wang (2022), Seismogenic structure beneath the northern Longitudinal Valley revealed by the 2018-2021 Hualien earthquake sequences and 3-D velocity model, *Terr. Atmos. Ocean. Sci.*, *33:17*, doi:10.1007/s44195-022-00017-z.

Hwang, R D., Y. L. Huang, W. Y. Chang, C. Y. Lin, C. Y. Lin, S. T. Wang, J. B. Chan, J. P. Chang and T. W. Lin (2022), Radiated seismic energy from the 2021 M_L 5.8 and M_L 6.2 Shoufeng (Hualien), Taiwan, earthquakes and their aftershocks, *Terr. Atmos. Ocean. Sci.*, *33:19*, doi:10.1007/s44195-022-00020-4.

Kanamori, H. and D. L. Anderson (1975), Theoretical basis of some empirical relation in seismology, *Bull. Seismol. Soc. Am.*, 65(5), 1073–1095.

Lee, S. J., H. H. Huang, J. B. H. Shyu, T. Y. Yeh and T. C. Lin (2014), Numerical earthquake model of the 31 October 2013 Ruisui, Taiwan, earthquake: source rupture process and seismic wave propagation, *J. Asian Earth Sci.*, *96*, 374–385.

Lee, S. J., T. P. Wong, T. Y. Liu, T. C. Lin and C. T. Chen (2020), Strong ground motion over a large area in northern Taiwan caused by the northward rupture directivity of the 2019 Hualien earthquake, *J. Asian Earth Sci.*, *192*, 104095, doi: 10.1016/j.jseaes.2019.104095.

Lee, S. J., T. Y. Liu and T. C. Lin (2023), The role of the westdipping collision boundary fault in the Taiwan 2022 Chihshang earthquake sequence, *Sci. Rep.*, *13:3552*, doi: 10.1038/s41598-023-30361-0.

Li, S., T. Tao, Y. Chen, P. He, F. Gao, X. Qu and Y. Zhou (2021), Geodetic observation and modeling of the coseismic and postseismic deformation associated with the 2020 M_w 6.5 Monte Cristo earthquake, *Earth and Space Science*, *8*, doi:10.1029/2021EA001696.

Lin, J. T., W. L. Chang, D. Melgar, A. M. Thomas and C. Y. Chiu (2019), Quick determination of earthquake source parameters from GPS measurements: a study of suitability for Taiwan, *Geophys. J. Int.*, *219*, 1148-1162.

Lin, J. T., K. S. Aslam, A. M. Thomas and D. Melgar (2020), Overlapping regions of coseismic and transient slow slip on the Hawaiian décollement, *Earth Planet. Sci. Lett.*, *544*, doi:10.1016/j.epsl.2020.116353.

Lin, H. F., Y. F. Hsu and A. Canitano (2022), Source modeling of the 2009 Fengpin-Hualien earthquake sequence, Taiwan, inferred from static strain measurements, *Pure Appl. Geophys.*, *179*, doi:10.1007/s00024-022-03068-y.

Lin, H. F. (2023), Interplay between seismic and aseismic deformation on the Central Range fault during the 2013 Mw 6.3 Ruisui earthquake (Taiwan) [Dataset]. Zenodo. https://doi.org/10.5281/zenodo.7803958.

Mandler, E., F. Pintori, A. Gualandi, L. Anderlini, E. Serpelloni and M. E. Belardinelli (2021), Post-seismic deformation related to the 2016 Central Italy seismic sequence from GPS displacement time-series, *J. Geophys. Res. Solid Earth*, *126*, doi:10.1029/2021JB022200.

Marone, C. J., C. H. Scholz and R. Bilham (1991), On the mechanics of earthquake afterslip, *J. Geophys. Res.*, *96*, 8441–8452.

Matthews, M. V. and P. Segall (1993), Estimation of depth-dependent fault slip from measured surface deformation with application to the 1906 San Francisco earthquake, *J. Geophys. Res.*, *98*, 12,153–12,163.

Mozziconacci, L., B. Delouis, B. S. Huang, J. C. Lee and N. Béthoux (2013), Determining fault geometry from the distribution of coseismic fault slip related to the 2006 Taitung earthquake, eastern Taiwan, *Bull. Seismol. Soc. Am.*, *103*, 394–411.

Okada, Y. (1992), Internal deformation due to shear and tensile faults in a half-space, *Bull. Seism. Soc. Am.*, *82*(2), 1018–1040.

Peltzer, G., P. Rosen, F. Rogez and K. Hudnut (1996), Postseismic rebound in fault step-overs caused by pore fluid flow, *Science*, *273*(5279), 1202–1204.

Peng, W., D. Marsan, K. H. Chen and E. Pathier (2021), Earthquake swarms in Taiwan: a composite declustering method for detection and their spatial characteristics, *Earth Planet. Sci. Lett.*, *574*, doi:10.1016/j.epsl.2021.117160.

Perfettini, H. and J. P. Avouac (2004), Postseismic relaxation driven by brittle creep: A possible mechanism to reconcile geodetic measurements and the decay rate of aftershocks, application to the Chi-Chi earthquake, Taiwan, *J. Geophys. Res.*, *109*, B02304, doi:10.1029/2003JB002488.

Perfettini, H., W. B. Frank, D. Marsan and M. Bouchon (2018), A model of aftershock migration driven by afterslip, *Geophys. Res. Lett.*, *45*, 2283–2293.

Peyret, M., S. Dominguez, R. Cattin, J. Champenois, M. Leroy and A. Zajac (2011), Present-day interseismic surface deformation along the Longitudinal Valley, eastern Taiwan, from a PS-InSAR analysis of the ERS satellite archives, *J. Geophys. Res.*, *116*, B03402, doi:10.1029/2010JB007898.

Rolandone, F., J. M. Nocquet, P. A. Mothes, P. Jarrin, M. Vallée, N. Cubas, S. Hernandez, M. Plain, S. Vaca and Y. Font (2018), Areas prone to slow slip events impede earthquake rupture propagation and promote afterslip, *Sci. Adv.*, *4*, eaao6596.

Rousset, B., S. Barbot, J. P. Avouac and Y. J. Hsu (2012), Postseismic deformation following the 1999 Chi-Chi earthquake, Taiwan: implication for lower-crust rheology, *J. Geophys. Res.*, *117*, B12405, doi:10.1029/2012JB009571.

Sacks, S., S. Suyehiro, D. W. Evertson and Y. Yamagishi (1971), Sacks-Evertson strainmeter, its installation in Japan and some preliminary results concerning strain steps, *Pap. Meteorol. Geophys.*, *22*, 195–208.

Schorlemmer, D., S. Wiemer and M. Wyss (2005), Variations in earthquake-size distribution across different stress regimes, *Nature*, *437*, 539–542.

Serpelloni, E., F. Pintori, A. Gualandi, E. Scoccimarro, A. Cavaliere, L. Anderlini, M. E. Belardinelli and M. Todesco (2018), Hydrologically induced karst deformation: Insights from GPS measurements in the Adria-Eurasia plate boundary zone, *J. Geophys. Res. Solid Earth*, *123*, 4413–4430.

Shyu, J. B. H., K. Sieh, Y. G. Chen and L. H. Chung (2006), Geomorphic analysis of the Central Range fault, the second major active structure of the Longitudinal Valley suture, eastern Taiwan, *Geol. Soc. Am. Bull.*, *118*, 1447–1462.

Shyu, J. B. H., Y. H. Yin, C. H. Chen, Y. R. Chuang and S. C Liu (2020), Updates to the on-land seismogenic structure source database by the Taiwan Earthquake Model (TEM) project for seismic hazard analysis of Taiwan, *Terr. Atmos. Ocean. Sci.*, *31*(4), 469–478.

Tang, C. H., Y. J. Hsu, S. Barbot, J. D. P. Moore and W. L Chang (2019), Lower-crustal rheology and thermal gradient in the Taiwan orogenic belt illuminated by the 1999 Chi-Chi earthquake, *Sci. Adv.*, *5*(2), doi:10.1126/sciadv.aav3287.

Thomas, M. Y., J. P. Avouac, J. Champenois, J. C. Lee and L. C. Kuo (2014), Spatiotemporal evolution of seismic and aseismic slip on the Longitudinal Valley Fault, Taiwan, *J. Geophys. Res.*, *119*(6), 5114–5139.

Utsu, T., Y. Ogata and R. S. Matsu'ura (1995), The centenary of the Omori formula for a decay law of aftershock activity, *J. Phys. Earth*, *43*, 1–33.

Wen, Y. Y. (2018), Source characteristics of the northern Longitudinal Valley, Taiwan derived from broadband strong-motion simulation, *Pure Appl. Geophys.*, *175*, 587–596.

Wessel, P. and W. H. F. Smith (1998), New, improved version of the Generic Mapping Tools released, *Eos Trans. AGU*, *79*, 579, doi:10.1029/98EO00426.

Wiemer, S. (2001), A software package to analyze seismicity: ZMAP, *Seismol. Res. Lett.*, *72*(3), 373–382.

Wu, Y. M. and L. Y. Chiao (2006), Seismic quiescence before the 1999 Chi-Chi, Taiwan, M_w 7.6 earthquake, *Bull. Seismol. Soc. Am.*, *96*(1), 321–327.

Wu, Y. M., C. H. Chang, L. Zhao, T. L. Teng and M. Nakamura (2008), A comprehensive relocation of earthquakes in Taiwan from 1991 to 2005, *Bull. Seismol. Soc. Am.*, *98*, 1471–1481.

Wu, Y. M., S. K. Chen, T. C. Huang, H. H. Huang, W. A. Chao and I. Koulakov (2018), Relationship between earthquake b-values and crustal stresses in a young orogenic belt, *Geophys. Res. Lett.*, *45*, 1832–1837.

Yagi, Y., R. Okuwaki, B. Enescu and J. Lu (2023), Irregular rupture process of the 2022 Taitung, Taiwan, earthquake sequence, *Sci. Rep.*, *13:1107*, doi:10.1038/s41598-023-27384-y.

Yu, S. B. and L. C. Kuo (2001), Present-day crustal motion along the Longitudinal Valley Fault, eastern Taiwan, *Tectonophysics*, *333*, 199–217.

Figure 1: (a) Map of eastern Taiwan. The red and black triangles denote the strainmeters and GNSS stations, respectively. GNSS stations used for constraining postseismic relaxation are outlined (green box: stations recording surface displacements, and red box: stations with no displacements). The red star depicts the epicenter of the Ruisui earthquake (CGMT). The blue stars denote the epicenters of moderate to large earthquakes ($M_w \geq 5.9$) that struck the CRF from 2006 to 2022. The black dot shows Ruisui town. The black box shows the region in (b). (Inset) Geodynamic framework of Taiwan. The black arrow indicates the relative motion between the Philippine Sea plate (PSP) and Eurasian plate (EP); (RT): Ryukyu Trench. LVF: Longitudinal Valley fault; CRF: Central Range fault; LV: Longitudinal Valley. (b) Surface projection of the spatiotemporal evolution of the relocated aftershocks (with $M_L \geq 1.6$) during the first 3 months following the mainshock. Surface projection of the relocated plane used for finite-fault geodetic inversion (36 km $\times$ 30 km) (black rectangle) and of the main region of coseismic slip (26 km $\times$ 22 km) (red rectangle). The thick line depicts the top edge of each plane.

Figure 2: (a) Cumulative frequency-magnitude distribution of aftershocks during about 3 months following the mainshock. The dashed line represents the Gutenberg-Richter law ($log_{10}(N) = a - bM$, where N is the cumulative number of earthquakes having magnitudes larger than M) with $a = 3.671$ and $b = 0.653 \pm 0.032$ obtained via a maximum-likelihood approach. The magnitude of completeness ($M_c = 1.6 \pm 0.1$) for the sequence is estimated using a maximum curvature approach. (b) Cumulative number of aftershocks (N) over a $\sim$ 3-month period following the mainshock (after removing events with $M_L < M_c$) approximated with the cumulative Omori-Utsu law

($N(t) = K(c^{1-p} - (t+c)^{1-p})/(p-1)$, where K, c and p are constants).

Figure 3: Comparison of observed and modeled 3-D coseismic displacements associated with the 2013 Ruisui earthquake. (a) GNSS coseismic displacements obtained through a PCA approach (see Figure 1(a) for station details). Black vectors show horizontal displacements with a 95% confidence ellipse and circles show vertical displacements with uplift and subsidence indicated by warm and cold colors, respectively. The black star denotes the mainshock epicenter. (b) Modeled horizontal displacements (red arrows) and residual of vertical displacements (circles) inferred from the nonlinear joint inversion of GNSS and strain time series for a finite-fault model (Figure 5). The black thick line depicts the top edge of the fault plane and the dashed lines outline its surface projection.

Figure 4: Coseismic static dilatation offsets recorded by *Sacks-Evertson* borehole dilatometers over a 30-min period centered on the Ruisui earthquake onset timing. Expansion is positive.

Figure 5: Coseismic slip distribution resolved on 2 km $\times$ 2 km subfaults ($\beta = 152$). The dashed black rectangle denotes the ~ 26 km $\times$ 22 km fault plane hosting the rupture. The projection onto the fault plane of the mainshock epicenter is depicted by a black star and black dots show the projection of relocated aftershocks (with $M_L \geq 1.6$) occurring during the first 3 months following the mainshock.

Figure 6: Temporal evolution of stress-driven afterslip induced on the CRF over a 3-month period inferred from our best source combination (Figure 7(a)) (see Figure S7 for additional examples).

Figure 7: (a) Horizontal postseismic displacements detected by near-source GNSS stations estimated using a vbICA approach (black arrows) and predictions resulting from a forward nonlinear rate strengthening friction model (purple arrows). Near-source stations with insignificant detections are shown by red triangles. The purple rectangle outlines the receiver located on the CRF considered in the simulation. The thick line depicts the top edge of each plane. The plain red rectangle outlines the main coseismic slip region (stress-driven source) and the black star is the mainshock epicenter. (b) Relocated seismicity ($M_L \geq 1.5$) in central LV from 1990 to 2020 from the CWB. Relocated aftershocks of the Ruisui earthquake are shown by black dots. The shallow section of the CRF in the Ruisui region is associated with a very low level of historical seismicity.

Figure 8: (a) Comparison between the cumulative number of aftershocks (with $M_L \geq 1.6$) and the temporal evolution of afterslip (IC1 component). (b) Along-strike expansion of the aftershock zone of the Ruisui earthquake predicted using Equation (6).

Figure 9: Spatiotemporal evolution of postseismic slip along the CRF (Equation (5)) inferred from our optimal parameters ($v_0 = 5$ mm.yr^{-1}, $(a-b)\sigma = 3$ MPa). Postseismic relaxation surrounds the coseismic slip region (dark blue region) with average slip of $\sim$ 0.05-0.1 m and shows a spatially heterogeneous distribution in the shallow fault sec-

tion, with maximum cumulative slip of approximately 0.15 m about 3 months following the mainshock.

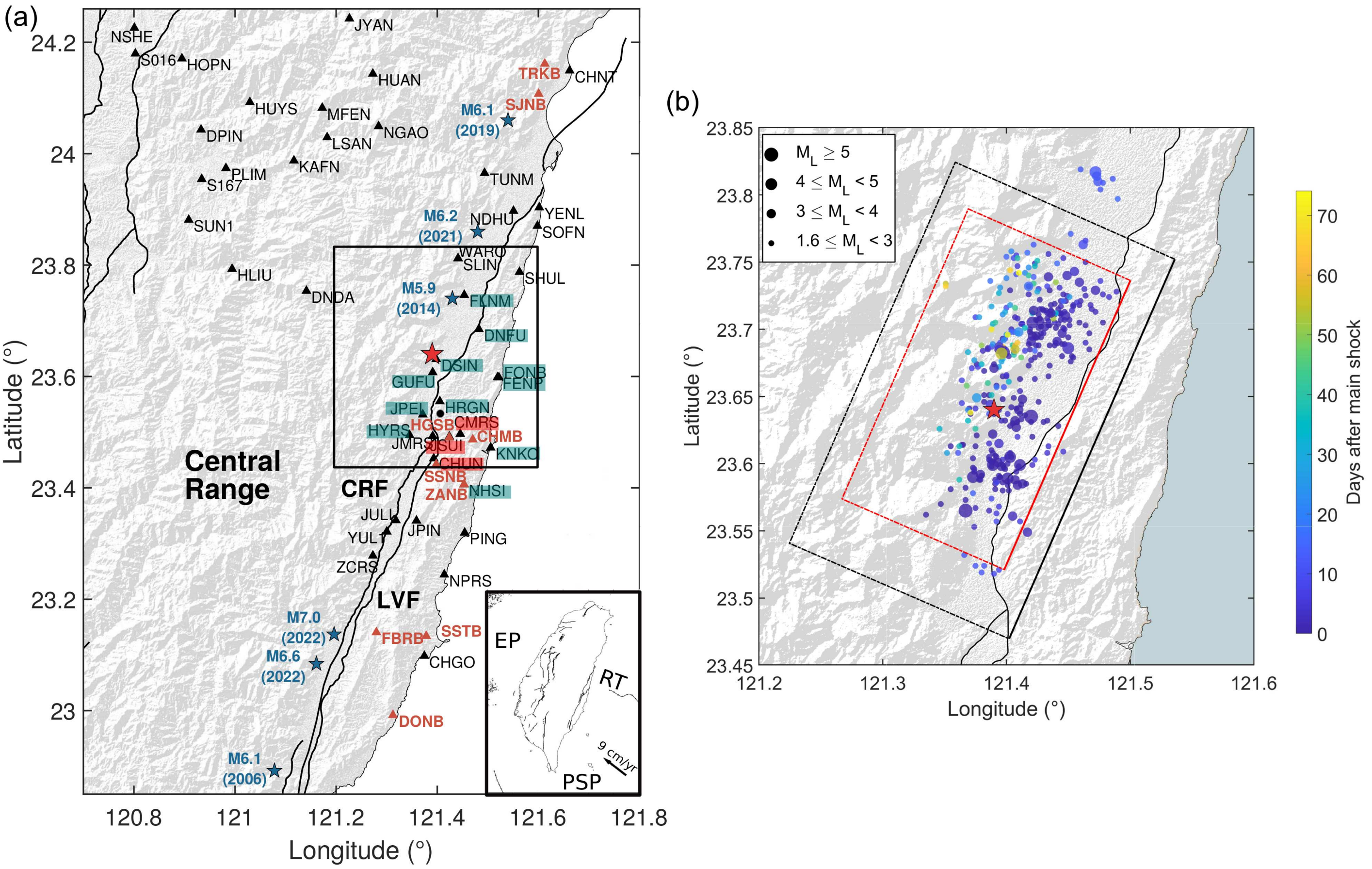
(a)
Central Range
CRF
LVF
EP
RT
PSP
9 cm/yr
M6.1 (2019)
M6.2 (2021)
M5.9 (2014)
M7.0 (2022)
M6.6 (2022)
M6.1 (2006)
Latitude (°)
Longitude (°)
(b)
Days after main shock
Latitude (°)
Longitude (°)

Figure 1.

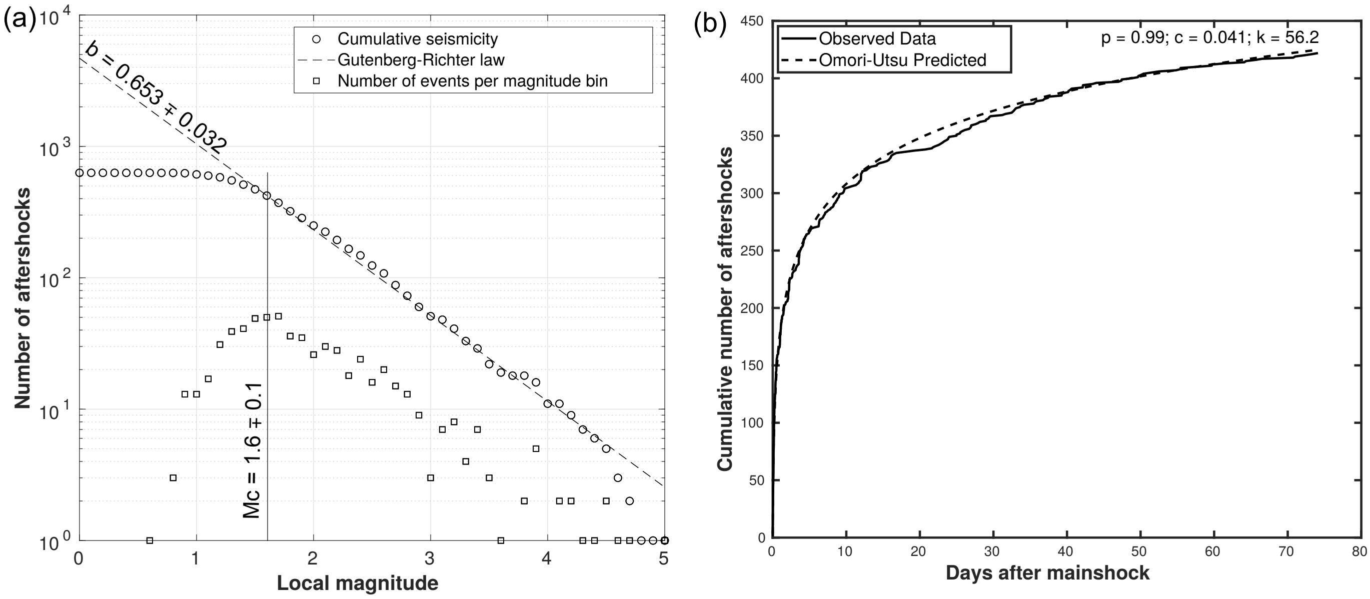

(a)
Cumulative seismicity
Gutenberg-Richter law
Number of events per magnitude bin
b = 0.653 ∓ 0.032
Mc = 1.6 ∓ 0.1
Number of aftershocks
Local magnitude
(b)
Observed Data
Omori-Utsu Predicted
p = 0.99; c = 0.041; k = 56.2
Cumulative number of aftershocks
Days after mainshock

Figure 2.

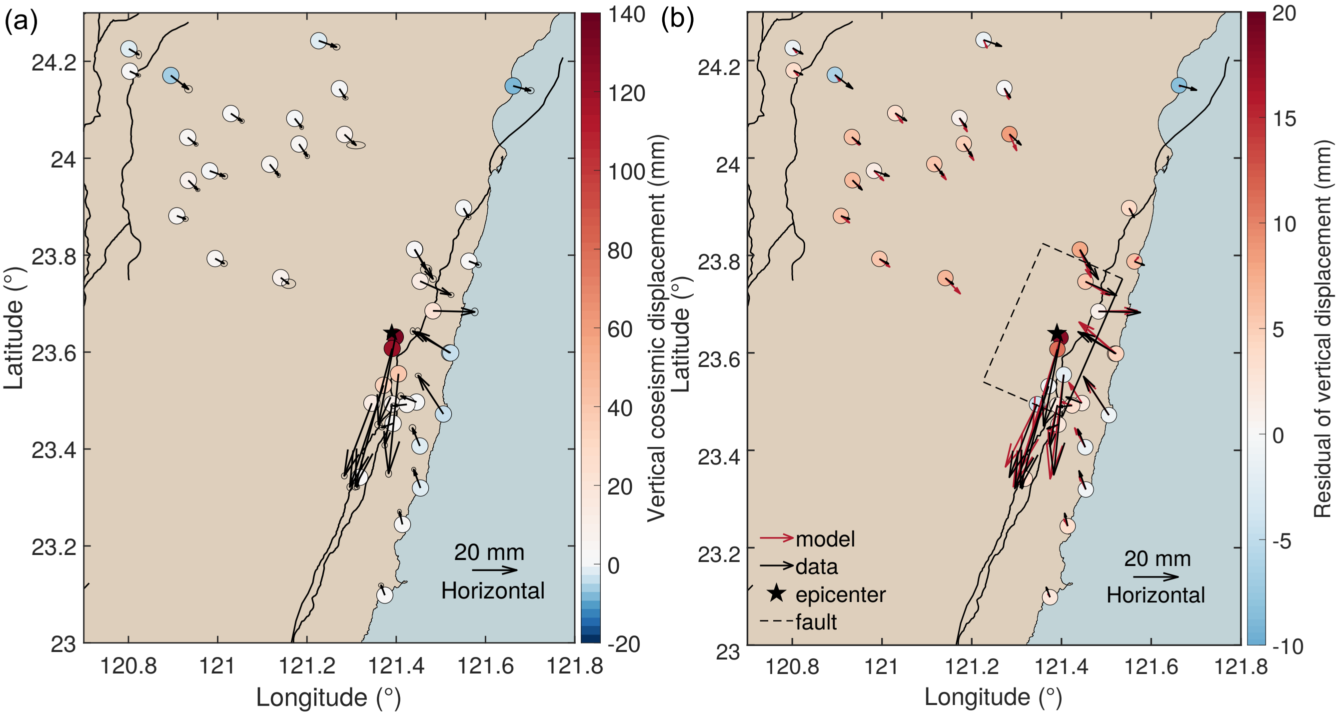
(a)
Latitude (°)
Longitude (°)
Vertical coseismic displacement (mm)
20 mm
Horizontal
(b)
Residual of vertical displacement (mm)
model
data
epicenter
fault

Figure 3.

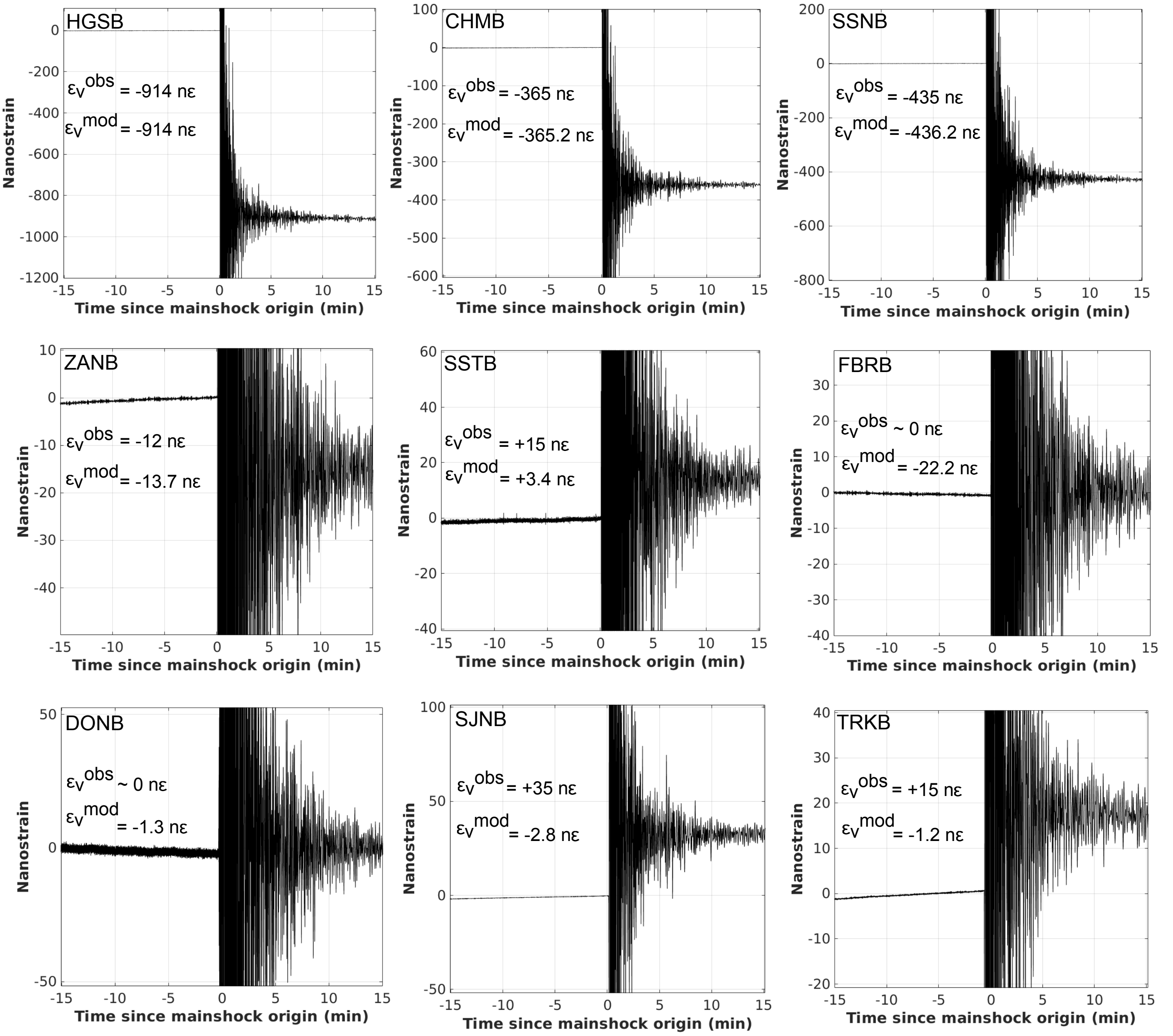
HGSB
ε_V^{obs} = -914 nε
ε_V^{mod} = -914 nε
CHMB
ε_V^{obs} = -365 nε
ε_V^{mod} = -365.2 nε
SSNB
ε_V^{obs} = -435 nε
ε_V^{mod} = -436.2 nε
ZANB
ε_V^{obs} = -12 nε
ε_V^{mod} = -13.7 nε
SSTB
ε_V^{obs} = +15 nε
ε_V^{mod} = +3.4 nε
FBRB
ε_V^{obs} ~ 0 nε
ε_V^{mod} = -22.2 nε
DONB
ε_V^{obs} ~ 0 nε
ε_V^{mod} = -1.3 nε
SJNB
ε_V^{obs} = +35 nε
ε_V^{mod} = -2.8 nε
TRKB
ε_V^{obs} = +15 nε
ε_V^{mod} = -1.2 nε
Nanostrain
Time since mainshock origin (min)

Figure 4.

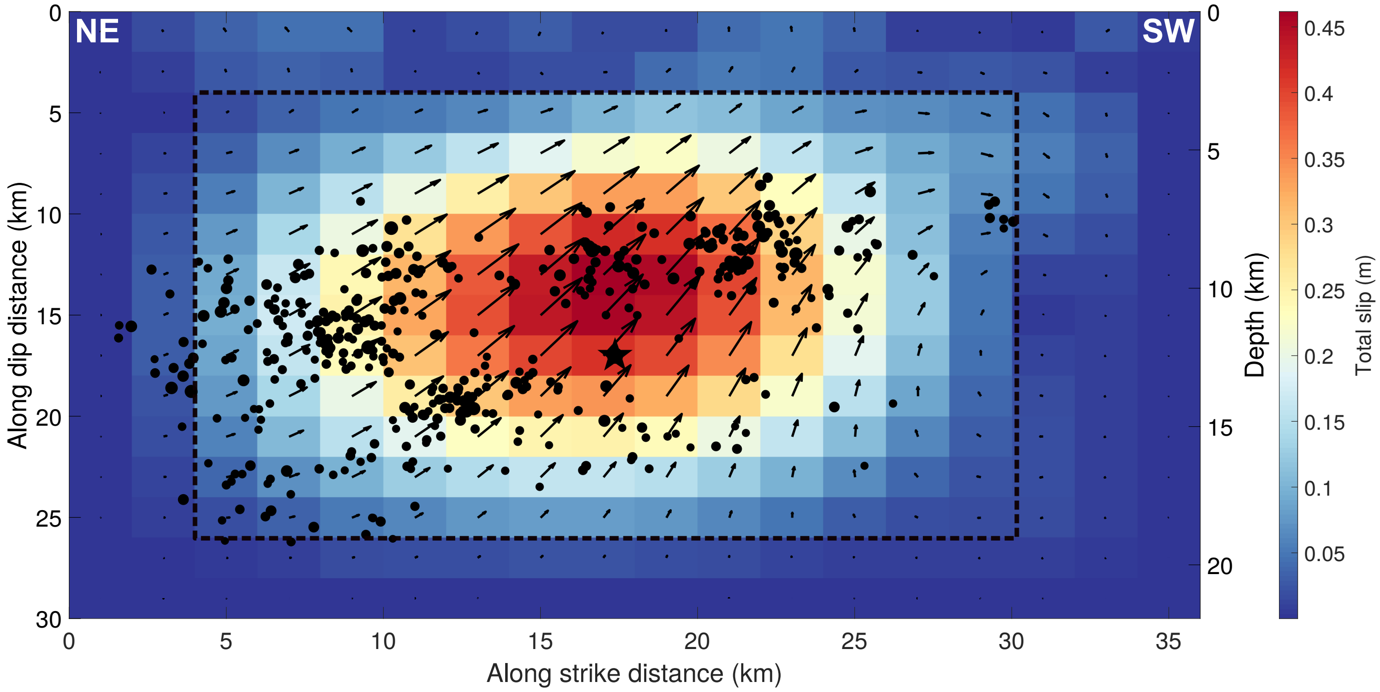
NE
SW
Along dip distance (km)
Along strike distance (km)
Depth (km)
Total slip (m)
0
5
10
15
20
25
30
35
0.45
0.4
0.35
0.3
0.25
0.2
0.15
0.1
0.05

Figure 5.

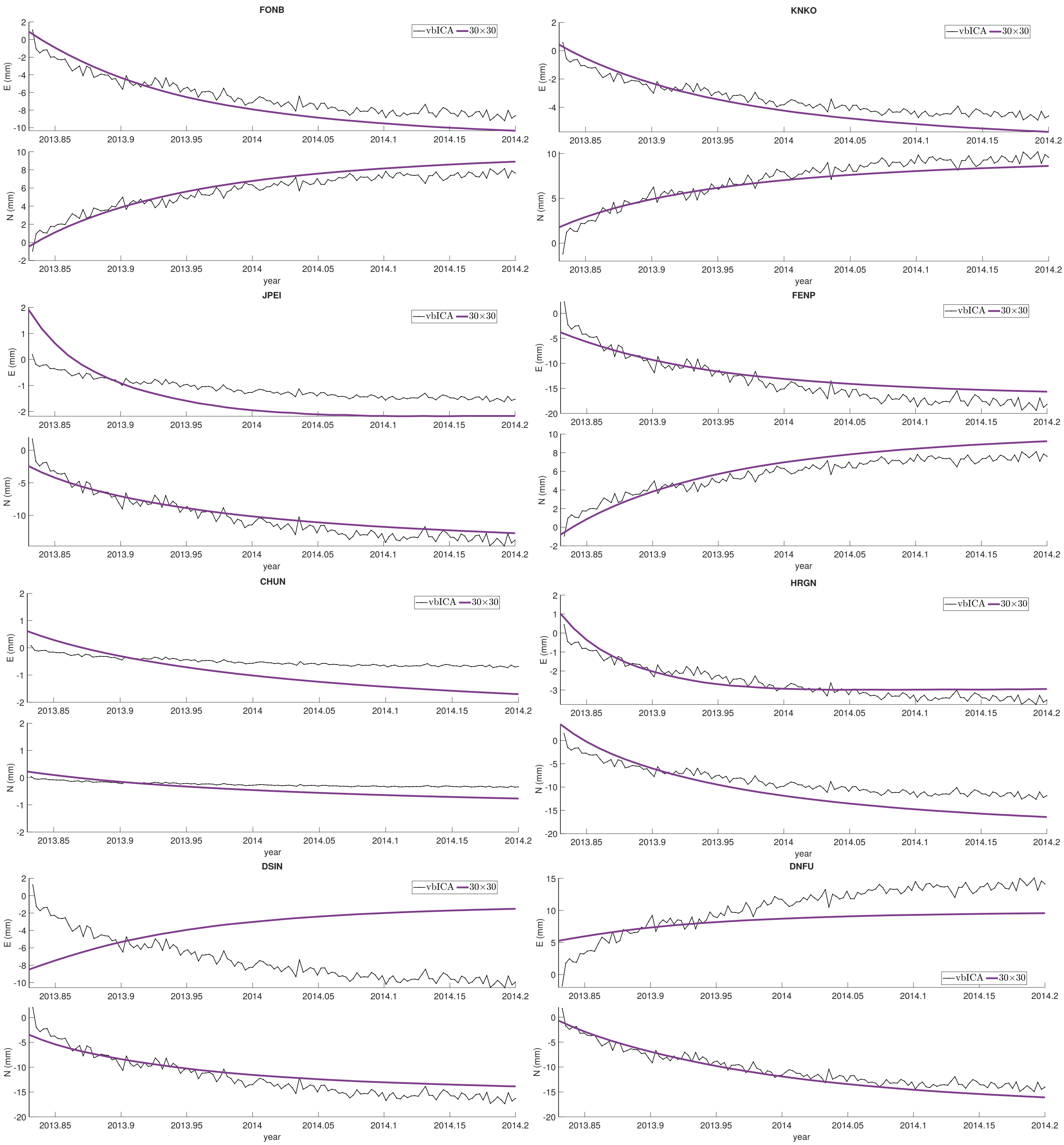
FONB
KNKO
JPEI
FENP
CHUN
HRGN
DSIN
DNFU
vbICA
30×30
E (mm)
N (mm)
year
2013.85
2013.9
2013.95
2014
2014.05
2014.1
2014.15
2014.2

Figure 6.

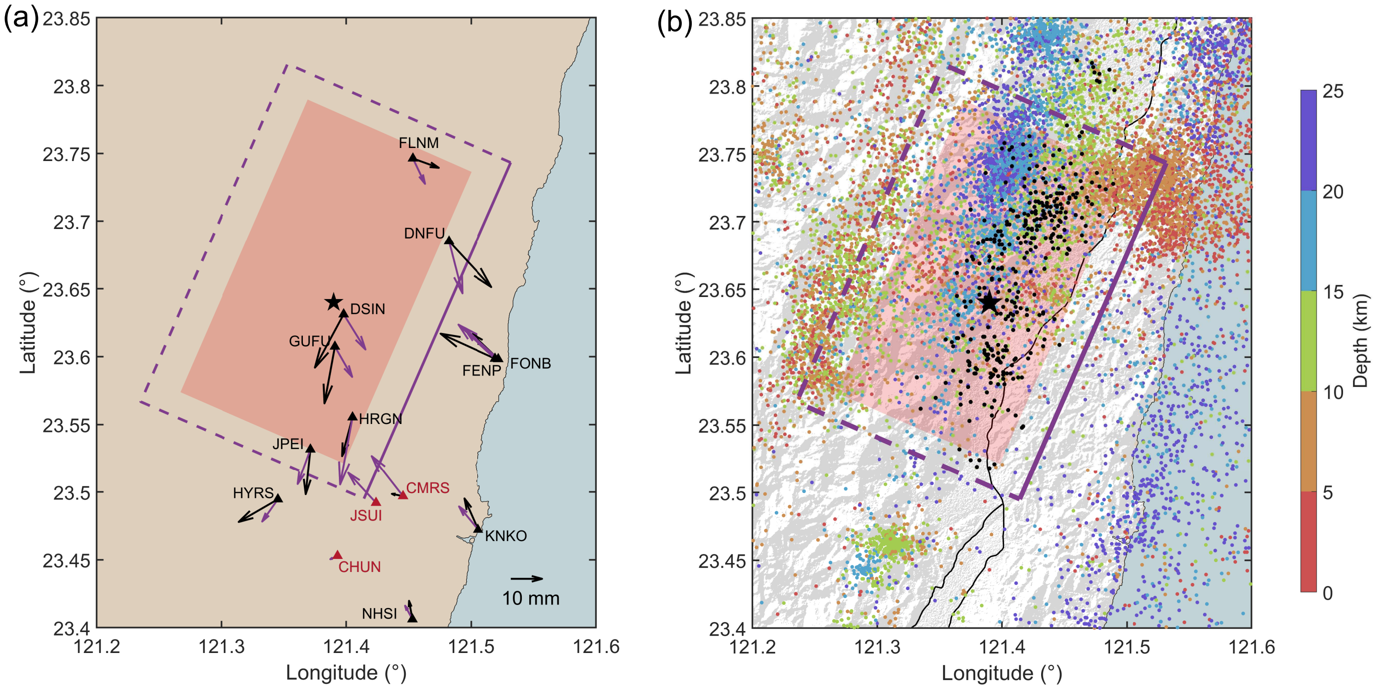
(a)
(b)
Latitude (°)
Longitude (°)
FLNM
DNFU
DSIN
GUFU
FENP
FONB
HRGN
JPEI
HYRS
CMRS
JSUI
KNKO
CHUN
NHSI
10 mm
Depth (km)

Figure 7.

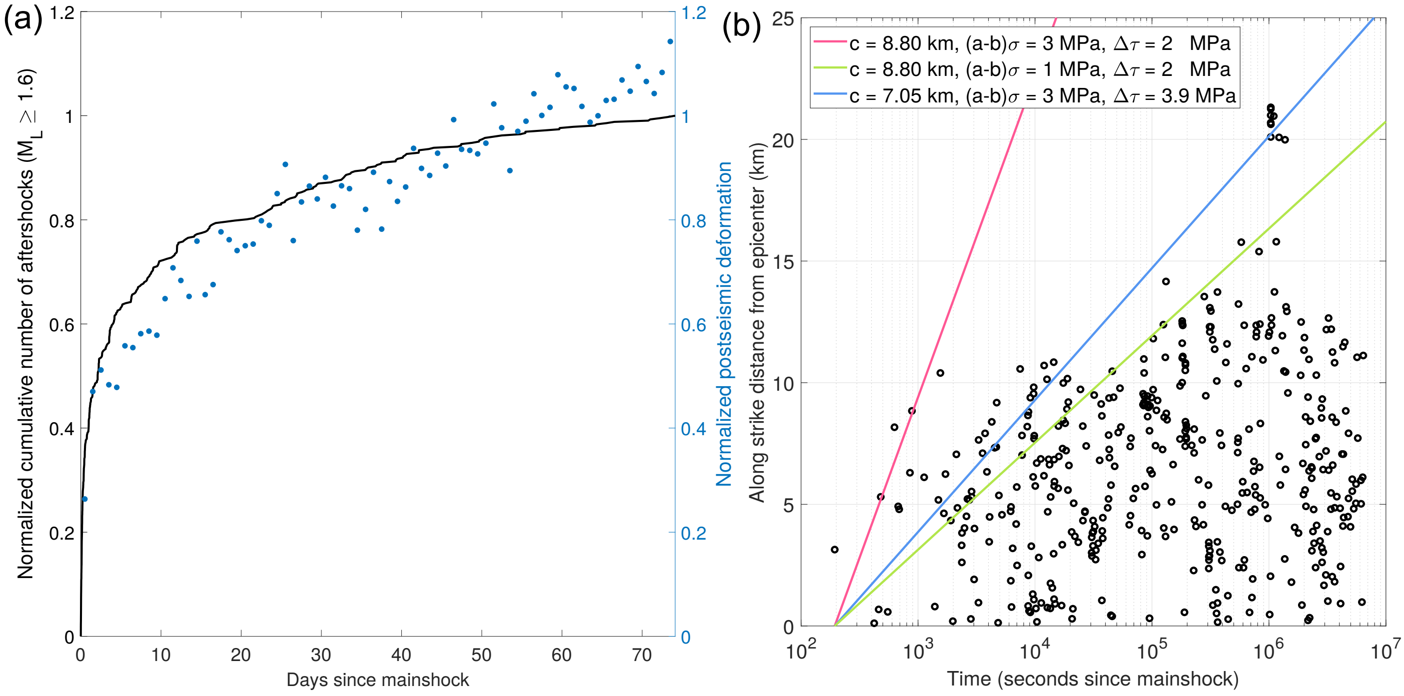

(a)
Normalized cumulative number of aftershocks ($M_L \geq 1.6$)
Normalized postseismic deformation
Days since mainshock
(b)
c = 8.80 km, (a-b)σ = 3 MPa, $\Delta\tau$ = 2 MPa
c = 8.80 km, (a-b)σ = 1 MPa, $\Delta\tau$ = 2 MPa
c = 7.05 km, (a-b)σ = 3 MPa, $\Delta\tau$ = 3.9 MPa
Along strike distance from epicenter (km)
Time (seconds since mainshock)

Figure 8.

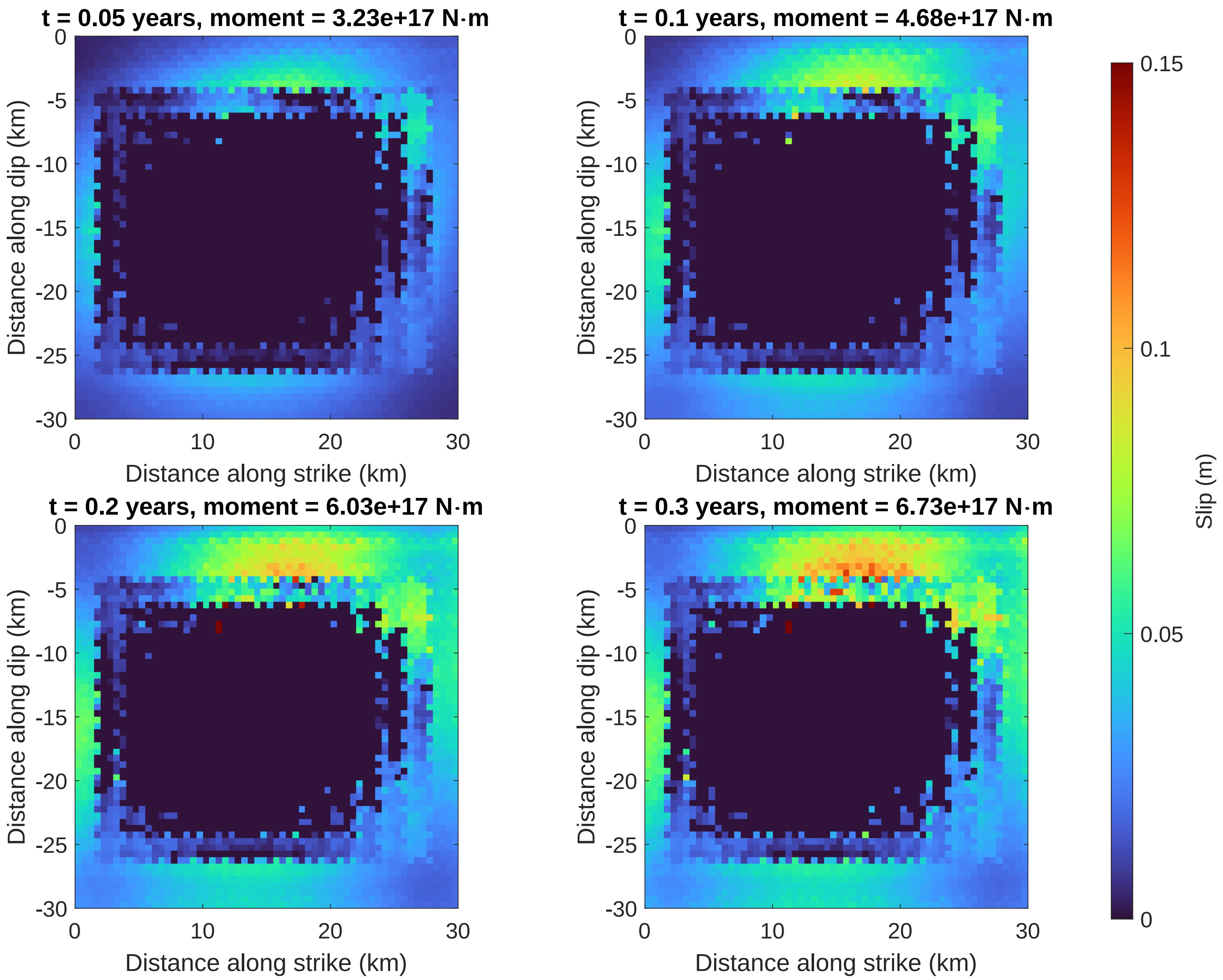
t = 0.05 years, moment = 3.23e+17 N·m
t = 0.1 years, moment = 4.68e+17 N·m
t = 0.2 years, moment = 6.03e+17 N·m
t = 0.3 years, moment = 6.73e+17 N·m
Distance along dip (km)
Distance along strike (km)
0
-5
-10
-15
-20
-25
-30
0
10
20
30
Slip (m)
0.15
0.1
0.05
0

Figure 9.

Interplay between seismic and aseismic deformation on the Central Range fault during the 2013 M_w 6.3 Ruisui earthquake (Taiwan)

Hsiao-Fan Lin[1], Adriano Gualandi[2], Yu-Fang Hsu[3], Ya-Ju Hsu[1], Hsin-Hua Huang[1], Hsin-Ming Lee[1] and Alexandre Canitano[1*]

Corresponding author: A. Canitano, Institute of Earth Sciences, Academia Sinica, Nankang, Taipei, Taiwan. (canitano@earth.sinica.edu.tw)

[1]Institute of Earth Sciences, Academia Sinica, Nankang, Taipei, Taiwan.

[2]Department of Earth Sciences, Bullard Laboratories, UK.

[3]Department of Earth Sciences, University of Southern California, Los Angeles, CA, USA.

Abstract.

The 2013 Ruisui earthquake represents the first unequivocal evidence of the activity of the Central Range fault in central Longitudinal Valley, Taiwan. Using a joint Bayesian finite-fault source inversion of Global Navigation Satellite System and strain time series, we infer that coseismic rupture occurred between 4 to 19 km depth with maximum slip of 0.5 m located near the hypocenter. We then apply a variational Bayesian Independent Component Analysis approach to displacement signals to infer a 3-month long afterslip located in the near-source region. This observation represents the first evidence of aseismic slip on the Central Range fault. Combining geodetic and seismological analysis with simulations based on rate-and-state friction mechanics, we analyze the interplay between seismic and aseismic deformation during the earthquake sequence. We observe that afterslip represents the dominant postseismic deformation mechanism, with $> 95\%$ of the moment being released aseismically in the postseismic phase. Besides, afterslip likely represents the driving force controlling aftershock productivity and the spatiotemporal migration of seismicity. Finally, we infer the presence of a shallow velocity strengthening zone ($\sim$ 0-4 km depth) associated with spatially heterogeneous slip during the postseismic phase with maximum slip of 0.15 m located above the zone of maximum coseismic deformation.

Plain Language Summary: Tectonic faults display a broad range of slip patterns, ranging from fast slip (earthquakes) to episodic or continuous aseismic slip. Aseismic transient slip events are now widely observed in active regions and play an important role in stress redistribution in the Earth's crust. The Central Range fault is the second most active fault in the Longitudinal Valley, in eastern Taiwan. During the past 15 years, the fault hosted large to destructive earthquakes, but little is known about the presence and the role of aseismic events on the fault deformation. The 2013 Ruisui earthquake reveals for the first time the presence of transient slip regions on the Central Range fault, capable of sustaining aseismic deformation over months. Besides, slow stress relaxation on the fault plane may have also influenced the behavior of seismicity following the mainshock. Monitoring and characterizing the sources of aseismic slip is fundamental to identify areas with high seismic hazard on the fault and to gain more knowledge about the interactions between seismic and aseismic processes.

1. Introduction

The Longitudinal Valley (LV), in eastern Taiwan, represents the collision boundary between the Philippine Sea plate (PSP) and the Eurasian plate (EP) [*Barrier and Angelier*, 1986], and accounts for about a third of plate convergence [*Yu and Kuo*, 2001]. The Central Range fault (CRF) is dipping westward underneath the western flank of the LV [*Biq*, 1965], and contributes to the rapid uplift (3-10 mm.yr^{-1}) of the Central Range (CR) [*Shyu et al.*, 2006] (Figure 1(a)). The CRF and the Longitudinal Valley fault (LVF), which bounds the eastern flank of the LV, represent the major active structures in eastern Taiwan. However, the role of the CRF in the regional geodynamics and even its existence have long been debated because of the absence of unambiguous geomorphic expression of the fault and its lack of recent seismic activity [*Shyu et al.*, 2006]. In the past 15 years, a succession of moderate to large ruptures (moment magnitude $M_w \geq 5.9$) has led to the activation of the CRF almost along its entire length [*Lee et al.*, 2023]. The M_w 6.1 Taitung earthquake that occurred in 2006 in southern LV represents the first large event ever recorded on the CRF [*Mozziconacci et al.*, 2013]. In May 2014, a M_w 5.9 earthquake ruptured the fault section located north of the Ruisui earthquake [*Wen*, 2018]. Then, the northernmost section of the fault ruptured during the 2019 M_w 6.1 [*Lee et al.*, 2020] and the 2021 M_w 6.2 [*Hwang et al.*, 2022] earthquake sequences. Recently, in September 2022, a M_w 6.6 earthquake struck the southern section of the CRF at the depth of 9 km, and was followed about 16 hours later by an M_w 7.1 event (8 km depth) [*Yagi et al.*, 2023]. The sequence shows a complex rupture pattern that possibly reflects the spatially heterogeneous stress and structure properties of the CRF [*Yagi et al.*, 2023]. Finally, the 18 September 2022 Chengkung earthquake also represents the largest event striking the island since the 1999 devastating Chi-Chi earthquake [*Rousset et al.*, 2012], and thus reveals that the CRF can also generate destructive earthquakes.

The 31 October 2013 Ruisui earthquake, which ruptured a shallow to intermediate section (4 to 20 km depth) of the CRF [*Lee et al.*, 2014], represents the first unequivocal evidence of the fault activity in central LV [*Chuang et al.*, 2014]. Based on dense seismological and geodetic (Global Navigation Satellite System (GNSS), strainmeters) networks, previous studies have inferred a complex rupture pattern distributed over a $\sim$ 30 km $\times$ 25 km fault plane [*Lee et al.*, 2014; *Canitano et al.*, 2017], striking 201°-209° NE, dipping 44°-59° westward with a dominant left-lateral thrust-faulting mechanism (47°-57°) [*Chuang et al.*, 2014; *Canitano et al.*, 2015; *Lin et al.*, 2019]. In this study, we invert GNSS and strain time series to infer a static finite-fault coseismic model of the earthquake. We also present the first evidence of postseismic deformation on the CRF. Indeed, a frictional afterslip is detected by near-source GNSS stations ($\leq$ 25 km from the epicenter) during about 3 months following the mainshock. We characterize the velocity strengthening region of the CRF and its implication during the Ruisui mainshock by combining geodetic and seismological analysis with numerical simulations based on rate-and-state friction mechanics [*Marone et al.*, 1991; *Dieterich*, 1994].

2. Instrumentation and data processing

2.1. Aftershock catalog

We apply the time and spatial double-link cluster-analysis approach [*Wu and Chiao*, 2006] to analyze the aftershock sequence during the first 3 months following the mainshock. We apply the method to the Central Weather Bureau (CWB) catalog after 3-D double-difference relocation [*Wu et al.*, 2008; *Huang et al.*, 2014]. The approach identifies aftershocks via a space-time distance linking and we select 3 days and 5 km as optimal parameters, as widely utilized in Taiwan region [*Hsu et al.*, 2021; *Huang and Wang*, 2022]. We then estimate the completeness magnitude M_c of the aftershock sequence using a magnitude correction factor of 0.1, which corresponds to the size of the event magnitude binning [*Schorlemmer et al.*, 2005]. Using the maximum curvature approach in *ZMAP* software [*Wiemer*, 2001], we infer $M_c = 1.6 \pm 0.1$, and we retain aftershocks with local magnitude $M_L \geq M_c$ (423 events) (Figure 1(b)). We estimate a and b parameters in the Gutenberg-Richter law [*Gutenberg and Richter*, 1944] using a maximum-likelihood approach ($a = 3.671$, $b = 0.653 \pm 0.032$) (Figure 2(a)). b-value is consistent with estimates inferred for thrust-faulting events ($b \sim 0.7$) [*Schorlemmer et al.*, 2005] and with values observed in the Ruisui region ($b \sim$ 0.7-0.8) [*Wu et al.*, 2018]. Finally, the evolution of aftershock activity is explained by the Omori-Utsu law [*Utsu et al.*, 1995] with parameters: $p = 0.99$, $k = 56.2$, and $c = 0.041$ day (Figure 2(b)). p-value estimate represents a typical value for aftershock decay rate (median value of 1.1) [*Utsu et al.*, 1995].

2.2. GNSS data

We process displacement time series for 82 GNSS stations in eastern Taiwan with the *GAMIT10.42/GLOBK5.16* software packages [*Herring et al.*, 2010]. We estimate daily solutions through double-differenced carrier phase measurements. We also utilize additional stations (362 from Taiwan, 8 from Ryukyu and 17 International GNSS Service sites in the Asia-Pacific region) to assess a more accurate pattern of regional deformation for Taiwan. Finally, we process *GAMIT* output with *GLOBK* to estimate daily positions in

ITRF2008 reference frame [*Altamini et al.*, 2012]. Then, we use a Principal component analysis (PCA) [*Dong et al.*, 2006; *Gualandi et al.*, 2014] to estimate horizontal and vertical coseismic offsets related to the Ruisui earthquake. We apply the PCA to 40 GNSS stations over a 2-month period (30 days prior and following the earthquake) (Figure S1 in the Supplementary Information) and permanent coseismic displacements are obtained by fitting the first principal component to a Heaviside function H (Figure 3(a) and Table S1).

To isolate postseismic deformation from signals of both non-tectonic (e.g., hydrological loading cycles [*Hsu et al.*, 2020]) and tectonic origin [*Gualandi et al.*, 2017], we process the displacement time series recorded by 28 near-source stations over a 1.5-year time period (from January 2013 to May 2014). First, we model displacement time series x with a trajectory equation described as follows:

$$x(t) = q + mt + \sum_{i=1}^{n_{eq}} H\left(t - t_{eq}^{(i)}\right) A_{eq}^{(i)} + \sum_{j=1}^{n_{off}} H\left(t - t_{off}^{(j)}\right) A_{off}^{(j)}$$
$$+ A_{yr}\sin\left(2\pi t + \phi_{yr}\right) + A_{hfyr}\sin\left(4\pi t + \phi_{hfyr}\right) + \sum_{i=1}^{n_{eq}} H\left(t - t_{eq}^{(i)}\right) A_{post}^{(i)} \times \left(1 - e^{-\frac{t - t_{eq}^{(i)}}{\tau_{post}^{(i)}}}\right) \tag{1}$$

where q is a constant, m is the secular velocity, t is time, $A_{eq}^{(i)}$ is the coseismic step starting at time $t_{eq}^{(i)}$, n_{eq} is the number of detected earthquakes, $A_{off}^{(j)}$ is instrumental offset at time $t_{off}^{(j)}$, n_{off} is the number of detected offsets, A_{yr} and A_{hfyr} are the amplitudes of the annual and semi-annual seasonal motions with phase shifts ϕ_{yr} and ϕ_{hfyr} respectively, $A_{post}^{(i)}$ is the maximum amplitude of the postseismic displacement with relaxation time $\tau_{post}^{(i)}$. Second, a linear trend and both instrumental and tectonic offsets are removed from position time series (first line in Equation (1)) and we keep all other signals (second line). Finally, we input the corrected time series into a variational Bayesian Independent Component Analysis (vbICA) algorithm [*Choudrey and Roberts*, 2003] adapted to study complex geodetic signals [*Gualandi et al.*, 2016].

The ICA method is an unsupervised learning technique commonly used to resolve blind source separation problems [*Gualandi et al.*, 2016], which allows us to model signals for which the actual temporal functional form is unknown [*Serpelloni et al.*, 2018]. Here we use the vbICA, which assumes that observations are generated by a linear mixture of a limited number of statistically independent sources, because it offers more flexibility in characterizing and extracting sources with multimodal probability density functions, as commonly observed in geophysical time series. We set the number of independent components (IC) using an Automatic Relevance Determination method (nIC = 5) [*Gualandi et al.*, 2016]. The postseismic displacement signal is mapped in the first independent component IC1 and represents the prominent signal in GNSS data for the selected epoch (Figure S2). We infer 11 stations with resolvable postseismic relaxation (cumulative horizontal displacements $\geq$ 3 mm) (Figure S3), mainly located in the earthquake near-source region ($\leq$ 25 km from epicenter).

2.3. Strainmeter data

We estimate dilatation (ϵ_v) coseismic offsets for the 9 *Sacks-Evertson* borehole dilatometers [*Sacks et al.*, 1971] operating during the earthquake. We calibrate the dilatometers through waveform correlation between observed and synthetic tides following *Canitano et al.* [2018a]. We correct the 100-Hz sampling data for solid and ocean tidal strain, air pressure-induced strain and borehole relaxation [*Hsu et al.*, 2015; *Canitano et al.*, 2021] and estimate coseismic strain offsets following *Lin et al.* [2022]. Coseismic static contraction of -900 nϵ to -360 nϵ, well above the measurement noise of $\sim$ 1 nϵ, is recorded by near-field dilatometers (15-20 km SE of the rupture) (Figure 4). Far-field stations (40-60 km away from the rupture) show moderate to little expansion (about 15 nϵ to 35 nϵ), while no coseismic steps are recorded by DONB and FBRB stations.

3. Finite-fault coseismic model

We follow a two-step approach to estimate a finite-fault coseismic slip model. In a first step, we estimate a preliminary model inverting geodetic data for a uniform slip distribution on a single patch. In a second step, we refine the fault discretization. Both solutions are obtained by the joint inversion of horizontal and vertical coseismic displacements for 40 GNSS stations and dilatation for 9 strainmeters. We utilize the *Geodetic Bayesian Inversion Software* (*GBIS*, MATLAB-based software) [*Bagnardi and Hooper*, 2018], which performs a rapid and robust characterization of source fault parameters and associated uncertainties for multiple geodetic datasets using a Bayesian approach and assuming elastic homogeneous half-space Green's function for a rectangular source [*Okada*, 1992]. We assume a rigidity of 30 GPa, as commonly used to model the Earth crust in the region [*Canitano et al.*, 2015]. We modified the *GBIS* algorithm to integrate the calculation of internal deformations together with surface displacements [*Okada*, 1992].

To determine the preliminary source model, we invert for source dimensions and location (length, width, midpoint of the fault upper edge (X, Y, and depth)) and source parameters (strike, dip, uniform slip in the strike and in the dip direction) without imposing constraints onto fault strike (0°-360° clockwise from north), dip (0° to 90° from horizontal) angles and geologic slip direction to explore all possible fault kinematics and orientations. We searched for a fault plane within 15 km from the epicenter with a depth of the midpoint upper edge varying from 0 to 20 km and uniform slip ranging from -1.5 m to 2.0 m (10^6 iterations). We define the weighted misfit between the GNSS observations and the modeled coseismic displacements as follows:

$$misfit_G = \sqrt{\frac{r^T W r}{Tr(W)/3}} \tag{2}$$

where r is the vector of residual displacements between GNSS observations and models, W is the weight matrix, and $Tr(.)$ the matrix trace. The dilatation misfit is estimated as follows (all observations have identical weight):

$$misfit_\epsilon = \sqrt{\frac{\sum_{i=1}^{n}(\epsilon_v^{obs(i)} - \epsilon_v^{mod(i)})^2}{n}} \tag{3}$$

where $\epsilon_v^{obs(i)}$ and $\epsilon_v^{mod(i)}$ are the observed and modeled dilatation for the i^{th} strainmeter, respectively and n is the number of stations ($n = 9$). The source model reveals that surface displacements and dilatation are well explained ($misfit_G = 5$ mm and $misfit_\epsilon = 14$ nϵ) by a left-lateral thrust-fault (rake = 45°-47°) striking 203° and dipping 48° westward (Table S2). This source modeling agrees well with previous models [*Canitano et al.*, 2015; *Lin et al.*, 2019], and is consistent with a rupture on the CRF.

Then, we aim to obtain a more realistic rupture model by discretizing the extended previous fault plane (36 km × 30 km) into 270 subfaults (2 km × 2 km) and solve for slip on each patch. We fix strike and dip angles to values inferred from the uniform-slip model but we allow a variable rake on each subfault to account for the complex rupture pattern [*Lee et al.*, 2014; *Canitano et al.*, 2017]. To avoid unrealistic slip values because of the small amount of constraints west of the fault plane, we apply a zero slip boundary constraint B (unapplied to the plane top edge). A weighted least squares inversion with constraints on smoothness and boundary is performed by minimizing the cost function $\phi(s)$:

$$\phi(s) = \|\Sigma_d^{-1/2}(d - Gs)\|^2 + \beta\|Ls\|^2 + \alpha\|Bs\|^2 \tag{4}$$

where Σ_d is the error covariance matrix, d is GNSS and strain observation matrix, G is the Green's function, s is the slip vector on each subfault and L is the 9-point stencil finite difference Laplacian. β and α are the weighting factors for smoothing and boundary constraints, respectively. We estimate the optimal smoothing factor ($\beta = 152$) by minimizing the leave-one-out cross-validation mean squared error [*Matthews and Segall*, 1993] (Figure S4).

Our preferred model ($misfit_G = 4$ mm and $misfit_\epsilon = 16$ nϵ) (Figure 3(b)) shows that the rupture occurs on a fault plane with dimensions of approximately 26 km $\times$ 22 km located between 3 and 19 km depth (Figure 5). The main asperity is concentrated in a region with dimensions of $\sim$ 16 km $\times$ 10 km located between 6 and 16 km depth, with a peak slip of about 0.5 m located near the hypocenter. The asperity exhibits a dominant left-lateral thrust-faulting mechanism and aftershocks fall both within and at the edge of coseismic slip distribution. The total seismic moment of the rupture is 3.12×10^{18} N.m, corresponding to $M_w = 6.3$, in agreement with other studies [*Chuang et al.*, 2014; *Canitano* *et al.*, 2015]. We estimate the earthquake stress drop $\Delta\tau$ assuming a rectangular rupture [*Kanamori and Anderson*, 1975] and found a value (2 MPa), about twice lower than what obtained with seismological data (3.9 MPa) [*Lee et al.*, 2014] under the assumption of circular fault rupture [*Eshelby*, 1957].

4. Forward model of stress-driven afterslip

Several mechanisms are commonly involved in postseismic transient deformation. Viscoelastic lower crust or upper mantle relaxation can follow moderate-magnitude events ($M_w \sim$ 6-6.5) [*Mandler et al.*, 2021] and is characterized by large-scale and long-lasting deformation (months to years) [*Tang et al.*, 2019]. Here, postseismic relaxation is of short-duration ($\sim$ 3 months) and is mainly recorded by near-source GNSS stations. Poroelastic rebound is generated by changes in pore pressure in the near-source region due to a dislocation [*Peltzer et al.*, 1996]. We calculate the poroelastic deformation following *Li et al.* [2021] protocol for an undrained Poisson's ratio of 0.3. Predicted surface displacements ($\leq$ 1 mm) are one order of magnitude smaller than near-field transient deformation, therefore poroelastic rebound shows no appreciable contribution to postseismic deformation. We thus consider frictional afterslip as the main contributor to the postseismic deformation of the Ruisui earthquake. Typically, afterslip takes place on fault portions surrounding the coseismic rupture. These regions exhibit velocity strengthening behavior and can resist the rupture propagation [*Marone et al.*, 1991]. Afterslip usually represents the predominant deformation mechanism in the postseismic phase during weeks to months after the mainshock [e.g., *Hu et al.*, 2016].

Here, because of the small amount of stations detecting postseismic slip (11 stations) (Figure 1(a)), we are not able to resolve afterslip distribution using the discretized fault plane. Therefore, we perform a forward modeling of stress-driven afterslip to approximate the equivalent effects on the horizontal surface displacements generated by the time dependent slip response v of a fault governed by nonlinear rate strengthening friction parameters [*Dieterich*, 1994] using *Relax* software [*Barbot and Fialko*, 2010a, b], in which afterslip is driven by coseismic shear stress change:

$$v = 2v_0 \exp \frac{-\mu_0}{(a-b)} \sinh \frac{\tau}{(a-b)\sigma} \tag{5}$$

where v_0 represents the reference long-term slip velocity, μ_0 is the static reference friction at depth, a and b are frictional parameters, and τ and σ denote the shear and normal stress changes on the fault, respectively (assumed constant in time). We use the finite-fault coseismic model (26 km $\times$ 22 km) as the stress-driven source and explore parameters v_0, $(a-b)\sigma$, and the dimensions and location of afterslip regions. Given the size of the mainshock and the limited extension of the postseismic deformation, we are seeking for afterslip located in the vicinity of the coseismic slip region. We thus limit our search to the 36 km $\times$ 30 km plane considered for finite-fault modeling (Figure 1(b)). Note that forward modeling simulates relaxation taking place outside of the coseismic source area, which does not preclude the possibility that afterslip and coseismic slip did overlap. We explore two rupture scenarios: afterslip occurs only on the CRF (strike = 203°, dip = 48°, rake = 47°) (Figure S5(a)), and afterslip occurs on the CRF and on the shallow, creeping section of the LVF [*Thomas et al.*, 2014] (about 0-4 km depth) beneath which the CRF may be buried [*Shyu et al.*, 2006]. We model the shallow LVF section with a 5 km-wide receiver striking 20°NE with variable length and location and with a dip of 60° [*Thomas et al.*, 2014] and a rake at the surface of 60° [*Peyret et al.*, 2011] (Figure S5(b)).

In the case of the CRF, we analyze several receiver configurations to seek the simplest model explaining near-source horizontal displacements (Figure S6). Observations are well explained by postseismic relaxation surrounding the coseismic slip region. In particular, we find that shallow relaxation is required to explain observations recorded in the eastern rupture region (e.g., FENP, FONB, HRGN) and NS displacements for near-source stations DNFU and DSIN (Figures 6 and S7). Lateral relaxation on the southwestern fault plane region allows to predict horizontal displacements recorded by KNKO and NHSI stations. Frictional parameters show $v_0 = 5$ mm.yr^{-1}, agreeing with the long-term slip rate of the CRF [*Shyu et al.*, 2020] and $(a-b)\sigma = 3$ MPa, which is about the earthquake stress drop, and is also consistent with estimates for afterslip on continental faults (typically ~ 1 MPa) [*Perfettini and Avouac*, 2004]. This simple, forward relaxation model also explains the absence of detection for remote stations (e.g., YUL1, NPRS, ZCRS or SHUL) but tends to overestimate displacements for stations located south of the rupture (JSUI and CMRS) and to underestimate EW displacements for stations located right above the hypocenter (GUFU and DSIN) (Figure 7). Finally, adding the shallow section of the LVF as a passive fault in the forward modeling does not improve displacement modeling (Figure S8), suggesting that the fault did not appreciably contribute to postseismic stress relaxation.

5. Aftershock activity possibly mediated by frictional afterslip

To explore a possible connection between aftershock activity and afterslip, we first compare the cumulative seismicity with the afterslip temporal function mapped in IC1 component (Figure 8(a)). We observe a good correlation between the signals, which suggests that afterslip may represent the driving force behind aftershock productivity during the Ruisui sequence [*Perfettini and Avouac*, 2004; *Hsu et al.*, 2006; *Gualandi et al.*, 2020]. Besides, seismicity rate and postseismic relaxation decays are well explained by the Omori-Utsu law with p-value $= 1$ (Figure 2(b)). This particular case also reflects a temporal seismicity decay compatible with resisting stress on the fault plane increasing as the logarithm of the sliding velocity, as typically observed during afterslip [*Dieterich*, 1994; *Perfettini et al.*, 2018].

To further investigate how seismic and aseismic transient slip interact during the postseismic period, we analyze the spatiotemporal evolution of aftershocks. In particular, we seek a possible expansion of the aftershock region reflecting aftershock migration driven by afterslip [*Frank et al.*, 2017; *Perfettini et al.*, 2018]. For a rate strengthening rheology, the aftershock region expansion with time $\Delta R_a(t)$, since the onset time t_i of the first aftershock, is expressed as [*Perfettini et al.*, 2018]:

$$\Delta R_a(t) = \zeta(a-b)\sigma\frac{c}{\Delta\tau}\log\left(\frac{t}{t_i}\right) \tag{6}$$

where ζ is a constant and c represents the source radius assuming a circular crack model following *Eshelby* [1957]:

$$c = \left(\frac{7}{16}\frac{M_0}{\Delta\tau}\right)^{1/3} \tag{7}$$

We model the aftershock zone expansion using parameters related to our coseismic model ($c = 8.80$ km, $\Delta\tau = 2$ MPa) and we also test *Lee et al.* [2014] model ($c = 7.05$ km, $\Delta\tau = 3.9$ MPa). We assume $M_0 = 3.12\times10^{18}$ N.m, $(a-b)\sigma = 3$ MPa, $\zeta = 1$ [*Frank et al.*, 2017] and $t_i = 194$ s.

We observe that apparent propagation velocity shows substantial differences for these coseismic models using $(a-b)\sigma$ constrained from rate-and-state simulations (Figure 8(b), purple and blue curves). Aftershock propagation velocity is well reproduced using *Lee et al.* [2014] coseismic parameters while our model tends to overestimate migration speed by a factor of about 3. However, since *Lee et al.* [2014] coseismic model shows greater resolution and related static stress drop was estimated under the assumption of circular fault rupture [*Eshelby*, 1957], we may expect a good estimate of aftershock spatiotemporal evolution. Conversely, our model is probably too complex to assume circular rupture (Figure 5), so that stress drop is estimated based on a rectangular rupture [*Kanamori and Anderson*, 1975]. We can note that $(a-b)\sigma$ parameter also strongly impacts migration pattern. For instance, a value of $(a-b)\sigma = 1$ MPa (which also yields a reasonable fit to postseismic signals) would allow to predict well expansion velocity using our coseismic model (Figure 8(b), green curve). Overall, the absence of resolution for characterizing afterslip that possibly occurs in the coseismic slip region (where most of aftershocks are located) limits our ability to investigate further the impact of afterslip on seismicity during the postseismic phase of the Ruisui earthquake.

6. Discussion

We analyze GNSS, strain, and seismological time series to investiage the spatiotemporal evolution of crustal deformation related to the 2013 Ruisui earthquake. We observe that the fault plane geometry and location inferred from the joint geodetic inversion agree well with previous models [e.g., *Chuang et al.*, 2014; *Lin et al.*, 2019]. Our finite-fault model shows that the rupture is distributed on a 26 km $\times$ 22 km fault plane located at a depth of about 3 to 19 km. The absence of surface ruptures directly above the mainshock was also reported previously [*Lee et al.*, 2014; *Chuang et al.*, 2014]. The dimension and location of the main asperity are consistent with *Lee et al.* [2014] model, but the coseismic slip is underestimated by approximately 30%. *Lee et al.* [2014] have also inferred a second, shallow asperity (with average slip of 0.3-0.4 m) in the SW section of the fault plane associated with a left-lateral slip component. Our model possibly shows shallow slip ($\sim$ 3 to 9 km depth) (Figure 5) in the SW termination of the rupture associated with a dominant left-lateral slip component and which concentrates a small cluster of aftershocks, albeit with limited resolution. Finally, we observe that near-source deformation (recorded by HGSB, SSNB, CHMB, and ZANB), previously used to infer the mainshock source parameters [*Canitano et al.*, 2015], is well explained ($misfit_{\epsilon} = 1.0$ nϵ) (Figure 4). Since joint geodetic inversion is dominated by GNSS and strain observations recorded in the near-source region, far-field deformation (e. g., SJNB and TRKB) is likely underestimated by our model.

While the existence of aseismic transient slip regions on the CRF was previously suggested based on geodetic [*Canitano et al.*, 2019] and seismological (seismic swarms, repeating earthquakes) [*Chen et al.*, 2020; *Peng et al.*, 2021] observations, the Ruisui earthquake reveals unambiguously the presence of velocity strengthening regions capable of sustaining transient deformation over months. Using frictional rate-and-state parameters from our optimal relaxation model, we simulate the spatial evolution of postseismic slip on the CRF plane as a function of time (Figure 9). We observe that during the early postseismic phase (first 2 weeks to 1 month), afterslip spreads around the coseismic slip region with relatively limited slip (< 0.1 m). Then, postseismic slip increases in the shallow fault section, reaching a maximum cumulative slip of approximately 0.15 m about 3 months following the mainshock. The velocity strengthening region extends toward the surface and mainly covers the fault region located right above the main asperity (Figure 5). We estimate the total moment released by the 3-month afterslip considering the slip associated with the $0.5^\circ \times 0.5^\circ$ cells distributed on the plane inferred from GNSS forward modeling (30 km $\times$ 30 km) (Figure 7). We infer a moment of about 6.73×10^{17} N.m ($M_w \sim 5.8$), that represents about 20% of the cumulative seismic moment. Typically, ratio estimates for thrust-faulting earthquakes with $M_w \sim 6$ to 6.5 range from about 10% to 30% [*Hawthorne et al.*, 2016]. However, since aftershocks appear to be primarily driven by afterslip, the fraction of postseismic slip that possibly occurs within the coseismic area remains unknown. Finally, the cumulative seismic moment released by aftershocks (423 events with $M_L \geq 1.6$) is $M_0 \sim 2.56\times10^{16}$ N.m ($M_w = 4.9$) which represents less than 4% of the minimum cumulative moment released by afterslip. Consequently, aseismic slip represents the dominant mechanism of postseismic deformation, a commonly observed pattern in active regions [e.g., *Gualandi et al.*, 2020].

The presence of the shallow afterslip-prone region, possibly highly fractured [*Lee et al.*, 2014], has contributed to relieve stress aseismically in the postseismic phase, but may have also arrested the rupture propagation, acting as a barrier that impeded locally seismic slip to reach the surface [*Rolandone et al.*, 2018]. Rupture propagation toward the surface arrested by shallow fault creep was observed during the 2003 Chengkung earthquake [*Hsu et al.*, 2009; *Thomas et al.*, 2014] or during the 2020 Elazig (Turkey) event [*Cakir et al.*, 2023], for instance. Indeed, a field survey conducted shortly after the Ruisui earthquake reported the absence of surface fractures in the region located right above the main coseismic zone while fractures were found further south, near the southwestern rupture termination [*Lee et al.*, 2014], suggesting that coseismic slip has possibly penetrated the surface. Seismic rupture propagation may have been impacted by the spatially heterogeneous properties of the velocity strengthening area that shows the largest postseismic slip level right above the main coseismic zone and a smaller amount above the SW rupture section (Figure 9). Seismic rupture can partially or completely penetrate a region of transient deformation provided effective stress difference between coseismic and aseismic regions is large enough to facilitate it [*Lin et al.*, 2020]. The presence of this shallow transient zone may also be compatible with the very low level of historical seismicity on the shallow section of the CRF in the Ruisui region (Figure 7(b)). Overall, further investigations are needed to constrain the rheological properties of the CRF and to understand the mechanisms that contribute to relieving the strain accumulated in the crust.

7. Conclusions

The 2013 Ruisui earthquake represents the first unequivocal evidence of the activity of the CRF in central LV. In this study, combining geodetic and seismological observations with numerical simulations based on rate and state-dependent friction, we present the first evidence of postseismic transient deformation on the CRF. We observe that afterslip represents the dominant mechanism during the postseismic period, releasing $> 95\%$ of the moment through aseismic slip on the CRF. Further, we demonstrate that afterslip also likely acts as the driving force controlling aftershock productivity and the spatiotemporal migration of seismicity during the first 3 months following the mainshock. Such a mechanism was previously observed on the LVF [*Canitano et al.*, 2018b] and we present the first evidence that the CRF can also experience complex interactions between aseismic and seismic slip in the postseismic phase. Finally, since the 2022 Chihshang earthquake revealed that the CRF can generate major earthquakes ($M_w > 7$) but also that both the CRF and LVF southern fault segments might be connected and might ruptured together during a seismic event [*Lee et al.*, 2023], enhancing detection and characterization of aseismic fault slip in the LV will be fundamental to reducing earthquake hazards in Taiwan in the future.

Acknowledgments

The authors thank the Carnegie Institution of Washington for helping with the strainmeter project. We are grateful to IES staff for helping with GNSS data. We thank Marco Bagnardi for valuable comments concerning GBIS software.

Data Availability Statement

All GNSS, strainmeter, and aftershock catalog data and slip inversion codes used in this study are available at https://doi.org/10.5281/zenodo.7803958 [*Lin*, 2023]. The open-source Geodetic Bayesian Inversion Software (GBIS) is available from *Bagnardi and Hooper* [2018] at https://comet.nerc.ac.uk/gbis/. The Relax v1.0.7 software is available via https://geodynamics.org. Some figures are plotted with the Generic Mapping Tools [*Wessel and Smith*, 1998].

References

Altamini, Z., L. Métivier and X. Collilieux (2012), ITRF2008 plate motion model, *J. Geophys. Res.*, *117*, doi:10.1029/2011JB008930.

Bagnardi, M. and A. Hooper (2018), Inversion of surface deformation data for rapid estimates of source parameters and uncertainties: A Bayesian approach, *Geochem. Geophys. Geosystems*, *19*, 2194–2211.

Barbot, S. and Y. Fialko (2010a), Fourier-domain Green's function for an elastic semi-infinite solid under gravity, with applications to earthquake and volcano deformation, *Geophys. J. Int.*, *182*(2), 568–582.

Barbot, S. and Y. Fialko (2010b), A unified continuum representation of postseismic relaxation mechanisms: Semi-analytic models of afterslip, poroelastic rebound and viscoelastic flow, *Geophys. J. Int.*, *182*(3), 1124–1140.

Barrier, E. and J. Angelier (1986), Active collision in eastern Taiwan: the Coastal Range, *Tectonophysics*, *125*, 39–72.

Biq, C. (1965), The East Taiwan Rift, *Pet. Geol. Taiwan*, *4*, 93–106.

Cakir, Z., U. Dogan, A. M. Akoglu, S. Ergintav, S. Ozarpaci, A. Ozdemir, T. Nazadkhalil, N. Cakir, C. Zabci, M. H. Erkoc, M. Basmenji, M. Kokum and R. Bilham, Arrest of the M_w 6.8 January 24, 2020 Elazig (Turkey) earthquake by shallow fault creep, *Earth Planet. Sci. Lett.*, *608*, doi:10.1016/j.epsl.2023.118085.

Canitano, A., Y. J. Hsu, H. M. Lee, A. T. Linde and S. Sacks (2015), Near-field strain observations of the October 2013 Ruisui, Taiwan, earthquake: source parameters and limits of very-short term strain detection, *Earth Planets Space*, *67*, 125, doi:10.1186/s40623-015-0284-1.

Canitano, A., Y. J. Hsu, H. M. Lee, A. T. Linde and S. Sacks (2017), A first modeling of dynamic and static crustal strain field from near-field dilatation measurements: example of the 2013 M_w 6.2 Ruisui earthquake, Taiwan, *J. Geodesy*, *91*(1), 1–8.

Canitano, A., Y. J. Hsu, H. M. Lee, A. T Linde and S. Sacks (2018a), Calibration for the shear strain of 3-component borehole strainmeters in eastern Taiwan through Earth and ocean tidal waveform modeling, *J. Geodesy*, *92*(3), 223–240.

Canitano, A., M. Godano, Y. J. Hsu, H. M. Lee, A. T. Linde and S. Sacks (2018b), Seismicity controlled by a frictional afterslip during a small magnitude seismic sequence ($M_L < 5$) on the Chihshang Fault, Taiwan, *J. Geophys. Res. Solid Earth*, *123*(2), 2003–2018, doi:10.1002/2017JB015128.

Canitano, A., H. Gonzalez-Huizar, Y. J. Hsu, H. M. Lee, A. T. Linde and S. Sacks (2019), Testing the influence of static and dynamic stress perturbations on the occurrence of a shallow, slow slip event in eastern Taiwan, *J. Geophys. Res. Solid Earth*, *124*(3), 3073–3087, doi:10.1029/2018JB016742.

Canitano, A., M. Godano and M. Y. Thomas (2021), Inherited state of stress as a key factor controlling slip and slip mode: inference from the study of a slow slip event in the Longitudinal Valley, Taiwan, *Geophys. Res. Lett.*, *48*, doi:10.1029/2020GL090278.

Chen, Y., K. H. Chen, J. C. Hu and J. C. Lee (2020), Probing the variation in aseismic slip behavior around an active suture zone: observations of repeating earthquakes in Eastern Taiwan, *J. Geophys. Res. Solid Earth*, *125*(5), doi:10.1029/2019JB018561.

Choudrey, R. A. and S. J. Roberts (2003), Variational mixture of Bayesian independent component analyzers, *Neural Comput.*, *15*(1), 213–252.

Chuang, R. Y., K. M. Johnson, Y. T. Kuo, Y. M. Wu, C. H. Chang and L. C. Kuo (2014), Active back thrust in the eastern Taiwan suture revealed by the 2013 Rueisuei earthquake: evidence for a doubly vergent orogenic wedge ?, *Geophys. Res. Lett.*, *41*, 3464–3470.

Dieterich, J. (1994), A constitutive law for rate of earthquake production and its application to earthquake clustering, *J. Geophys. Res.*, *99*(B2), 2601–2618.

Dong, D., P. Fang, Y. Bock, F. Webb, L. Prawirodirdjo, S. Kedar and P. Jamason (2006), Spatiotemporal filtering using principal component analysis and Karhunen-Loeve expansion approaches for regional GPS network analysis, *J. Geophys. Res.*, *111*, B03405, doi:10.1029/2005JB003806.

Eshelby, J. D. (1957), The determination of the elastic field of an ellipsoid inclusion and related problems, *Proc. R. Soc. London A*, *241*, 376–396.

Frank, W. B., P. Poli and H. Perfettini (2017), Mapping the rheology of the Central Chile subduction zone with aftershocks, *Geophys. Res. Lett.*, *44*, 5374–5382.

Gualandi, A., E. Serpelloni and M. E. Belardinelli (2014), Space-time evolution of crustal deformation related to the M_w 6.3, 2009 L'Aquila earthquake (central Italy) from principal component analysis inversion of GPS position time-series, *Geophys. J. Int.*, *197*, 174–191.

Gualandi, A., E. Serpelloni and M. E. Belardinelli (2016), Blind source separation problem in GPS time series, *J. Geodesy*, *90*, 323–341.

Gualandi, A., C. Nichele, E. Serpelloni, L. Chiaraluce, D. Latorre, M. E. Belardinelli and J. P. Avouac (2017), Aseismic deformation associated with an earthquake swarm in the northern Apennines (Italy), *Geophys. Res. Lett.*, *42*, doi:10.1002/2017GL073687.

Gualandi, A., Z. Liu and C. Rollins (2020), Post-large earthquake seismic activities mediated by aseismic deformation processes, *Earth Planet. Sci. Lett.*, *530*, doi: 10.1016/j.epsl.2019.115870.

Gutenberg, R. and C. F. Richter (1944), Frequency of earthquakes in California, *Bull. Seismol. Soc. Am.*, *34*, 185–188.

Hawthorne, J. C., M. Simons and J.-P. Ampuero (2016), Estimates of aseismic slip associated with small earthquakes near San Juan Bautista, CA, *J. Geophys. Res. Solid Earth*, *121*, 8254–8275.

Herring, T., W. King and S. M. McCluskey (2010), Introduction to GAMIT/GLOBK release 10.4., *Mass. Inst. of Technol., Cambridge.*

Hsu, Y. J., M. Simons, J. P. Avouac, J. Galetzka, K. Sieh, M. Chlieh, D. Natawidjaja, L. Prawirodirdjo and Y. Bock (2006), Frictional afterslip following the 2005 Nias-Simeulue earthquake, Sumatra, *Science*, *312*, 1921–1926.

Hsu, Y. J., S. B. Yu and H. Y. Chen (2009), Coseismic and postseismic deformation associated with the 2003 Chengkung, Taiwan, earthquake, *Geophys. J. Int.*, *176*, 420–430.

Hsu, Y. J., Y. S. Chang, C. C. Liu, H. M. Lee, A. T. Linde, S. Sacks, G. Kitagawa and Y. G. Chen (2015), Revisiting borehole strain, typhoons, and slow earthquakes using quantitative estimates of precipitation-induced strain changes, *J. Geophys. Res. Solid Earth*, *120*(6), 4556–4571.

Hsu, Y. J., Y. Fu, R. Bürgmann, S. Y. Hsu, C. C. Lin, C. H. Tang and Y. M. Wu (2020), Assessing seasonal and interannual water storage variations in Taiwan using geodetic and hydrological data, *Earth Planet. Sci. Lett.*, *550*, doi:10.1016/j.epsl.2020.116532.

Hsu, Y. J., H. Kao, R. Bürgmann, Y. T. Lee, H. H. Huang, H. F. Hsu, Y. M. Wu and J. Zhuang (2021), Synchronized and asynchronous modulation of seismicity by hydrological loading: A case study in Taiwan, *Sci. Adv.*, *7:eabf7282*.

Hu, Y., R. Bürgmann, N. Uchida, P. Banerjee and J. T. Freymueller (2016), Stress-driven relaxation of heterogeneous upper mantle and time-dependent afterslip following the 2011 Tohoku earthquake, *J. Geophys. Res. Solid Earth*, *121*, 385–411.

Huang, H. H., Y. M. Wu, X. Song, C. H. Chang, S. J. Lee, T. M. Chang and H. H. Hsieh (2014), Joint V_p and V_s tomography of Taiwan: implications for subduction-collision orogeny, *Earth Planet. Sci. Lett.*, *392*, 177–191.

Huang, H H. and Y. Wang (2022), Seismogenic structure beneath the northern Longitudinal Valley revealed by the 2018-2021 Hualien earthquake sequences and 3-D velocity model, *Terr. Atmos. Ocean. Sci.*, *33:17*, doi:10.1007/s44195-022-00017-z.

Hwang, R D., Y. L. Huang, W. Y. Chang, C. Y. Lin, C. Y. Lin, S. T. Wang, J. B. Chan, J. P. Chang and T. W. Lin (2022), Radiated seismic energy from the 2021 M_L 5.8 and M_L 6.2 Shoufeng (Hualien), Taiwan, earthquakes and their aftershocks, *Terr. Atmos. Ocean. Sci.*, *33:19*, doi:10.1007/s44195-022-00020-4.

Kanamori, H. and D. L. Anderson (1975), Theoretical basis of some empirical relation in seismology, *Bull. Seismol. Soc. Am.*, 65(5), 1073–1095.

Lee, S. J., H. H. Huang, J. B. H. Shyu, T. Y. Yeh and T. C. Lin (2014), Numerical earthquake model of the 31 October 2013 Ruisui, Taiwan, earthquake: source rupture process and seismic wave propagation, *J. Asian Earth Sci.*, *96*, 374–385.

Lee, S. J., T. P. Wong, T. Y. Liu, T. C. Lin and C. T. Chen (2020), Strong ground motion over a large area in northern Taiwan caused by the northward rupture directivity of the 2019 Hualien earthquake, *J. Asian Earth Sci.*, *192*, 104095, doi: 10.1016/j.jseaes.2019.104095.

Lee, S. J., T. Y. Liu and T. C. Lin (2023), The role of the westdipping collision boundary fault in the Taiwan 2022 Chihshang earthquake sequence, *Sci. Rep.*, *13:3552*, doi: 10.1038/s41598-023-30361-0.

Li, S., T. Tao, Y. Chen, P. He, F. Gao, X. Qu and Y. Zhou (2021), Geodetic observation and modeling of the coseismic and postseismic deformation associated with the 2020 M_w 6.5 Monte Cristo earthquake, *Earth and Space Science*, *8*, doi:10.1029/2021EA001696.

Lin, J. T., W. L. Chang, D. Melgar, A. M. Thomas and C. Y. Chiu (2019), Quick determination of earthquake source parameters from GPS measurements: a study of suitability for Taiwan, *Geophys. J. Int.*, *219*, 1148-1162.

Lin, J. T., K. S. Aslam, A. M. Thomas and D. Melgar (2020), Overlapping regions of coseismic and transient slow slip on the Hawaiian décollement, *Earth Planet. Sci. Lett.*, *544*, doi:10.1016/j.epsl.2020.116353.

Lin, H. F., Y. F. Hsu and A. Canitano (2022), Source modeling of the 2009 Fengpin-Hualien earthquake sequence, Taiwan, inferred from static strain measurements, *Pure Appl. Geophys.*, *179*, doi:10.1007/s00024-022-03068-y.

Lin, H. F. (2023), Interplay between seismic and aseismic deformation on the Central Range fault during the 2013 Mw 6.3 Ruisui earthquake (Taiwan) [Dataset]. Zenodo. https://doi.org/10.5281/zenodo.7803958.

Mandler, E., F. Pintori, A. Gualandi, L. Anderlini, E. Serpelloni and M. E. Belardinelli (2021), Post-seismic deformation related to the 2016 Central Italy seismic sequence from GPS displacement time-series, *J. Geophys. Res. Solid Earth*, *126*, doi:10.1029/2021JB022200.

Marone, C. J., C. H. Scholz and R. Bilham (1991), On the mechanics of earthquake afterslip, *J. Geophys. Res.*, *96*, 8441–8452.

Matthews, M. V. and P. Segall (1993), Estimation of depth-dependent fault slip from measured surface deformation with application to the 1906 San Francisco earthquake, *J. Geophys. Res.*, *98*, 12,153–12,163.

Mozziconacci, L., B. Delouis, B. S. Huang, J. C. Lee and N. Béthoux (2013), Determining fault geometry from the distribution of coseismic fault slip related to the 2006 Taitung earthquake, eastern Taiwan, *Bull. Seismol. Soc. Am.*, *103*, 394–411.

Okada, Y. (1992), Internal deformation due to shear and tensile faults in a half-space, *Bull. Seism. Soc. Am.*, *82*(2), 1018–1040.

Peltzer, G., P. Rosen, F. Rogez and K. Hudnut (1996), Postseismic rebound in fault step-overs caused by pore fluid flow, *Science*, *273*(5279), 1202–1204.

Peng, W., D. Marsan, K. H. Chen and E. Pathier (2021), Earthquake swarms in Taiwan: a composite declustering method for detection and their spatial characteristics, *Earth Planet. Sci. Lett.*, *574*, doi:10.1016/j.epsl.2021.117160.

Perfettini, H. and J. P. Avouac (2004), Postseismic relaxation driven by brittle creep: A possible mechanism to reconcile geodetic measurements and the decay rate of aftershocks, application to the Chi-Chi earthquake, Taiwan, *J. Geophys. Res.*, *109*, B02304, doi:10.1029/2003JB002488.

Perfettini, H., W. B. Frank, D. Marsan and M. Bouchon (2018), A model of aftershock migration driven by afterslip, *Geophys. Res. Lett.*, *45*, 2283–2293.

Peyret, M., S. Dominguez, R. Cattin, J. Champenois, M. Leroy and A. Zajac (2011), Present-day interseismic surface deformation along the Longitudinal Valley, eastern Taiwan, from a PS-InSAR analysis of the ERS satellite archives, *J. Geophys. Res.*, *116*, B03402, doi:10.1029/2010JB007898.

Rolandone, F., J. M. Nocquet, P. A. Mothes, P. Jarrin, M. Vallée, N. Cubas, S. Hernandez, M. Plain, S. Vaca and Y. Font (2018), Areas prone to slow slip events impede earthquake rupture propagation and promote afterslip, *Sci. Adv.*, *4*, eaao6596.

Rousset, B., S. Barbot, J. P. Avouac and Y. J. Hsu (2012), Postseismic deformation following the 1999 Chi-Chi earthquake, Taiwan: implication for lower-crust rheology, *J. Geophys. Res.*, *117*, B12405, doi:10.1029/2012JB009571.

Sacks, S., S. Suyehiro, D. W. Evertson and Y. Yamagishi (1971), Sacks-Evertson strainmeter, its installation in Japan and some preliminary results concerning strain steps, *Pap. Meteorol. Geophys.*, *22*, 195–208.

Schorlemmer, D., S. Wiemer and M. Wyss (2005), Variations in earthquake-size distribution across different stress regimes, *Nature*, *437*, 539–542.

Serpelloni, E., F. Pintori, A. Gualandi, E. Scoccimarro, A. Cavaliere, L. Anderlini, M. E. Belardinelli and M. Todesco (2018), Hydrologically induced karst deformation: Insights from GPS measurements in the Adria-Eurasia plate boundary zone, *J. Geophys. Res. Solid Earth*, *123*, 4413–4430.

Shyu, J. B. H., K. Sieh, Y. G. Chen and L. H. Chung (2006), Geomorphic analysis of the Central Range fault, the second major active structure of the Longitudinal Valley suture, eastern Taiwan, *Geol. Soc. Am. Bull.*, *118*, 1447–1462.

Shyu, J. B. H., Y. H. Yin, C. H. Chen, Y. R. Chuang and S. C Liu (2020), Updates to the on-land seismogenic structure source database by the Taiwan Earthquake Model (TEM) project for seismic hazard analysis of Taiwan, *Terr. Atmos. Ocean. Sci.*, *31*(4), 469–478.

Tang, C. H., Y. J. Hsu, S. Barbot, J. D. P. Moore and W. L Chang (2019), Lower-crustal rheology and thermal gradient in the Taiwan orogenic belt illuminated by the 1999 Chi-Chi earthquake, *Sci. Adv.*, *5*(2), doi:10.1126/sciadv.aav3287.

Thomas, M. Y., J. P. Avouac, J. Champenois, J. C. Lee and L. C. Kuo (2014), Spatiotemporal evolution of seismic and aseismic slip on the Longitudinal Valley Fault, Taiwan, *J. Geophys. Res.*, *119*(6), 5114–5139.

Utsu, T., Y. Ogata and R. S. Matsu'ura (1995), The centenary of the Omori formula for a decay law of aftershock activity, *J. Phys. Earth*, *43*, 1–33.

Wen, Y. Y. (2018), Source characteristics of the northern Longitudinal Valley, Taiwan derived from broadband strong-motion simulation, *Pure Appl. Geophys.*, *175*, 587–596.

Wessel, P. and W. H. F. Smith (1998), New, improved version of the Generic Mapping Tools released, *Eos Trans. AGU*, *79*, 579, doi:10.1029/98EO00426.

Wiemer, S. (2001), A software package to analyze seismicity: ZMAP, *Seismol. Res. Lett.*, *72*(3), 373–382.

Wu, Y. M. and L. Y. Chiao (2006), Seismic quiescence before the 1999 Chi-Chi, Taiwan, M_w 7.6 earthquake, *Bull. Seismol. Soc. Am.*, *96*(1), 321–327.

Wu, Y. M., C. H. Chang, L. Zhao, T. L. Teng and M. Nakamura (2008), A comprehensive relocation of earthquakes in Taiwan from 1991 to 2005, *Bull. Seismol. Soc. Am.*, *98*, 1471–1481.

Wu, Y. M., S. K. Chen, T. C. Huang, H. H. Huang, W. A. Chao and I. Koulakov (2018), Relationship between earthquake b-values and crustal stresses in a young orogenic belt, *Geophys. Res. Lett.*, *45*, 1832–1837.

Yagi, Y., R. Okuwaki, B. Enescu and J. Lu (2023), Irregular rupture process of the 2022 Taitung, Taiwan, earthquake sequence, *Sci. Rep.*, *13:1107*, doi:10.1038/s41598-023-27384-y.

Yu, S. B. and L. C. Kuo (2001), Present-day crustal motion along the Longitudinal Valley Fault, eastern Taiwan, *Tectonophysics*, *333*, 199–217.

Figure 1: (a) Map of eastern Taiwan. The red and black triangles denote the strainmeters and GNSS stations, respectively. GNSS stations used for constraining postseismic relaxation are outlined (green box: stations recording surface displacements, and red box: stations with no displacements). The red star depicts the epicenter of the Ruisui earthquake (CGMT). The blue stars denote the epicenters of moderate to large earthquakes ($M_w \geq 5.9$) that struck the CRF from 2006 to 2022. The black dot shows Ruisui town. The black box shows the region in (b). (Inset) Geodynamic framework of Taiwan. The black arrow indicates the relative motion between the Philippine Sea plate (PSP) and Eurasian plate (EP); (RT): Ryukyu Trench. LVF: Longitudinal Valley fault; CRF: Central Range fault; LV: Longitudinal Valley. (b) Surface projection of the spatiotemporal evolution of the relocated aftershocks (with $M_L \geq 1.6$) during the first 3 months following the mainshock. Surface projection of the relocated plane used for finite-fault geodetic inversion (36 km $\times$ 30 km) (black rectangle) and of the main region of coseismic slip (26 km $\times$ 22 km) (red rectangle). The thick line depicts the top edge of each plane.

Figure 2: (a) Cumulative frequency-magnitude distribution of aftershocks during about 3 months following the mainshock. The dashed line represents the Gutenberg-Richter law ($log_{10}(N) = a - bM$, where N is the cumulative number of earthquakes having magnitudes larger than M) with $a = 3.671$ and $b = 0.653 \pm 0.032$ obtained via a maximum-likelihood approach. The magnitude of completeness ($M_c = 1.6 \pm 0.1$) for the sequence is estimated using a maximum curvature approach. (b) Cumulative number of aftershocks (N) over a $\sim$ 3-month period following the mainshock (after removing events with $M_L < M_c$) approximated with the cumulative Omori-Utsu law

($N(t) = K(c^{1-p} - (t+c)^{1-p})/(p-1)$, where K, c and p are constants).

Figure 3: Comparison of observed and modeled 3-D coseismic displacements associated with the 2013 Ruisui earthquake. (a) GNSS coseismic displacements obtained through a PCA approach (see Figure 1(a) for station details). Black vectors show horizontal displacements with a 95% confidence ellipse and circles show vertical displacements with uplift and subsidence indicated by warm and cold colors, respectively. The black star denotes the mainshock epicenter. (b) Modeled horizontal displacements (red arrows) and residual of vertical displacements (circles) inferred from the nonlinear joint inversion of GNSS and strain time series for a finite-fault model (Figure 5). The black thick line depicts the top edge of the fault plane and the dashed lines outline its surface projection.

Figure 4: Coseismic static dilatation offsets recorded by *Sacks-Evertson* borehole dilatometers over a 30-min period centered on the Ruisui earthquake onset timing. Expansion is positive.

Figure 5: Coseismic slip distribution resolved on 2 km $\times$ 2 km subfaults ($\beta = 152$). The dashed black rectangle denotes the $\sim$ 26 km $\times$ 22 km fault plane hosting the rupture. The projection onto the fault plane of the mainshock epicenter is depicted by a black star and black dots show the projection of relocated aftershocks (with $M_L \geq 1.6$) occurring during the first 3 months following the mainshock.

Figure 6: Temporal evolution of stress-driven afterslip induced on the CRF over a 3-month period inferred from our best source combination (Figure 7(a)) (see Figure S7 for additional examples).

Figure 7: (a) Horizontal postseismic displacements detected by near-source GNSS stations estimated using a vbICA approach (black arrows) and predictions resulting from a forward nonlinear rate strengthening friction model (purple arrows). Near-source stations with insignificant detections are shown by red triangles. The purple rectangle outlines the receiver located on the CRF considered in the simulation. The thick line depicts the top edge of each plane. The plain red rectangle outlines the main coseismic slip region (stress-driven source) and the black star is the mainshock epicenter. (b) Relocated seismicity ($M_L \geq 1.5$) in central LV from 1990 to 2020 from the CWB. Relocated aftershocks of the Ruisui earthquake are shown by black dots. The shallow section of the CRF in the Ruisui region is associated with a very low level of historical seismicity.

Figure 8: (a) Comparison between the cumulative number of aftershocks (with M_L ≥ 1.6) and the temporal evolution of afterslip (IC1 component). (b) Along-strike expansion of the aftershock zone of the Ruisui earthquake predicted using Equation (6).

Figure 9: Spatiotemporal evolution of postseismic slip along the CRF (Equation (5)) inferred from our optimal parameters ($v_0 = 5$ mm.yr^{-1}, $(a-b)\sigma = 3$ MPa). Postseismic relaxation surrounds the coseismic slip region (dark blue region) with average slip of ~ 0.05-0.1 m and shows a spatially heterogeneous distribution in the shallow fault sec-

tion, with maximum cumulative slip of approximately 0.15 m about 3 months following the mainshock.

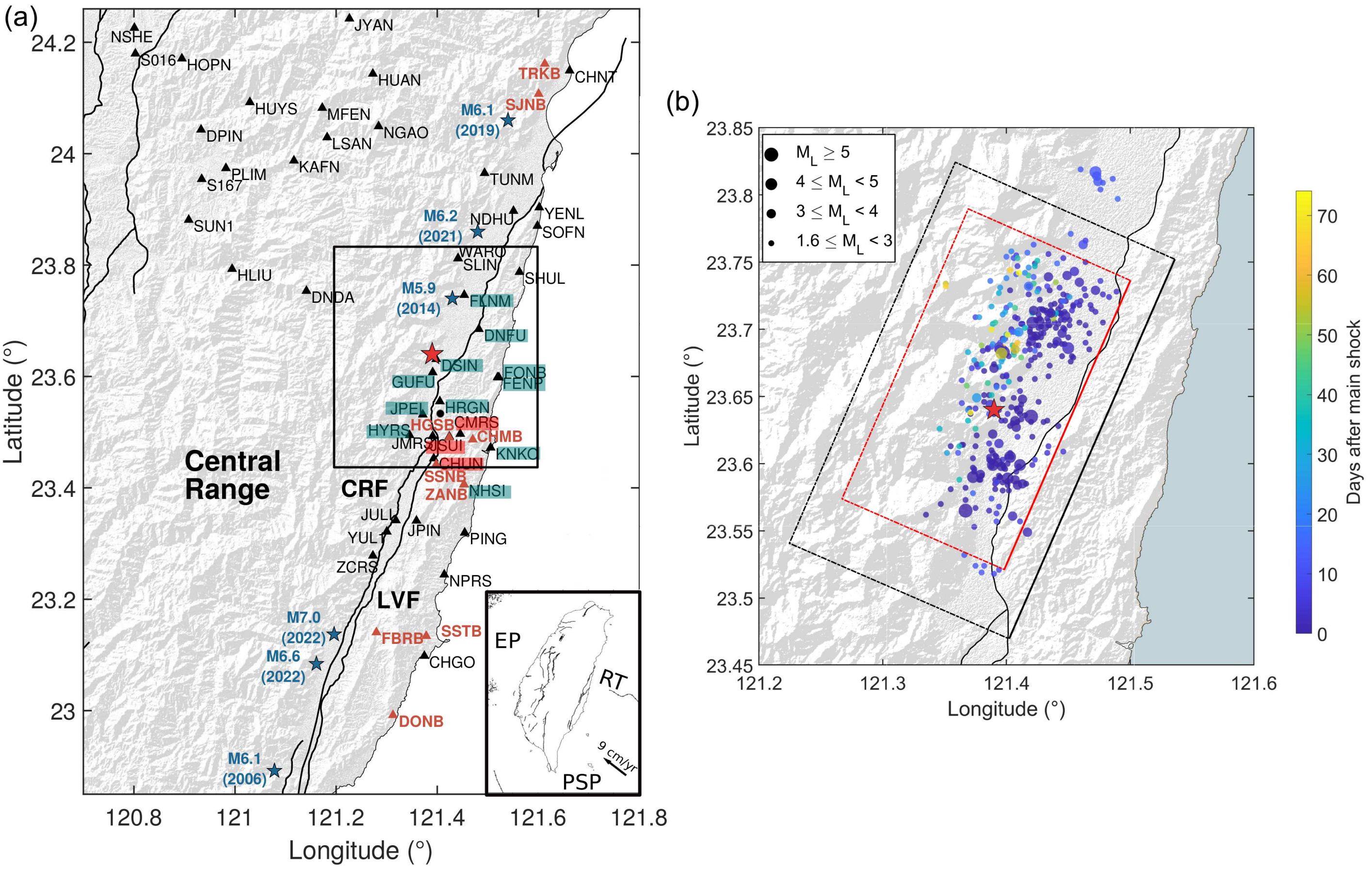
(a)
Central Range
CRF
LVF
EP
RT
PSP
9 cm/yr
M6.1 (2019)
M6.2 (2021)
M5.9 (2014)
M7.0 (2022)
M6.6 (2022)
M6.1 (2006)
Latitude (°)
Longitude (°)
(b)
Days after main shock
Latitude (°)
Longitude (°)

Figure 1.

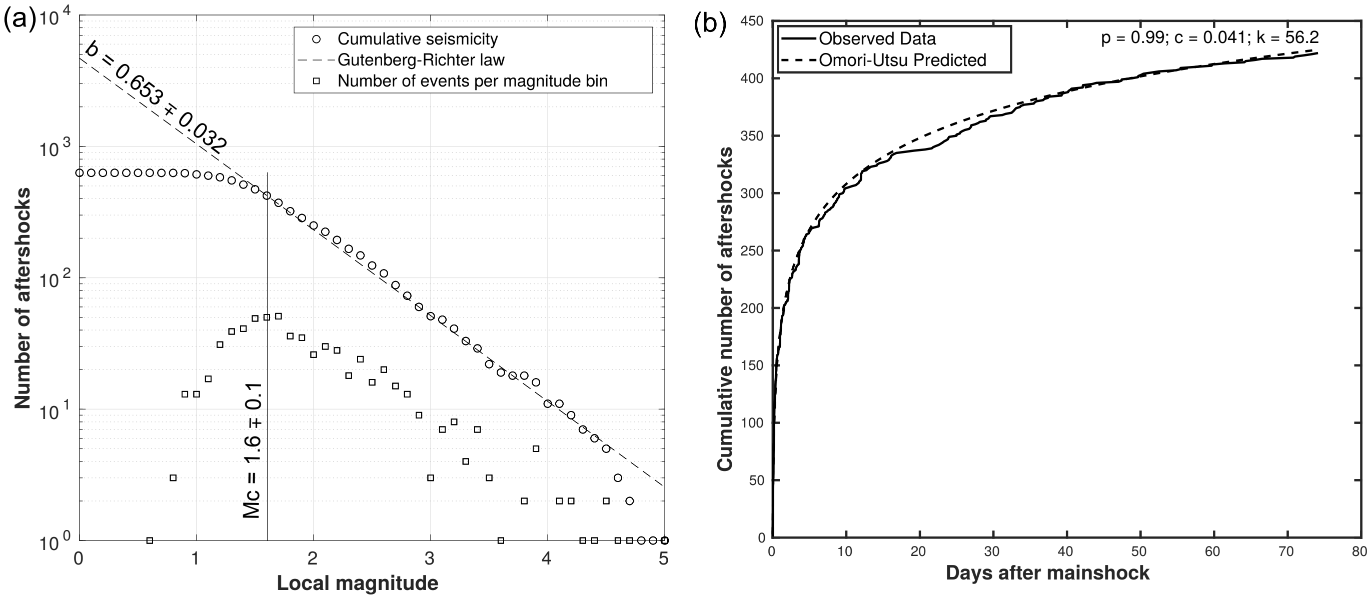
(a)
Cumulative seismicity
Gutenberg-Richter law
Number of events per magnitude bin
b = 0.653 ∓ 0.032
Mc = 1.6 ∓ 0.1
Number of aftershocks
Local magnitude
(b)
Observed Data
Omori-Utsu Predicted
p = 0.99; c = 0.041; k = 56.2
Cumulative number of aftershocks
Days after mainshock

Figure 2.

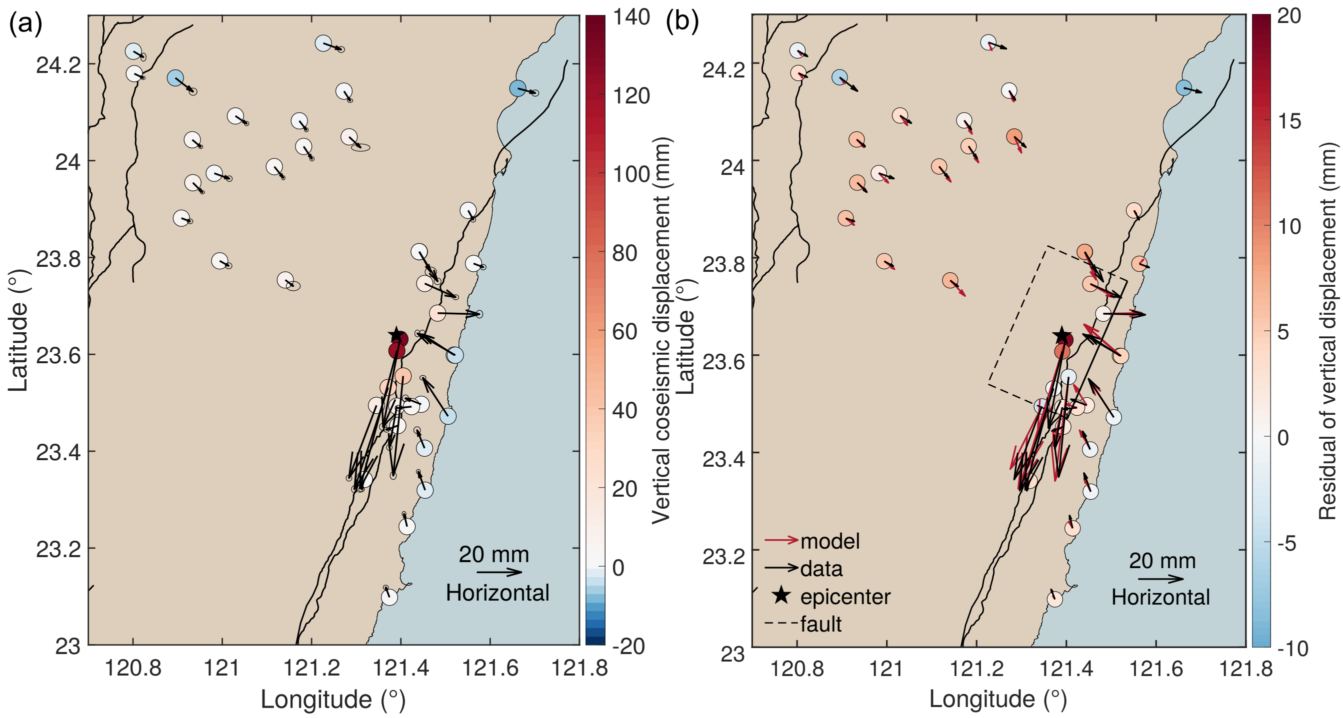
(a)
Latitude (°)
Longitude (°)
Vertical coseismic displacement (mm)
20 mm
Horizontal
(b)
Latitude (°)
Longitude (°)
Residual of vertical displacement (mm)
model
data
epicenter
fault
20 mm
Horizontal

Figure 3.

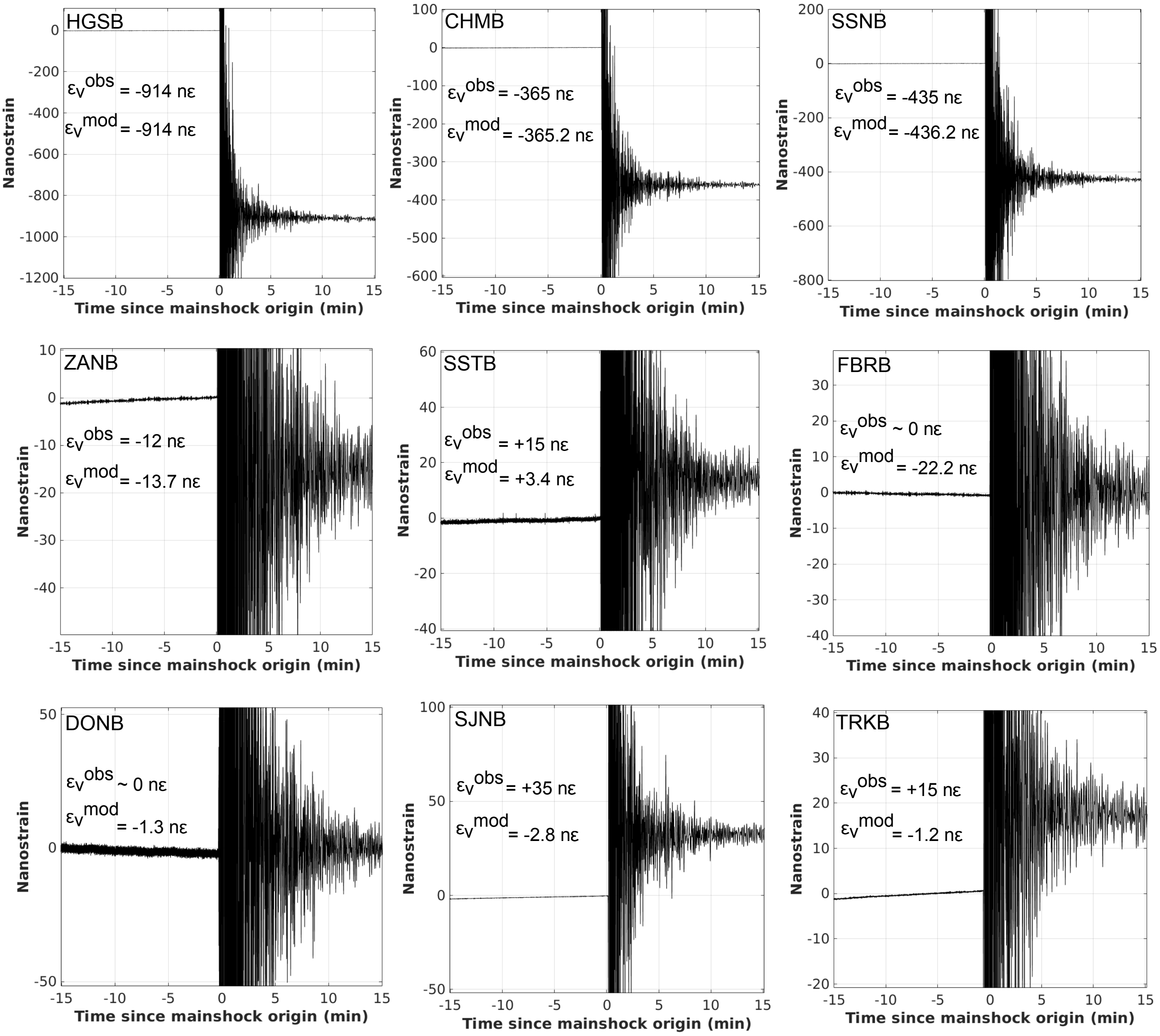
HGSB
ε_V^{obs} = -914 nε
ε_V^{mod} = -914 nε
CHMB
ε_V^{obs} = -365 nε
ε_V^{mod} = -365.2 nε
SSNB
ε_V^{obs} = -435 nε
ε_V^{mod} = -436.2 nε
ZANB
ε_V^{obs} = -12 nε
ε_V^{mod} = -13.7 nε
SSTB
ε_V^{obs} = +15 nε
ε_V^{mod} = +3.4 nε
FBRB
ε_V^{obs} ~ 0 nε
ε_V^{mod} = -22.2 nε
DONB
ε_V^{obs} ~ 0 nε
ε_V^{mod} = -1.3 nε
SJNB
ε_V^{obs} = +35 nε
ε_V^{mod} = -2.8 nε
TRKB
ε_V^{obs} = +15 nε
ε_V^{mod} = -1.2 nε
Nanostrain
Time since mainshock origin (min)

Figure 4.

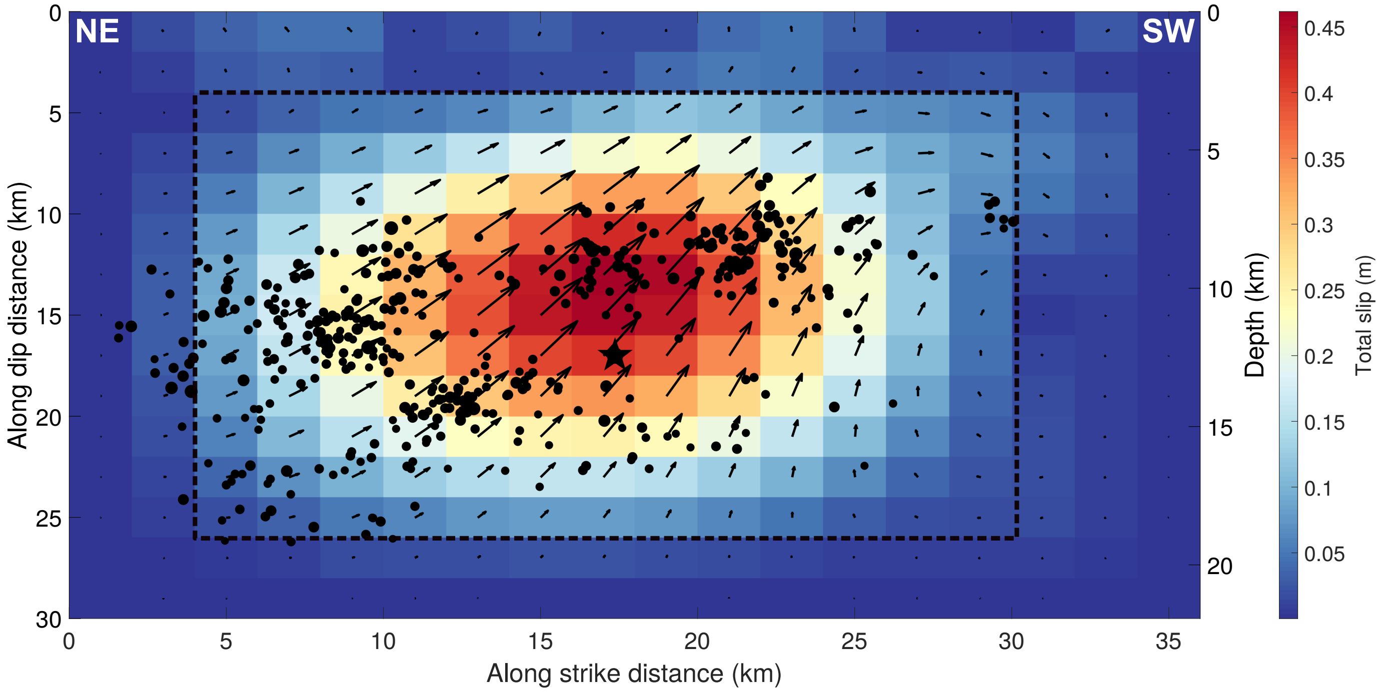
NE
SW
Along dip distance (km)
Along strike distance (km)
Depth (km)
Total slip (m)
0
5
10
15
20
25
30
35
0.45
0.4
0.35
0.3
0.25
0.2
0.15
0.1
0.05

Figure 5.

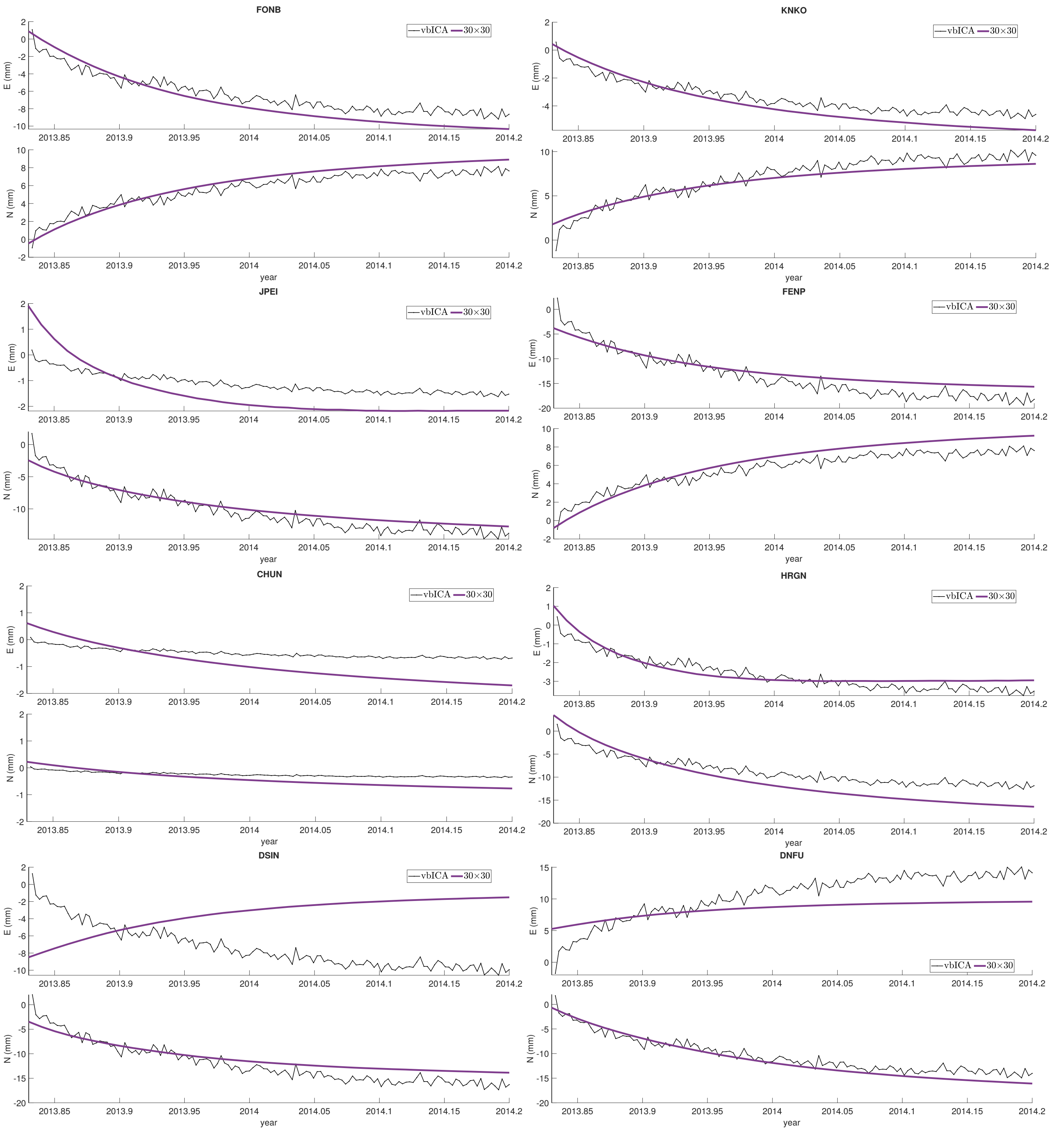
FONB
KNKO
JPEI
FENP
CHUN
HRGN
DSIN
DNFU
vbICA
30×30
E (mm)
N (mm)
year

Figure 6.

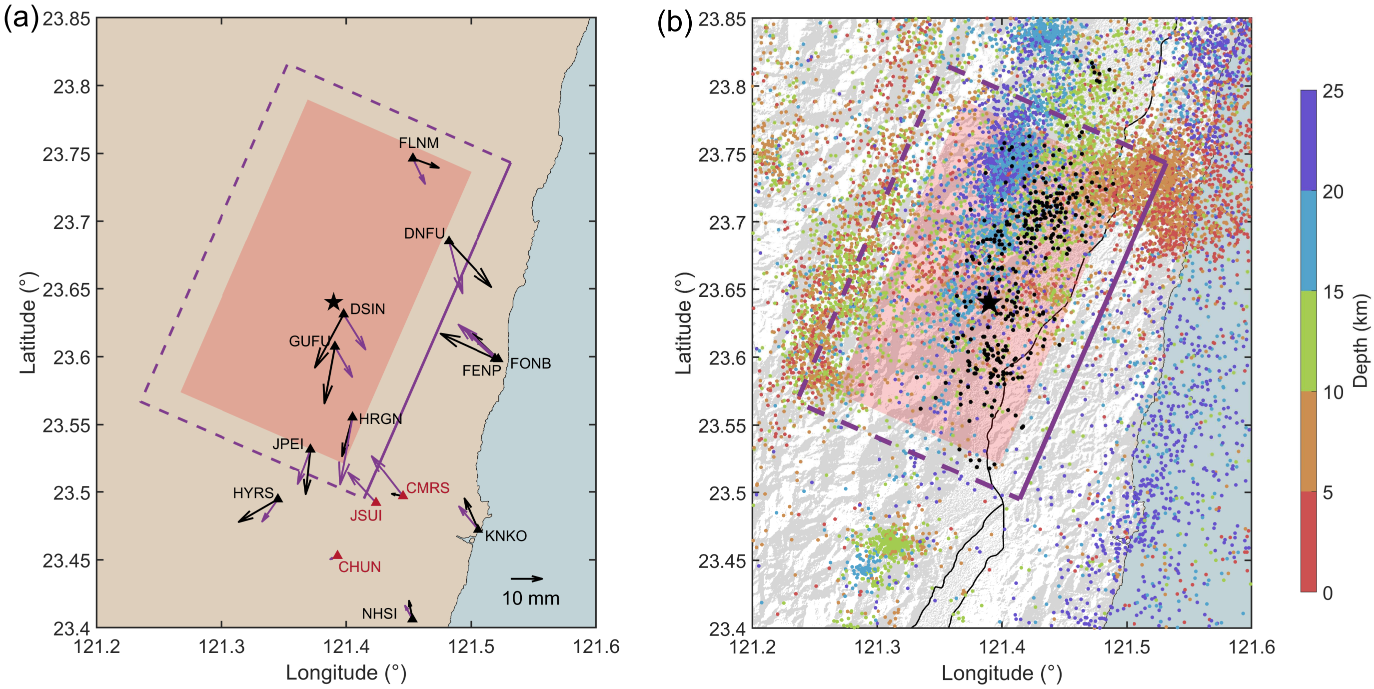
(a)
FLNM
DNFU
DSIN
GUFU
FENP
FONB
HRGN
JPEI
HYRS
CMRS
JSUI
KNKO
CHUN
NHSI
10 mm
Latitude (°)
Longitude (°)
(b)
Depth (km)
0
5
10
15
20
25

Figure 7.

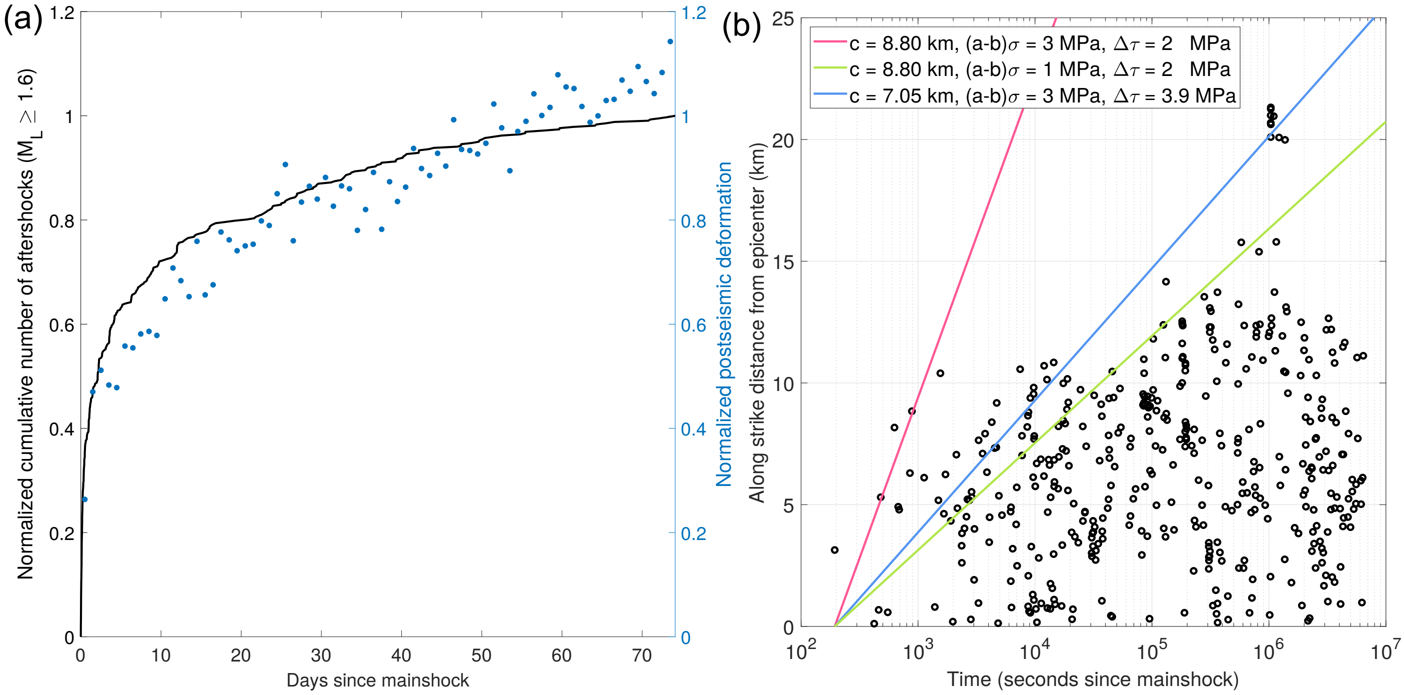

(a)
Normalized cumulative number of aftershocks ($M_L \geq 1.6$)
Normalized postseismic deformation
Days since mainshock
(b)
c = 8.80 km, (a-b)σ = 3 MPa, $\Delta\tau$ = 2 MPa
c = 8.80 km, (a-b)σ = 1 MPa, $\Delta\tau$ = 2 MPa
c = 7.05 km, (a-b)σ = 3 MPa, $\Delta\tau$ = 3.9 MPa
Along strike distance from epicenter (km)
Time (seconds since mainshock)

Figure 8.

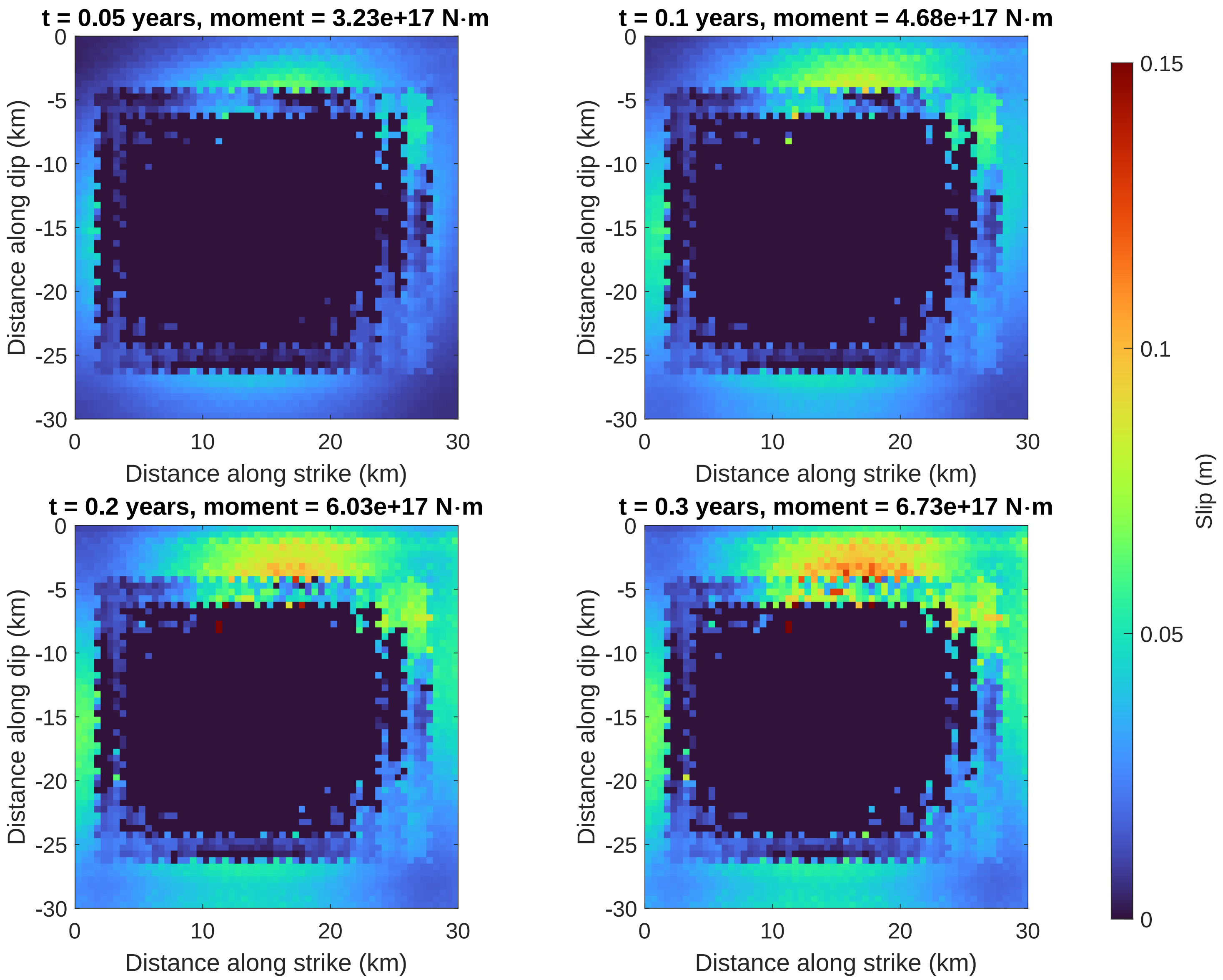
t = 0.05 years, moment = 3.23e+17 N·m
t = 0.1 years, moment = 4.68e+17 N·m
t = 0.2 years, moment = 6.03e+17 N·m
t = 0.3 years, moment = 6.73e+17 N·m
Distance along dip (km)
Distance along strike (km)
Slip (m)
0
-5
-10
-15
-20
-25
-30
10
20
30
0.15
0.1
0.05

Figure 9.

Supporting Information for "Interplay between seismic and aseismic deformation on the Central Range fault during the 2013 M_w 6.3 Ruisui earthquake (Taiwan)"

Hsiao-Fan Lin[1], Adriano Gualandi[2], Yu-Fang Hsu[3], Ya-Ju Hsu[1], Hsin-Hua Huang[1], Hsin-Ming Lee[1] and Alexandre Canitano[1*]

Contents of this file

1. Figure S1 to S8
2. Tables S1 to S2

Introduction

Corresponding author: A. Canitano, Institute of Earth Sciences, Academia Sinica, P.O Box 1-55, Nankang, Taipei, Taiwan. (canitano@earth.sinica.edu.tw)

[1]Institute of Earth Sciences, Academia Sinica, Nankang, Taipei, Taiwan.

[2]Department of Earth Sciences, Bullard Laboratories, UK.

[3]Department of Earth Sciences, University of Southern California, Los Angeles, CA, USA.

This supplement presents seismological and geodetic data processing and additional simulations of afterslip (Figures S1 to S8). Tables S1 and S2 present the GNSS stations analyzed for the Ruisui coseismic deformation and the source parameters inferred from the joint inversion of GNSS and strain data, respectively.

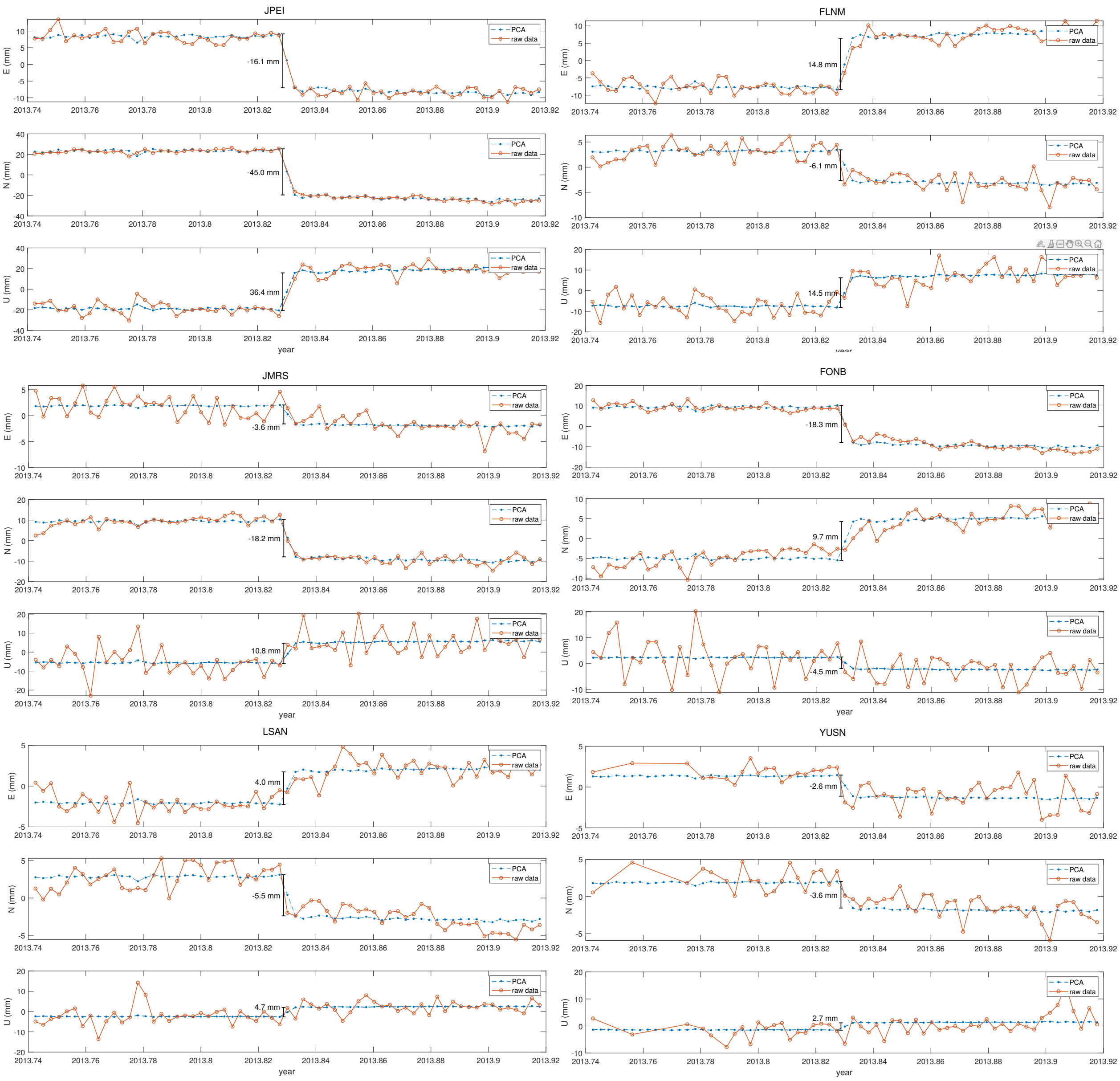

Figure S1: Example of analysis in principal component (PCA) over a 2-month period showing the extraction of the coseismic displacements related to the 2013 Ruisui earthquake.

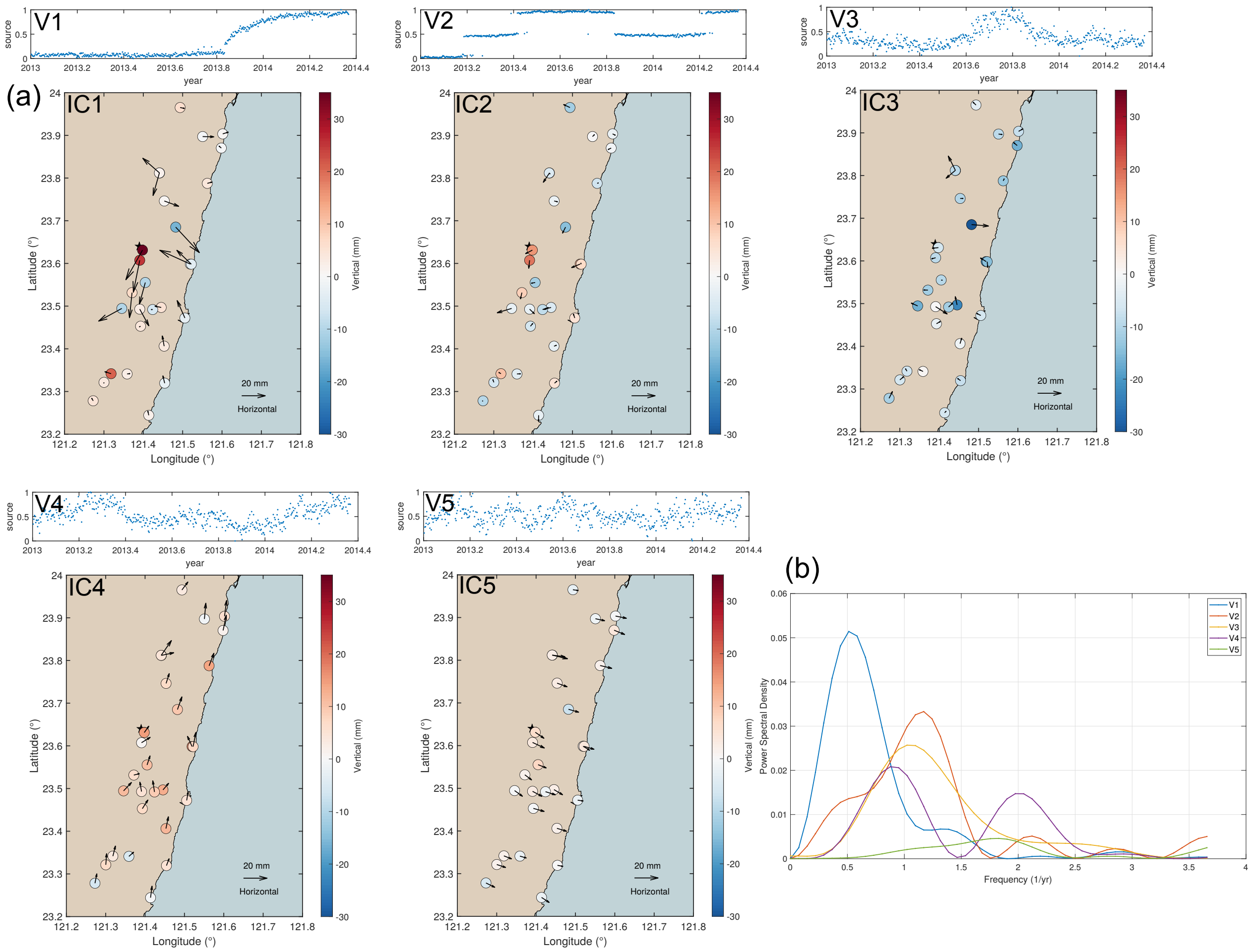

Figure S2: (a) Temporal evolution V of the five independent components (ICs) over a 1.5-year period and related 3-D displacements (28 stations). (b) Power spectral density plots of the ICs. The component associated with the Ruisui afterslip (IC1) represents the dominant signal in GNSS time series.

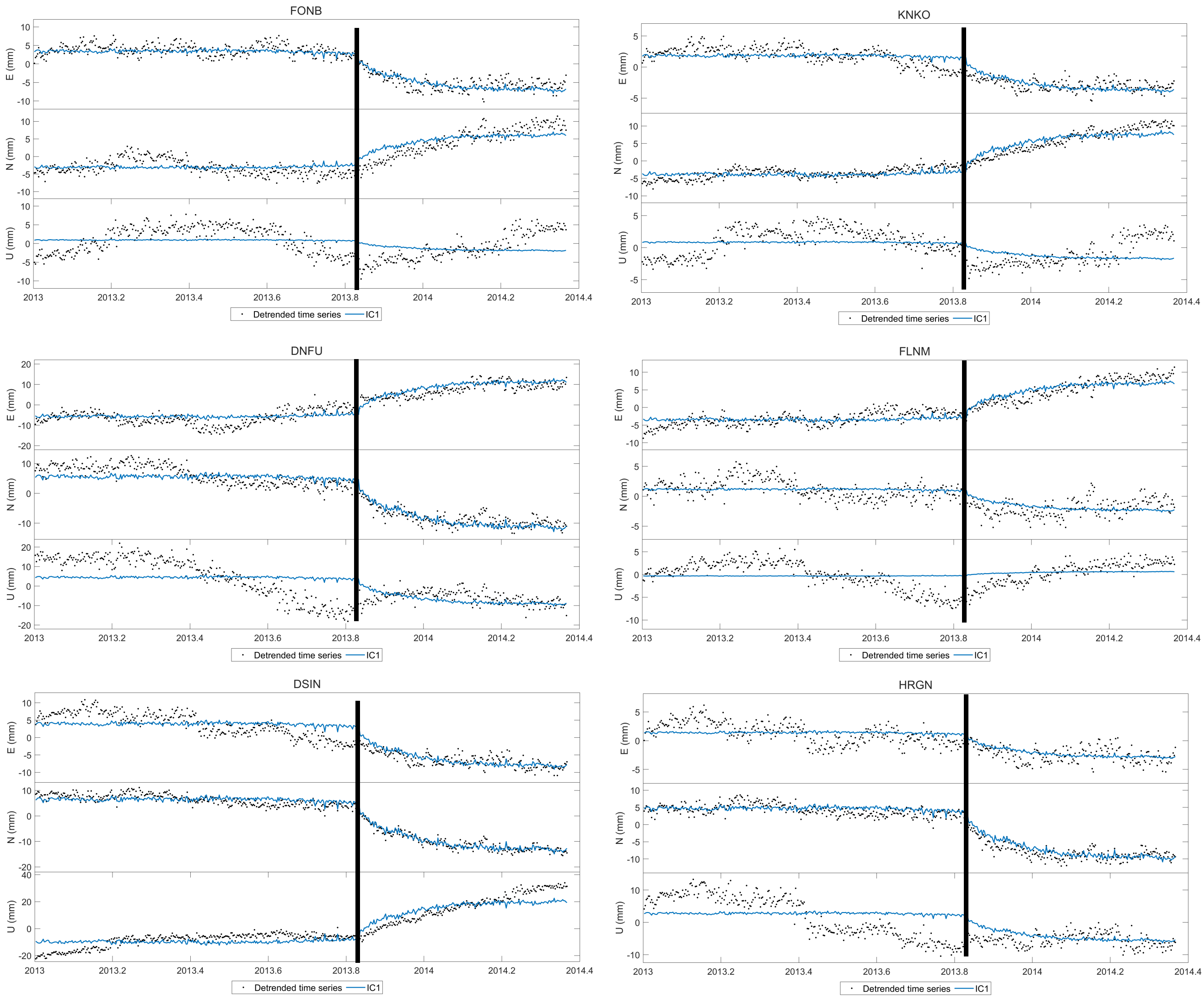

Figure S3: Example of analysis in independent component (ICA) over a 1.5-year period showing the extraction of the postseismic displacements (IC1) related to the 2013 Ruisui earthquake (marked as vertical black line).

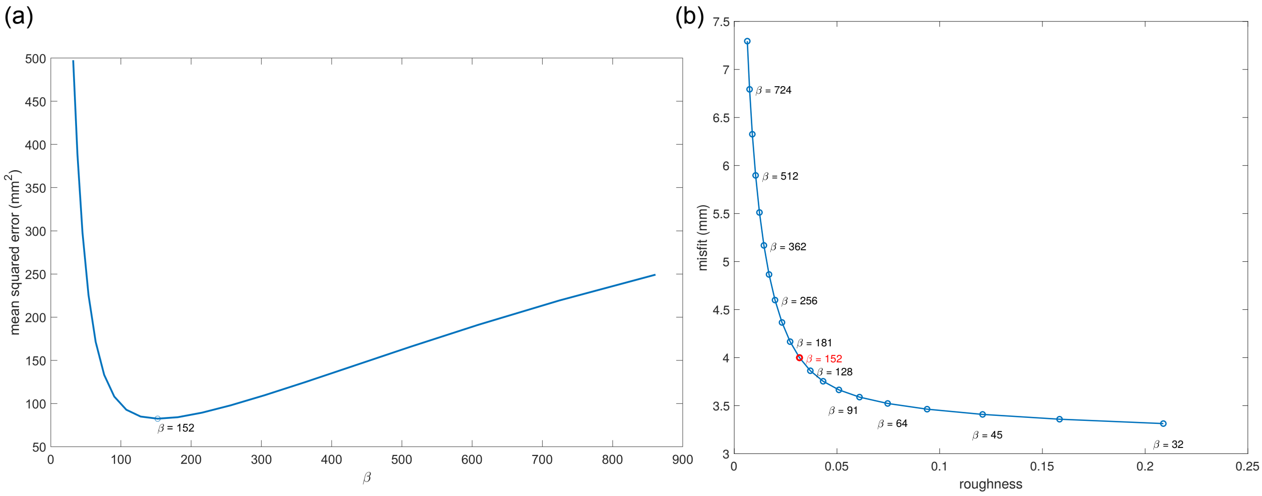

Figure S4: (a) Optimal smoothing factor obtained by minimizing the leave-one-out cross-validation mean squared error. (b) Trade-off curve between GNSS misfit and model roughness for different smoothing factors. A value of $\beta = 152$ is selected for the finite-fault coseismic model.

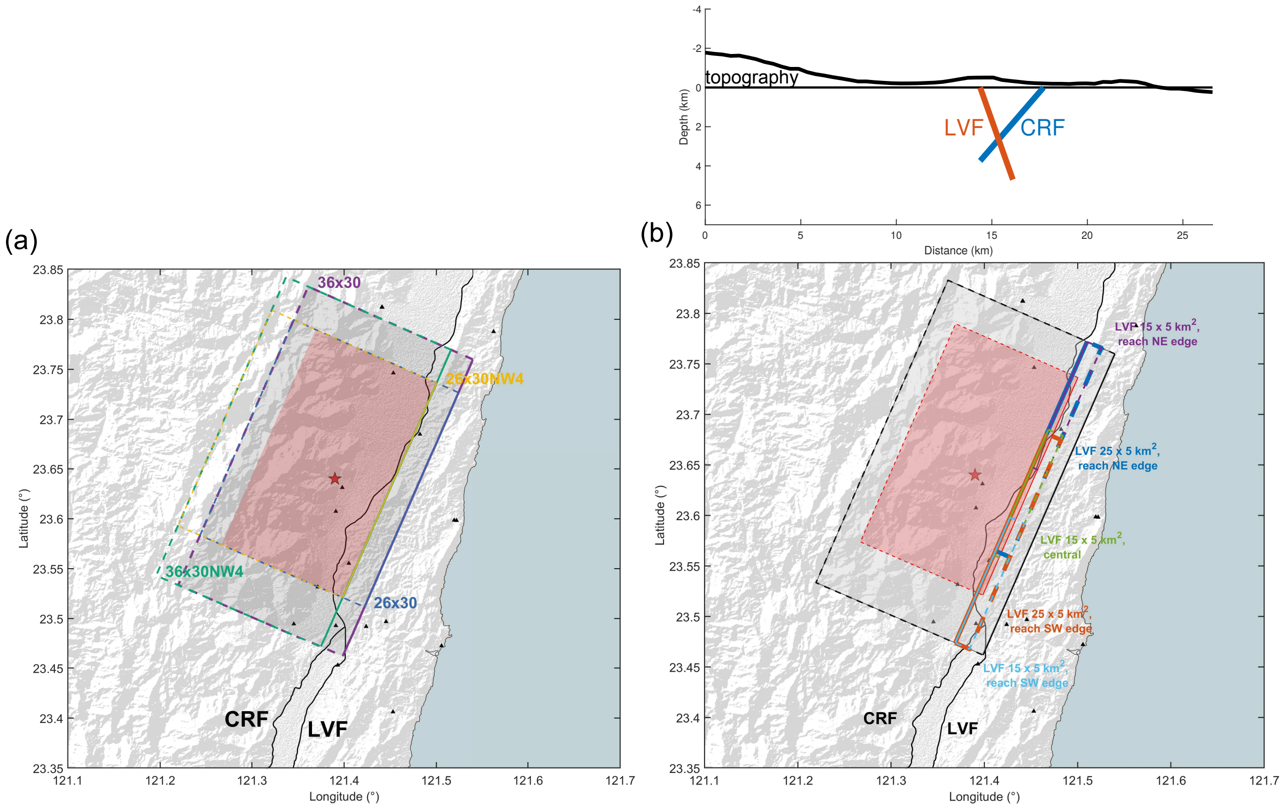

Figure S5: (a) Examples of initial receiver parametrization on the CRF (strike = 203°, dip = 48°, rake = 47°) for forward rate-and-state friction modeling. The red rectangle denotes the surface projection of the main region of coseismic slip (26 km × 22 km) used as the stress-driven source. The red star denotes the epicenter of the Ruisui earthquake and triangles are GNSS stations (see Figure 1(a)). (b) Parametrization of the shallow section of the LVF (strike = 20°, dip = 60°, rake = 60°). The black thick line depicts the top edge of each fault plane and the dashed line the surface projection. The updip panel shows a schematic view of the fault intersection.

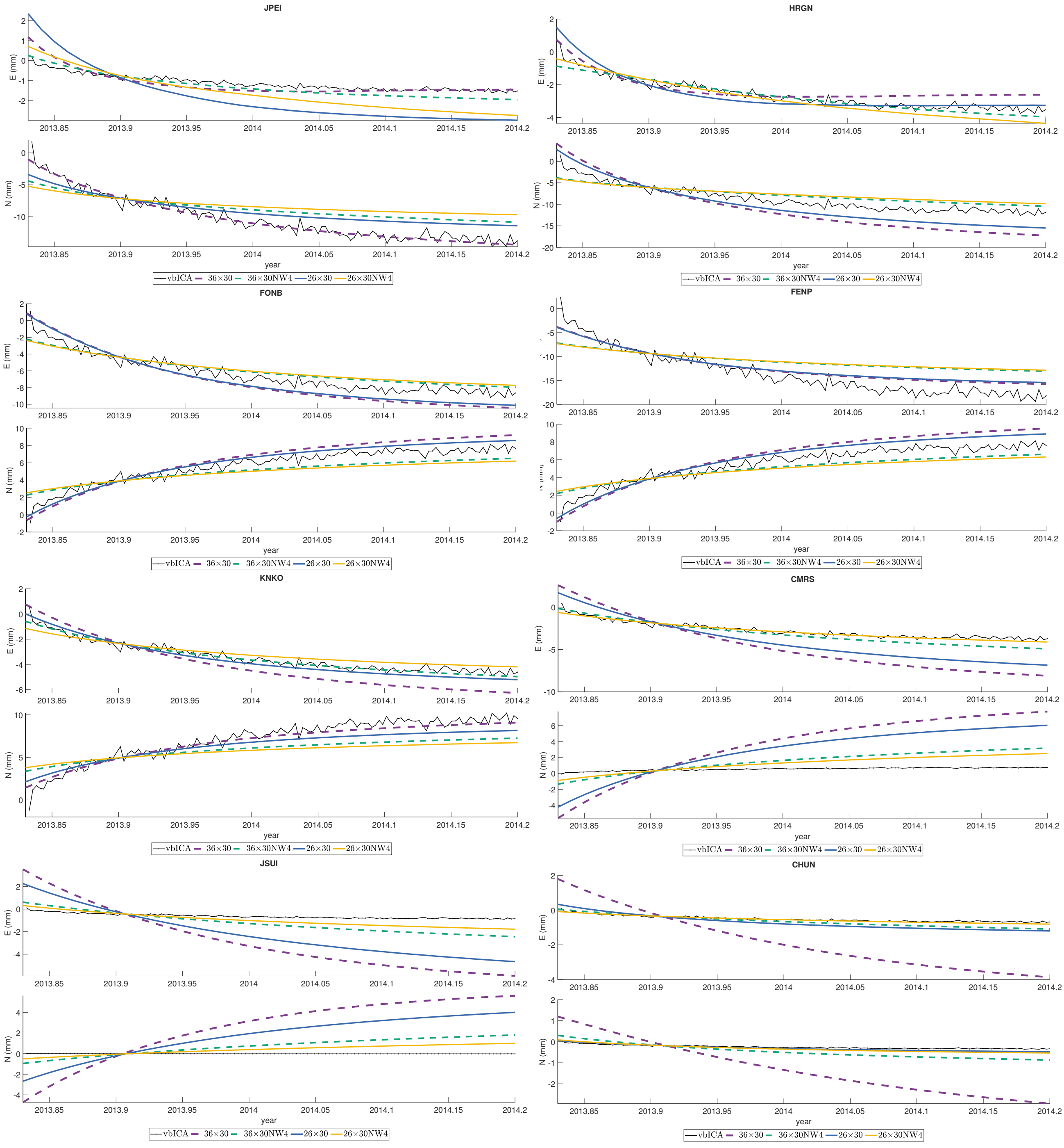

Figure S6: Horizontal displacements generated by stress-driven afterslip for initial receiver configuration on the CRF (see Figure S5(a)) ($v_0 = 5$ mm.yr^{-1}, $(a-b)\sigma = 3$ MPa).

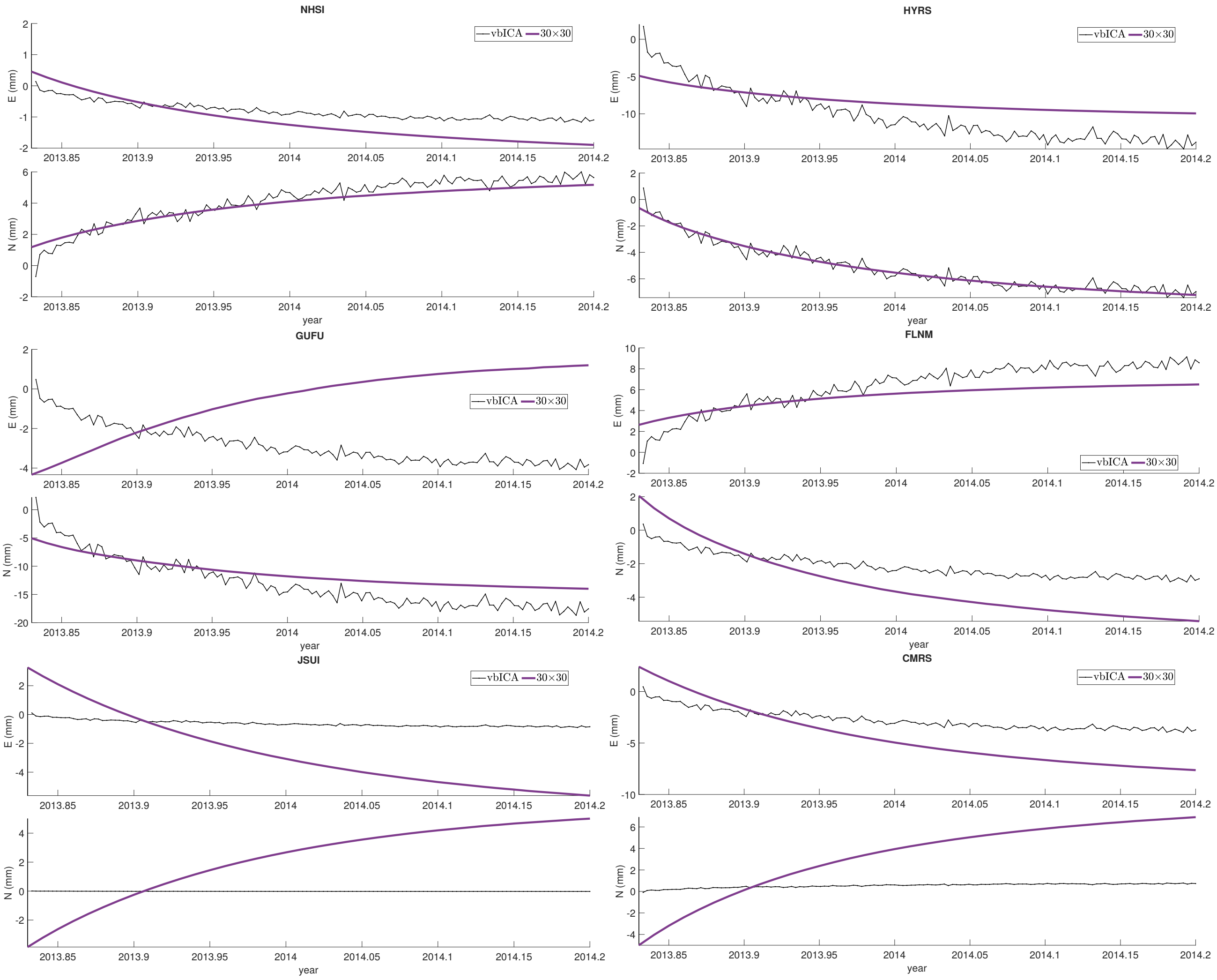

Figure S7: Additional examples of horizontal displacements generated by stress-driven afterslip on the CRF (see Figure 6 for details).

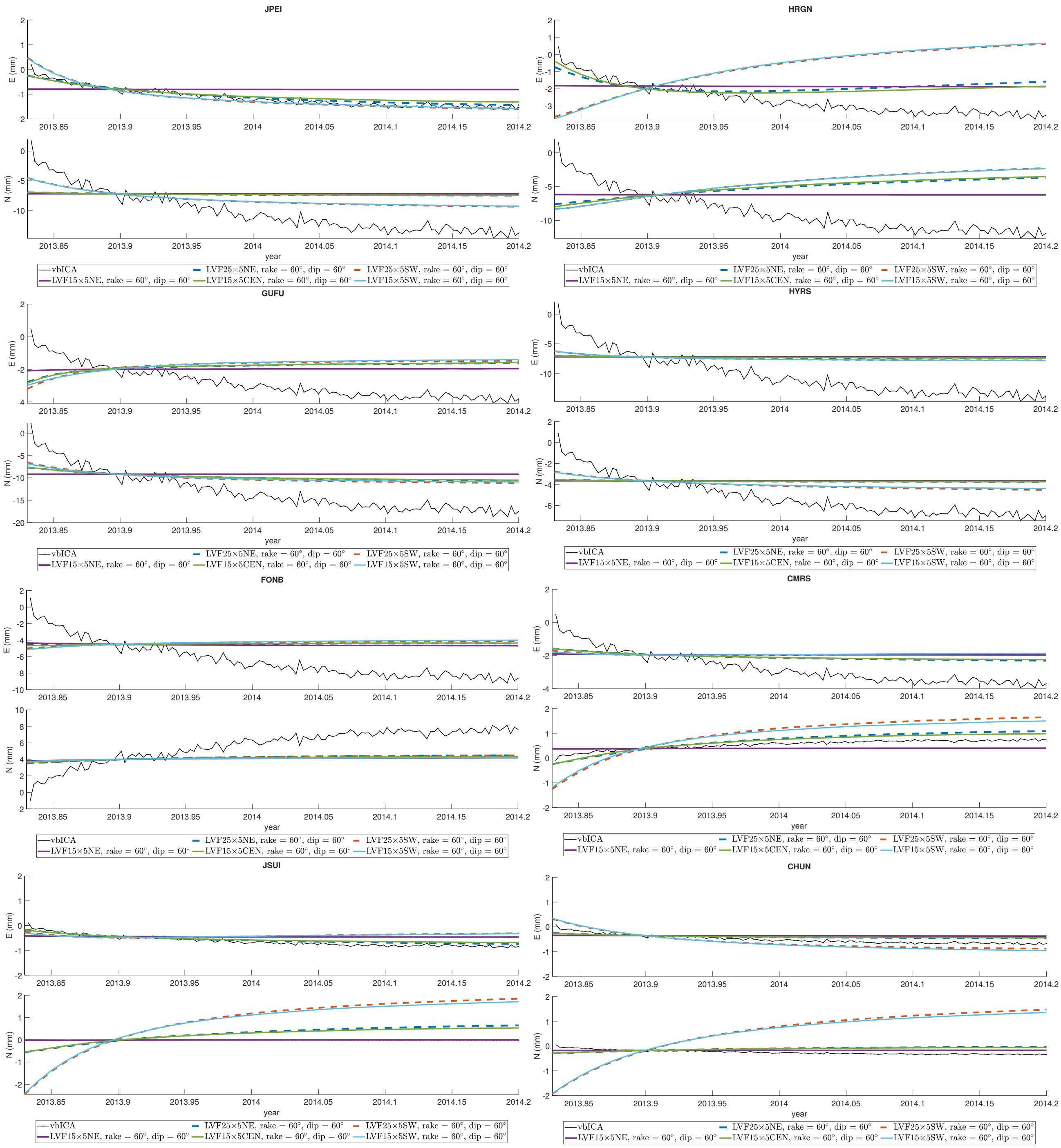

Figure S8: Horizontal displacements generated by stress-driven afterslip for initial receiver configuration on the LVF (see Figure S5(b)) ($v_0 = 5$ mm.yr^{-1}, $(a-b)\sigma = 3$ MPa).

Table S1: GNSS stations analyzed for the Ruisui coseismic deformation.

Station	Lon. (°E)	Lat. (°N)	N (mm)	ϵ_N (mm)	E (mm)	ϵ_E (mm)	Z (mm)	ϵ_Z (mm)
CHNT	121.6619	24.1492	-1.95	0.45	7.83	0.53	-8.91	1.25
SHUL	121.5627	23.7876	-1.53	0.42	4.38	0.44	2.61	0.90
NDHU	121.5508	23.8972	-3.84	0.40	2.26	0.41	1.61	0.88
FONB	121.5220	23.5982	9.02	0.49	-17.03	0.49	-4.35	0.88
FENP	121.5194	23.5985	8.60	0.54	-14.26	0.51	-4.30	1.15
KNKO	121.5057	23.4722	15.89	0.45	-11.30	0.50	-4.23	0.90
DNFU	121.4823	23.6851	-0.43	0.52	18.73	0.56	21.89	0.96
PING	121.4543	23.3195	7.66	0.39	-3.02	0.37	-0.88	0.86
FLNM	121.4534	23.7463	-5.68	0.41	13.87	0.51	13.31	0.80
NHSI	121.4530	23.4062	7.44	0.49	-3.34	0.50	-2.09	0.94
CMRS	121.4455	23.4969	2.49	0.47	-7.07	0.48	0.55	0.97
WARO	121.4409	23.8120	-12.25	0.49	8.28	0.51	1.97	0.80
JSUI	121.4239	23.4920	-0.58	0.41	-6.07	0.45	4.48	0.81
NPRS	121.4139	23.2443	5.26	0.39	-1.35	0.36	3.04	0.83
HRGN	121.4051	23.5553	-41.15	0.70	-4.45	0.48	38.88	0.95
DSIN	121.3980	23.6312	-36.19	0.66	-7.59	0.54	131.99	1.32
CHUN	121.3931	23.4529	-1.76	0.37	-5.08	0.45	4.47	0.86
GUFU	121.3910	23.6074	-56.81	0.80	-16.55	0.53	120.56	1.20
JMRS	121.3910	23.4942	-17.02	0.50	-3.36	0.44	9.75	0.93
CHGO	121.3745	23.0983	4.12	0.36	-1.69	0.41	2.10	0.87
JPEI	121.3714	23.5316	-42.02	0.70	-15.09	0.51	33.73	0.88
HYRS	121.3454	23.4946	-30.02	0.60	-12.34	0.49	12.62	0.86
JULI	121.3182	23.3417	-4.09	0.40	-1.27	0.45	3.73	0.83
NGAO	121.2845	24.0495	-4.44	0.75	5.17	2.09	7.40	5.83
HUAN	121.2726	24.1435	-3.92	0.34	2.73	0.44	-0.14	0.65
JYAN	121.2263	24.2425	-2.62	0.44	8.00	0.51	-1.34	0.90
LSAN	121.1822	24.0293	-5.11	0.38	3.74	0.40	4.21	0.72
MFEN	121.1725	24.0822	-3.74	0.35	3.15	0.35	0.43	0.70
DNDA	121.1412	23.7536	-2.52	0.97	3.55	1.58	5.95	4.14
KAFN	121.1165	23.9876	-4.62	0.36	4.05	0.34	4.81	0.80
HUYS	121.0294	24.0923	-3.16	0.37	5.04	0.39	3.35	0.81
HLIU	120.9942	23.7930	-2.05	0.43	4.03	0.49	5.01	0.98
PLIM	120.9820	23.9739	-2.24	0.44	6.77	0.47	1.51	0.92
S167	120.9341	23.9544	-3.95	0.31	4.28	0.40	6.26	0.75
DPIN	120.9328	24.0431	-2.91	0.33	3.79	0.36	5.68	0.81
SUN1	120.9084	23.8812	-1.31	0.38	3.88	0.44	5.67	0.83
HOPN	120.8949	24.1708	-5.69	0.49	7.94	0.55	-5.91	1.17
S016	120.8029	24.1796	-1.75	0.30	3.99	0.38	3.71	0.61
NSHE	120.8009	24.2258	-2.43	0.53	4.49	0.44	-0.85	0.95
SLIN	121.4414	23.8119	-8.31	0.99	5.10	1.28	-4.74	1.92

Note: N, E and Z are the north, east, and vertical components of coseismic displacements, respectively; ϵ_N, ϵ_E, and ϵ_Z are the errors in north, east, and vertical components, respectively.

Table S2: Source parameters inferred from joint GNSS and strain data using *GBIS* inversion.

Parameter	Optimal	Lower	Upper	2.5%	97.5%
Length (km)	15.2	10	40	13.2	19.5
Width (km)	8.1	1	20	8.1	14.7
Depth (km)	6.5	0	20	4.6	6.9
Dip (°)	47	0	90	39	57
Strike (°)	203	0	360	196	212
X (km)	7.8	0	15	6.8	9.6
Y (km)	9.0	0	15	7.1	10.5
Strike-Slip (m)	0.32	-1.5	2.0	0.28	0.38
Dip-Slip (m)	0.37	-1.5	2.0	0.34	0.43

Note: We report maximum probability solution, 2.5 and 97.5 percentiles of posterior probability density functions of source fault parameters. Strike-slip is $>$ 0 if left-lateral and dip-slip is $>$ 0 for thrust-faulting.